



Title	Study on optimization and robust control of active power decoupling circuit based converters
Author(s)	Hwang, Soonhwan
Citation	北海道大学. 博士(工学) 甲第13531号
Issue Date	2019-03-25
DOI	10.14943/doctoral.k13531
Doc URL	http://hdl.handle.net/2115/74332
Type	theses (doctoral)
File Information	Hwang_Soonhwan.pdf



[Instructions for use](#)

**STUDY ON OPTIMIZATION AND ROBUST CONTROL
OF ACTIVE POWER DECOUPLING CIRCUIT BASED
CONVERTERS**

SOONHWAN HWANG

A THESIS SUBMITTED FOR THE DEGREE OF DOCTOR OF PHILOSOPHY

ELECTRIC ENERGY CONVERSION LABORATORY
DEPARTMENT OF INFORMATION SCIENCE AND TECHNOLOGY
HOKKAIDO UNIVERSITY

2019

Abstract

As the use of electrical energy increases, the range of use of electric energy conversion devices is expanding. In particular, automobiles that have used internal combustion engines have been replaced by electric transducers and motors. Unlike in the past when thermal power generation and nuclear power generation have accounted for the majority of electric power production, more stable and environmentally friendly wind power and solar power generation are increasing. These devices require converters that effectively convert various types of energy into electrical energy. Efficiency, miniaturization and stability of these power converters have been important research topics. Recently, many researchers have been studying increasing reliability and life expectancy. The life expectancy of actuators such as solar panels and light-emitting diodes(LEDs) has been increased due to the development of material technologies. However, power conversion devices have limitations in increasing lifespan due to manufacturing cost and failure rate increase. AC / DC converters require large capacitors to smooth the ripple power generated from the power source. Electrolytic capacitors(E-Caps.) have been used in many applications as they have advantages in volume and price when compared with other types of capacitors. However, there is a problem that it is susceptible to temperature and ripple current due to the structure including high equivalent series resistance(ESR) and electrolyte. This has the shortest lifespan of the components and limits the life of the power inverter. Therefore, in order to increase the lifetime of the electric energy conversion device, it is necessary to replace it with another types of capacitor having high reliability.

In recent years, research has been conducted to replace E-Caps with film capacitors having relatively long lifetime and high reliability in order to improve the lifetime and failure rate of power conversion devices. Film capacitors have a relatively long lifetime compared to E-Caps due to their low ESR, self-healing and stable structure. However, there are problems that it is difficult to apply to actual products due to the large volume and high price compared to the same capacity. To solve this problem, it is necessary to reduce the capacity of the film capacitor. Single-phase AC/DC converters are approaching two ways: capacitor-less inverter control and active power decoupling(APD) method. In the case of capacitor-less inverter control, power is controlled at the inverter side so that the motor behaves like a resistive load. This method has the advantage that

power factor correction can be performed using a small-capacity film capacitor without the need for other auxiliary circuits. However, there is a problem that demagnetization may occur due to a high phase current of the inverter, deteriorated efficiency, and noise may be generated. The APD method actively removes power ripple using an auxiliary circuit. This makes it possible to remove power ripple even with a small-capacity film capacitor. However, there is a problem that the use of the auxiliary circuit increases the manufacturing cost and increases the uncertainty due to the increased complexity, which makes it difficult to ensure stability.

In this study, we propose a solution to the problem of increased manufacturing cost and stability of existing APD system. The number of components was optimized by designing the parts used in the converter circuit and the APD circuit. In addition, the voltage stress of the parts can be reduced, making it possible to use parts with lower rated voltage, thereby reducing manufacturing costs. In addition, the converter and the APD circuit are modularized through the commonization so that it can be expanded easily according to the required capacity of the product. This enabled us to take advantage of volume benefits. In addition, we proposed a way to implement the APD function without using additional components by changing only the control method of the existing bridge-less single ended primary inductor converter(SEPIC). Sliding mode control(SMC) strategy and Lyapunov function based control are used to solve the problem of control instability of the model. Because the APD circuit uses a large number of passive elements, the process error of each passive element increases the uncertainty of the model. The proposed control scheme always guarantees stability and performance even in the presence of this uncertainty. In addition, we proposed a parameter selection criterion based on the control theory, and it is possible to design a controller which can guarantee the target performance easily. All proposed circuit and control strategies have been validated through simulation using MATLAB / SIMULINK and experiment using prototype.

Acknowledgments

I would first like to thank my advisor Prof. Satoshi Ogasawara of the department of information science of technology at Hokkaido university. The door to Prof. Ogasawara office was always open whenever I ran into a trouble spot or had a question about my research or writing. He consistently allowed this paper to be my own work, but steered me in the right the direction whenever he thought I needed it.

I would also like to thank the experts who gave a lot of valuable comments: Assoc. Prof. Masatsugu Takemoto, Assist. Prof. Koji Orikawa. Without their passionate participation and input, my research could not have been successfully conducted.

I would like to thank my fellow student for their feedback, cooperation and, of course, friendship. Thanks to them, three and a half years in Japan were not lonely and they were able to make good memories.

In particular, I would like to thank LG Electronics for giving me a chance to study as a Ph.D. program in Japan. Without their continued support, there would not have been all the research results I had achieved.

I must express my very profound gratitude to my spouse Sunkyung Hwang for providing me with unfailing support and continuous encouragement throughout my years of study and through the process of researching and writing this thesis. This accomplishment would not have been possible without her. Thank you.

Last but not the least, I would like to thank my family: my parents and to my sister for supporting me spiritually throughout writing this thesis and my life in general.

Author

Soonhwan Hwang

Contents

List of Figures	vii
List of Tables	x
1 Introduction	1
1.1 Background	1
1.2 Related Work	3
1.3 Structures and Characteristics of APD circuit for Single Phase AC/DC Converter	5
1.4 Optimized solution for robust operation and low voltage stress of APD circuit based converters	6
1.5 Contributions	7
1.6 Thesis Organization	9
2 Preliminaries	10
2.1 Operation principle of the APD method	11
3 Independent decoupling plus Inductor multiplexing method	14
3.1 Contribution Summary	14
3.2 Proposed APD circuit	15
3.2.1 Basic operation of the proposed circuit	15
3.2.2 Modulation Strategy of the Proposed Converter	17
3.3 Control System	19
3.3.1 Buffer voltage control	19
3.3.2 Active power decoupling control	20
3.4 Sliding Mode Control Algorithm	20
3.5 Simulation studies and experimental results	31
3.5.1 System configuration	31
3.5.2 Allowable voltage and ripple current of the buffer capacitor	34
3.5.3 Simulation and experimental results	35
3.6 Conclusion	39
4 Lyapunov function based control strategy	41
4.1 Contribution Summary	42
4.2 Modeling of the buck-boost converter with the APD circuit	42
4.3 Lyapunov-function based control strategy	43

4.3.1	Robustness of the proposed control system to converter parameter's variations	46
4.4	Simulation studies and experimental results	47
4.5	Conclusion	49
5	Modular design and interleaving structure of APD circuit based converter	50
5.1	Contribution Summary	50
5.2	APD circuit based AC/DC interleaved buck-boost converter	50
5.3	Control System	54
5.3.1	Buffer voltage control	54
5.3.2	Active power decoupling control	56
5.4	Circuit configuration of loss-less clamp snubber for proposed converter	61
5.5	Simulation studies	62
5.6	Conclusion	65
6	Implement APD function for bridge-less SEPIC without auxiliary circuit	66
6.1	Contribution Summary	66
6.2	Operation and Modeling of the Bridge-less SEPIC PFC Rectifier	67
6.3	Proposed Control Strategy	69
6.4	Simulation Results	72
6.5	Conclusion	81
7	Reducing voltage stress of Bridge-less SEPIC based active power decoupling circuit	82
7.1	Contribution summary	82
7.2	Proposed circuit and control method	82
7.3	Simulation results	83
8	Summary and recommendations for future study	87
8.1	Summary	87
8.2	Recommendations for future study and implications for research	88
8.3	Conclusions	88
	References	89

List of Figures

1.1	Percentage of the response to the most frangible components in power electronic systems from an industry survey[4]	2
1.2	The combined structure of the APD circuit and the converter circuit, (A) independent decoupling topology, (b) switch multiplexing decoupling topology(c) switch and inductor multiplexing decoupling topology	4
1.3	Three types of APD circuits, (A) buck type (b) buck-boost type (c) boost type	5
1.4	Proposed APD topology	7
1.5	Proposed multi-phase interleaved APD topology	8
2.1	Basic active power decoupling topology	11
2.2	Required minimum capacitance	12
2.3	Key waveforms of the ideal AC-DC converter applied to the decoupling circuit	13
3.1	Capacitance per volume ratio of film capacitor according to rated voltage	14
3.2	The proposed buck-boost converter with the APD circuit	15
3.3	Current flows for each switch combination: (a) State1, (b) State2, (c) State3, and (d) State4	16
3.4	Switching pattern (a) discharging operation,(b) charging operation	18
3.5	State trajectories of each control phases	21
3.6	Magnetization current shapes in (a) discharging operation and (b) charging operation	23
3.7	Existence region of the sliding motion during the discharging operation ($v_{out} = 150V$, $v_{in} = 0V$)	26
3.8	Existence of the sliding motion region during the charging operation($v_{out} = 150$ V and $v_{in} = 141$ V)	27
3.9	Overall control scheme of the proposed converter	29
3.10	Hardware prototype	33
3.11	Laboratory test bed	33
3.12	Simulation waveforms and the sliding motion of states	35
3.13	Experimental waveform produced by the proposed control mechanism	36
3.14	Experimental waveform of the coupled-inductor current	36
3.15	Experimental waveform in the transient response during 50 % to 75 % load steps	37
3.16	Experimental waveform in the transient response during 75 % to 50 % load steps	37
3.17	Simulation results of the transient response under the inductance change	38
3.18	Power factor and efficiency of the proposed converter	39

4.1	Nonlinear characteristics of passive devices (a) Inductor, (b) Capacitor	41
4.2	Proposed control system	45
4.3	Simulation results of the prototype	47
4.4	Experimental waveforms (a) steady state and (b) current of the coupled-inductor	48
4.5	Transient response during (a) 500 Ω to 333 Ω and (b) 333 Ω to 500 Ω resistance change	48
5.1	Proposed circuit (left) and basic module (right).	51
5.2	Overall operations of proposed active power decoupling (APD) circuit.(a) State1, (b) State2, (c) State3, (d) State4, (e) State5	52
5.3	Overall control scheme of the proposed circuit	60
5.4	Lossless snubber operation and waveforms	62
5.5	Waveforms and control inputs of the proposed control system	63
5.6	Waveform comparison (a) non-interleaved circuit [Input filter : 300 μ H, 3 μ F], (b) 3-phase interleaved circuit [Input filter : 30 μ H, 3 μ F]	63
5.7	Waveform in the transient response during (a) 1250 W to 2500 W and (b) 2500 W to 1250 W load steps	64
5.8	A prototype of the interleaved converter based on the proposed APD circuit	65
6.1	Bridge-less SEPIC PFC rectifier	67
6.2	Bridge-less SEPIC PFC rectifier current flow according to a combination of switches.	68
6.3	Proposed control system	73
6.4	Conventional control system in [37]	74
6.5	Waveform and switch operation of bridge-less SEPIC by APD operation mode.	75
6.6	Simulation for global stability of the proposed control methods in the load variation condition	76
6.7	Comparison of control performance in the steady state, Red line: Proposed control method, Blue line: Method in [37]	77
6.8	Comparison of controller performance under load change conditions, Red line: Proposed control method, Blue line: Method in [37]	78
6.9	Comparison of controller performance under input voltage change conditions, Red line: Proposed control method, Blue line: Method in [?]	79
6.10	Harmonic current spectrum of the input current, conventional control method (red), proposed control method (blue)	80
7.1	Waveforms with target buffer voltage of 350 V	83
7.2	Proposed circuit	83
7.3	Simulation waveforms of the proposed circuit	84
7.4	Current wave due to ratio of 3rd harmonic current	84
7.5	Analysis of harmonic spectrum according to k_{3rd} value	85

7.6	Simulation results for applying 3rd harmonic injection method.	86
-----	--	----

List of Tables

1.1	Film vs. Electrolytic capacitor comparison	2
3.1	Simulation parameters	32
3.2	Hardware specification	32
3.3	Comparison between conventional method and proposed method	40
5.1	Snubber circuit comparison results	61
5.2	Simulation parameters	62
6.1	Simulation parameters	72
6.2	Design parameters of the proposed method and PI+PR control	72
6.3	Comparison between the proposed control method and the conventional method	81

CHAPTER 1

Introduction

1.1 Background

Due to the increasing demand for environmentally friendly energy and the issue of efficient use of energy, the application fields of power conversion devices are increasing.[1][2][3] In the past, research has focused on improving efficiency and regulation of power conversion devices, such as power factor, total harmonic distortion(THD), and manufacturing cost and performance. However, the lifespan and reliability of the power conversion device are becoming important as the application range of the power conversion device is expanded. In the case of PV panels and LEDs, the lifespan of the photovoltaic(PV) panels or LEDs has been lengthened due to the development of the material technology. However, there is a problem that the lifetime of the power conversion device is not long enough, and reliability due to a harsh external environment is also a problem. These problems are mainly caused by the E-Caps used for the AC/DC or DC/AC power conversion. E-Caps have high capacitance to volume and are advantageous in manufacturing cost, but E-Caps have a high failure rate and low reliability. According to the survey [4], capacitors account for 20% of the total failure rate of power electronic components. Compared to film capacitors in Table 1.1, E-Caps have relatively high ESR, short life expectancy and structural weaknesses. This means that power conversion devices using E-Caps are vulnerable to changes in harsh external environments and ripple currents, which may limit the lifespan of the product.[5][6] Therefore, in order to solve this problem, it is necessary to replace the film capacitor with a more reliable and long-life film capacitor. However, film capacitors at the same capacitance are bulky and expensive than E-caps.

APD method is one of the suitable solutions to realize the decoupling function with a small film capacitor.[7][8][9][10][11][12] To use small film capacitors, APD method uses auxiliary circuits consisting of switches and energy storage components and control algorithms to actively absorb and release AC power. The advantage of this approach is that the use of film capacitors ensures a long lifespan and high reliability, and it can be applied to existing converter circuits with a few modifications. Also, by adjusting the voltage fluctuation range of the buffer capacitor of the auxiliary circuit, the required capacitance can be greatly

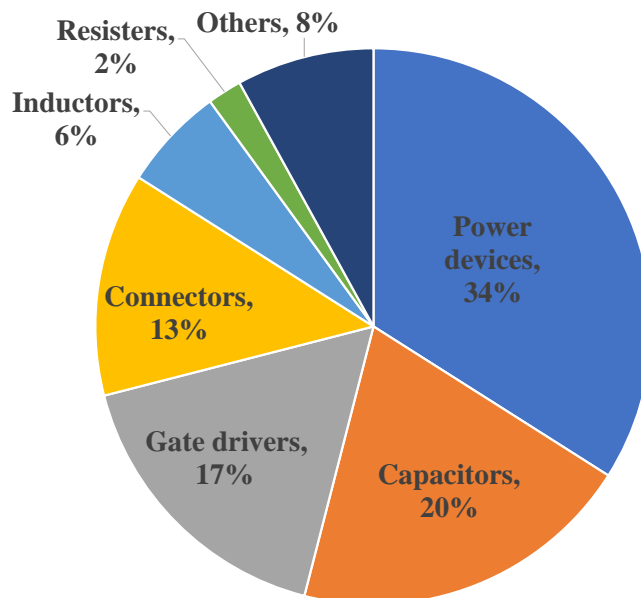


Figure 1.1: Percentage of the response to the most frangible components in power electronic systems from an industry survey[4]

reduced.

The conventional APD methods cause various problems because the use of the auxiliary circuit is necessary for ripple power removal. The auxiliary circuit requires several switches,

Table 1.1: Film vs. Electrolytic capacitor comparison

Characteristic	Electrolytic	Film
Capacitance/volume	High	Low
ESR	-	1/10 of electrolytic
Over-voltage capability	50V surge	1.5 x rated
Construction	Liquid or Gel can leak	Dry
Life expectancy	6,000 to 78,000 hours	200,000 hours
Self healing	x	o

diodes, capacitors, and inductors. Therefore, there are problems with the use of auxiliary circuits that increase the manufacturing cost and the size of the circuits.

1.2 Related Work

As shown in Fig. 1.2, converters with APD can be divided into three topologies depending on the combined structure of the APD circuit and the converter circuit.[13]

The first approach is an independent decoupling method.[14][15][16] Independent decoupling method in the decoupling scheme refers to the way in which components between the converter circuit and the APD circuit are constructed independently. Therefore, it is advantageous that the two circuits are constructed independently so that the modeling is simple and the voltage stress of each component is low. However, there is a disadvantage that the manufacturing cost and volume increase due to the use of many parts.

The second approach called switch-multiplexing method is to share components between the converter and the APD circuits with two circuit-sharing switches or bridge arms. This has the obvious benefit of reducing the number of switches but also has drawbacks in that the DC-link voltage range and the voltage stress of arms. Therefore, the switch multiplexing method has a limitation in using parts having a high rated voltage, which causes an increase in manufacturing cost. Moreover, there is a problem that modeling of the circuit becomes complicated due to the sharing of the switches, and the nonlinearity increases and the control becomes difficult.[17][18]

The third approach is switch and inductor multiplexing method.[19] It is a method that can reduce the number of parts the most by sharing inductor and switch commonly used in converter circuit and APD circuit. This approach has the benefit of high efficiency, long lifespan, the wide operational range for output voltage and manufacturing cost. However, this method requires that the buffer voltage be higher than the output voltage so that the voltage stress of the devices is higher than other methods. For this reason, there is a problem in that components with high voltage rating must be used. Thus, it is difficult to apply to high voltage and high power applications. Further, if the buffer capacitor is not sufficiently discharged under the condition that the input current is close to zero, there is a problem that the output voltage is distorted.

In addition to the three topologies mentioned above, there is a scheme to implement APD functions without using an auxiliary circuit but only by changing the control method. The paper [38] implemented the APD function by changing only the control method to the bridgeless SEPIC. There is an advantage that the manufacturing cost can be reduced because the auxiliary circuit is not needed and only the capacity of the components is changed in the existing circuit. However, this method has the problem that the buffer voltage must be

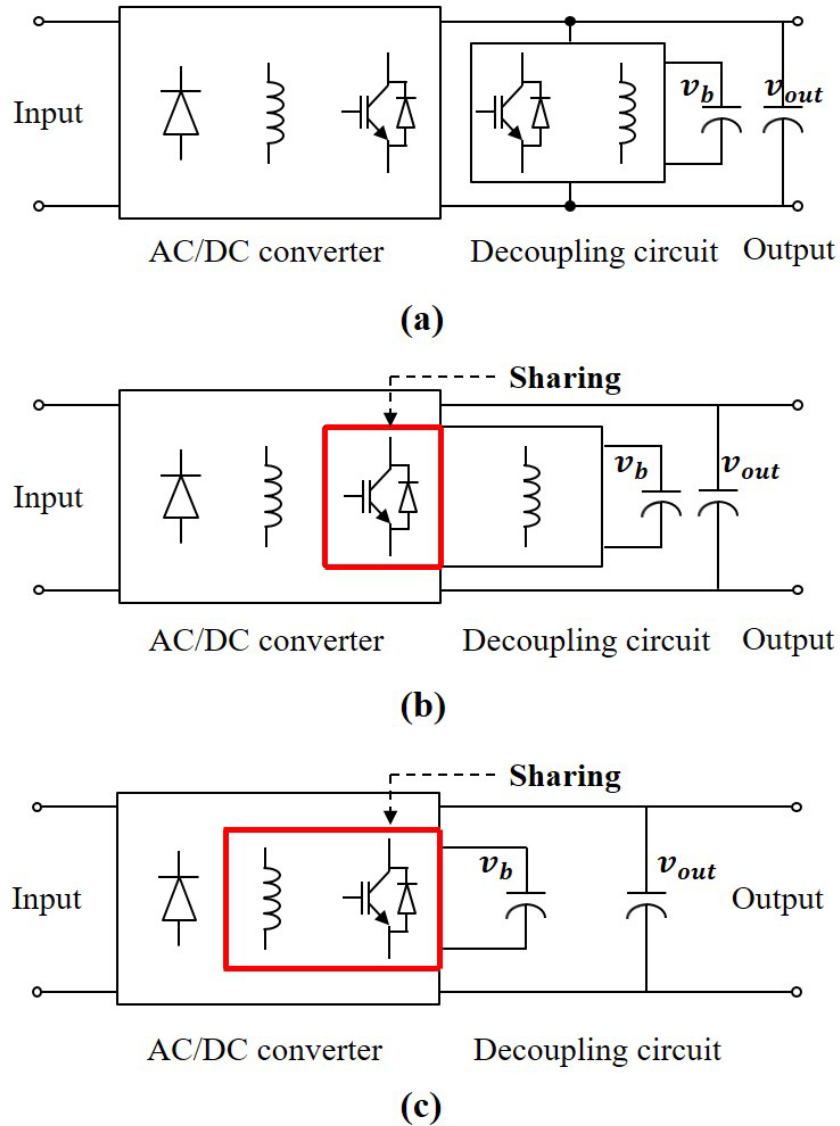


Figure 1.2: The combined structure of the APD circuit and the converter circuit, (A) independent decoupling topology, (b) switch multiplexing decoupling topology(c) switch and inductor multiplexing decoupling topology

higher than the output voltage for the operation of the APD function. This means that the volume of the buffer capacitor increases due to high voltage stress.

The control algorithms of the above-mentioned papers have the following problems in common. Due to the additional decoupling circuit, the complexity of the total circuit and the number of passive components are increased compared to conventional converters. Inductors and capacitors have relatively large manufacturing tolerances and highly non-linear characteristics. If the number of passive elements used increases, the process errors are overlapped and the uncertainty of the circuit model increases, which makes it difficult to

ensure the stability of the control. But the conventional control algorithms do not take these non-linearity and model uncertainties into account. When the actual parameters and designed parameters are mismatched, the performance of the APD function and its stability cannot be guaranteed.[20][21]

1.3 Structures and Characteristics of APD circuit for Single Phase AC/DC Converter

As shown in Fig. 1.3 the APD circuit can be divided into buck, boost, and buck-boost types according to the parts configuration of the APD circuit. The buck type decoupling circuit is characterized in that the buffer voltage is lower than the output voltage. This type has the advantages of low voltage stress on capacitors and switches, and limits the variation range of buffer voltage. The boost type is characterized in that the buffer voltage is higher than the output voltage. There is no limitation in the variation range of the buffer voltage. Therefore, theoretically, there is an advantage that the capacity of the capacitor required for decoupling can be greatly reduced. However, there is a problem that the voltage stress of the part increases, so the rated voltage of the part must be considered. The buck-boost type has the advantage that the buffer voltage can operate regardless of the output voltage. However, there is a disadvantage that the output is inverted with the input stage.

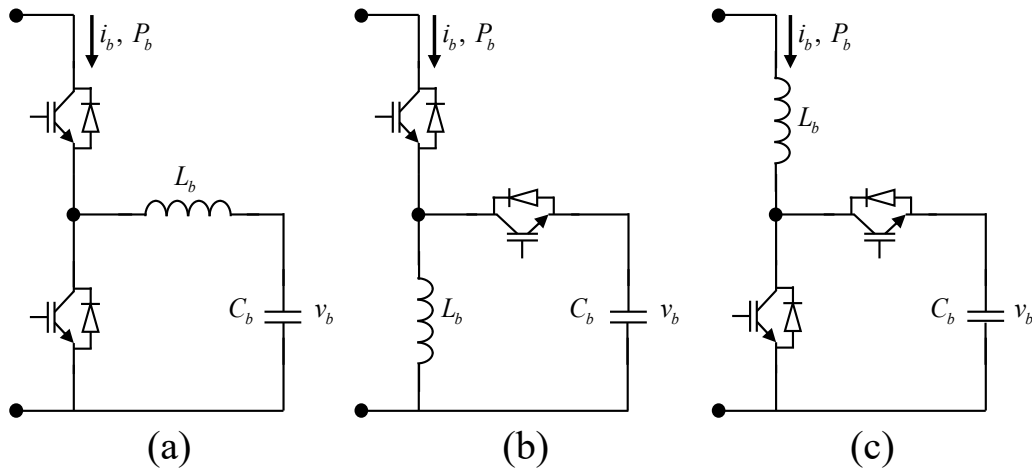


Figure 1.3: Three types of APD circuits, (A) buck type (b) buck-boost type (c) boost type

1.4 Optimized solution for robust operation and low voltage stress of APD circuit based converters

To solve the aforementioned problems, it is necessary to reduce the voltage stress of the APD circuit while also reducing the number of inductor cores. In addition, there is a need for a robust control strategy of the APD circuit to cope with the uncertainty due to an increase in the number of passive elements.

In order to reduce the voltage stress of the film capacitor, the APD operation should be performed even at the low buffer voltage. The proposed circuit used a coupled-inductor to construct the buck-boost APD circuit. In addition, the number of cores can be reduced by allowing the coupled-inductor to be shared between APD and converter circuits. One more switching element is needed than the switch and inductor multiplexing decoupling topology, but the voltage stress of the film capacitor is small, and the number of cores is reduced, which can reduce manufacturing cost and volume. The effective switching frequency is increased by applying interleave structure to reduce the size of input and output filters. The proposed circuit is modularized so that the interleaved structure can be easily applied. This technique can reduce the size of the input and output filters and distribute the weight of the coupled-inductors so that all components can be mounted on a single PCB. We also proposed a circuit to reduce the voltage stress of bridge-less SEPIC with APD function. By adding a diode to the existing circuit to prevent the flow of reverse current, the distortion of current and voltage that occurs when the APD function operates at low buffer voltage is prevented.

In order to guarantee the stability of the system even in the presence of uncertainty of the model, sliding mode control and Lyapunov function based control are applied. Assuming that uncertainties due to manufacturing tolerances and disturbances are limited, it is possible to ensure stability even under conditions where uncertainty exists, by determining appropriate gains to satisfy control stability. That is, the proposed control scheme guarantees stability and performance of control even when inductance and capacitance change due to external factors such as temperature and current.

1.5 Contributions

This study proposed the optimization and robust control technique of APD circuit. This makes it possible to reduce the manufacturing cost and improve the reliability of the control system. Three circuit design methods and two control strategies are proposed as follows.

1. **Independent decoupling plus Inductor multiplexing method:** The buck type APD circuit is applied to the buck-boost converter and the APD circuit and the converter circuit operate independently. In addition, the multiplexing scheme using a coupled-inductor is applied. With this proposed method, the number of magnetic cores and the voltage stress of the parts can be reduced. The effectiveness of the proposed method is verified by the prototype test and the proposed method has high power factor(98 % or higher) and low THD(less than 5 %). Maximum efficiency was 90.2 % under 100 W conditions. In addition, since the buffer voltage is lower than the output voltage, it is possible to use a component having a low rated voltage, which is advantageous in terms of volume and cost in comparison with the conventional method.

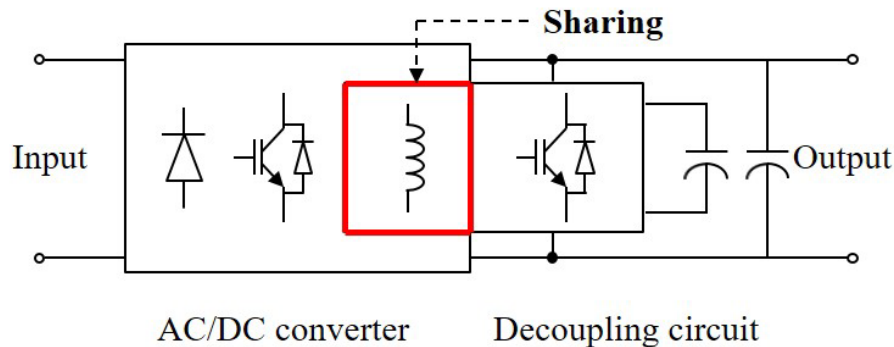


Figure 1.4: Proposed APD topology

2. **Modular design and interleaving structure of APD circuit based converter:** The buck-boost converter with APD function was designed as interleaving structure for the reduced size of input filters and higher power capability. In addition, APD circuits were modularized so that the number of phases could easily be increased and decreased. The sliding mode control strategy was modified so that it could be applied to multiple phases, making it easier to achieve scalability. Simulation results show that the proposed interleaved circuit can reduce the size of the input filter to 10% of that of the non - interleaved structure. In addition, it is possible to achieve high power capability by reducing current stress.

3. **Implement APD function for bridge-less SEPIC without auxiliary circuit** In order to solve the problem of model uncertainty due to the manufacturing error of the

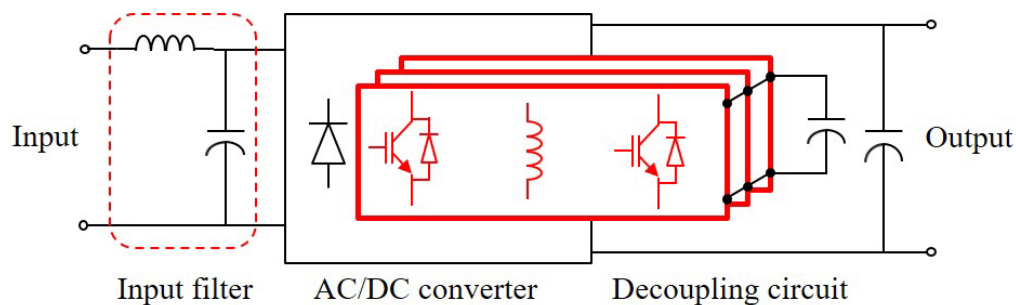


Figure 1.5: Proposed multi-phase interleaved APD topology

passive components, a Lyapunov function based control strategy is proposed. In addition, the current of the buffering inductor operates in a discontinuous conduction mode(DCM), thereby reducing the number of current sensors. This makes it possible to ensure stability and performance in disturbances such as voltage or load fluctuations, and reduces manufacturing costs. Compared to conventional PI-resonant controllers, it was verified that a smaller number of sensors had better transient response characteristics and a lower THD.

4. Robust control strategy of APD circuit based converter: SMC and Lyapunov function based control, which is a kind of nonlinear control technique, are applied to the control system of the APD circuits. The proposed control method guarantees stability and performance even in the presence of uncertainty such as parameter variation, disturbance and sensor noise. In addition, controller tuning is easy by suggesting selection criteria of design parameters based on control theory.

1.6 Thesis Organization

This thesis consists of the following contents. In Chapter 2, we define the frequently used symbols repeatedly in the paper and explain the operating principle and structural characteristics of the APD circuit. In Chapter 3, we introduce the SMC control strategy and the low-voltage stress inductor design for APD circuits. The effectiveness of the proposed circuit and control method is verified by simulation and prototype test. In Chapter 4, the performance of the controller is evaluated by applying Lyapunov function based control to the circuit proposed in Chapter 3. In Chapter 5, the circuit proposed in Chapter 3 is modularized for the interleaved structure and the suitable controller is introduced. In Chapter 6 and 7, we introduce a control method that implements the APD function without changing of the bridge-less SEPIC circuit. The effectiveness of the proposed method is verified by simulation and compared with the conventional control method. Finally, Chapter 8 discusses the issues covered in this thesis and discusses the things to be considered in implementing the proposed method and its future prospects.

CHAPTER 2

Preliminaries

In this chapter, we define commonly used notations throughout the paper before a full explanation. In addition, the operating principle and structural characteristics of the APD circuit are introduced.

List of Notations

v_b	Voltage of the buffer capacitor	v_{out}	Output voltage
v_{in}	Input voltage	i_{in}	Input current
i_{out}	Output current	i_m	Magnetizing current of the coupled-inductor
V_m	Magnitude of the input voltage	I_m	Magnitude of the input current
V_{out}^*	Target output voltage	V_b^*	Target buffer voltage
L_m	Magnetizing inductance of the coupled-inductor	C_{out}	Capacitance of the output capacitor
C_b	Capacitance of the buffer capacitor	ω	Angular velocity of the input voltage
P_{in}	Instantaneous input power	P_{out}	Instantaneous output power
T_s	Switching period	s	Sliding surface
$\alpha_1, \alpha_2, \rho, \delta$	Design parameters	$d_{sw1,2,3}$	Duty ratios of Q_1, Q_2, Q_3

2.1 Operation principle of the APD method

Assuming that input voltage(v_{in}) and current(i_{in}) have sinusoidal waveform and unity power factor, input power(P_{in}) can be calculated as:

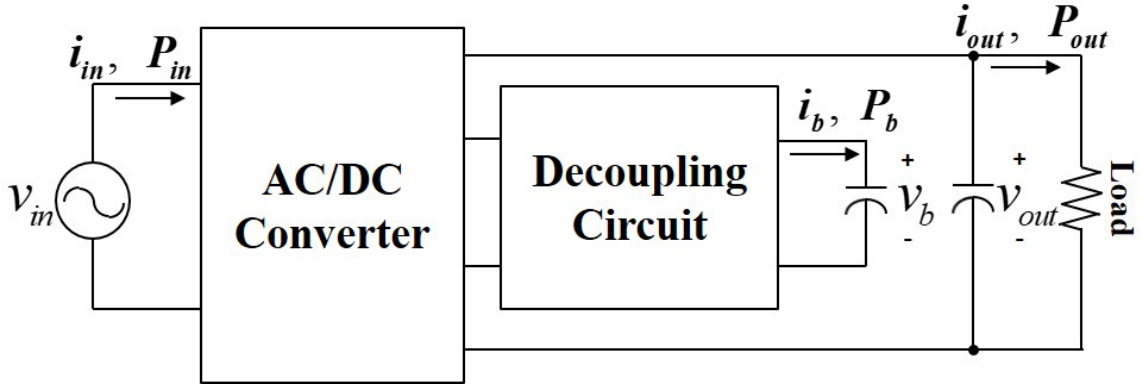


Figure 2.1: Basic active power decoupling topology

$$\begin{aligned}
 P_{in} &= v_{in}i_{in} = (V_m \sin \omega t) (I_m \sin \omega t) \\
 &= \underbrace{\frac{V_m I_m}{2}}_{P_{in_avg}} - \underbrace{\frac{V_m I_m}{2} \cos 2\omega t}_{P_{in_r}}
 \end{aligned} \tag{2.1}$$

where P_{in_avg} and P_{in_r} are the average and ripple input power values, respectively. To realize constant output power, a decoupling circuit like the one in Fig. 2.1 is used. The decoupling circuit actively controls the charging and discharging of the buffer capacitor to remove the ripple power P_{in_r} of (2.1). Assuming that the power loss in the circuit can be ignored, the output power(P_{out}) can be obtained as follows:

$$P_{out} = P_{in} - P_b = P_{in_avg} - P_{b_avg} \tag{2.2}$$

where

$$P_b = P_{b_avg} + P_{b_r}$$

P_b and P_{b_avg} are the total and average power of the buffer capacitor, respectively. Then, we can calculate P_{b_r} as follows:

$$P_{b_r} = -\frac{V_m I_m}{2} \cos 2\omega t \tag{2.3}$$

Using (2.3), the maximum energy charged in the buffer capacitor can be derived as

$$W_b = \int_{\frac{\pi}{4\omega}}^{\frac{3\pi}{4\omega}} P_{b_r} dt = \frac{V_m I_m}{2\omega} = \frac{P_{out}}{\omega} \tag{2.4}$$

When the energy is charged in the buffer capacitor, the following equation holds:

$$W_b = \frac{1}{2}C_b V_{b_max}^2 - \frac{1}{2}C_b V_{b_min}^2 \quad (2.5)$$

where V_{b_max} and V_{b_min} are the maximum and minimum voltage of the buffer capacitor, respectively. Using (2.4) and (2.5), the required minimum capacitance for decoupling function can be derived as

$$C_b = \frac{2P_{out}}{\omega(V_{b_max}^2 - V_{b_min}^2)} = \frac{P_{out}}{\omega V_{b_avg} \Delta V_b} \quad (2.6)$$

where

$$\Delta V_b = V_{b_max} - V_{b_min}, \quad V_{b_avg} = \frac{V_{b_max} + V_{b_min}}{2}$$

ΔV_b and V_{b_avg} are fluctuating voltage range and the average voltage of the buffer voltage,

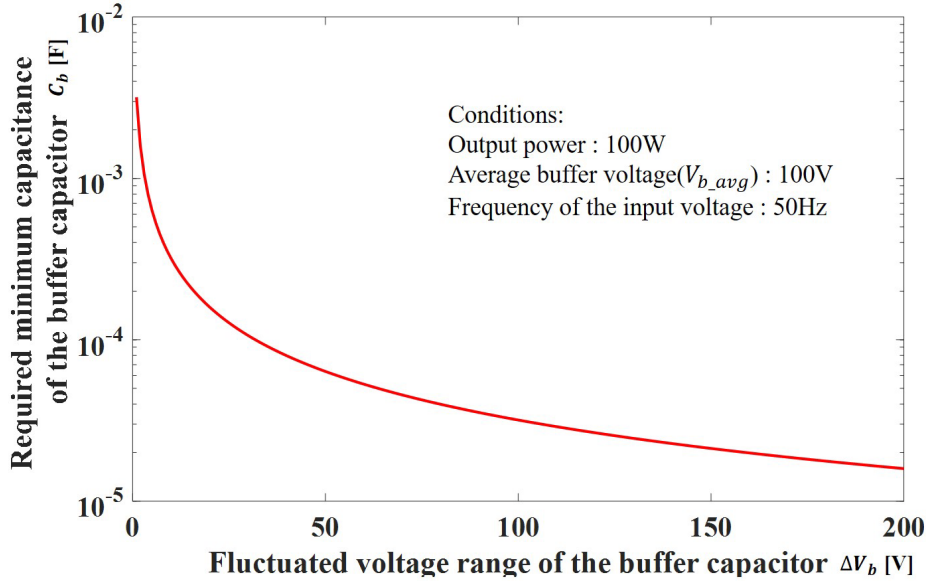


Figure 2.2: Required minimum capacitance

respectively. As shown in Fig. 2.2, the required minimum capacitance is reduced as fluctuating voltage range is increased, which means that we can remove the ripple power from the grid power system using a small capacitor by actively controlling the buffer voltage.

All of the operations and waveforms of the APD method are described in Fig. 2.3. If (2.3) is negative, it means that the buffer capacitor has been discharged and its energy transferred from the decoupling circuit to the output terminal. Otherwise, if (2.3) is positive, the decoupling circuit charges the buffer capacitor to store excess energy from the grid power system. Using this control, ripple power(P_{in_r}) from the input terminal is eliminated by the decoupling circuit.

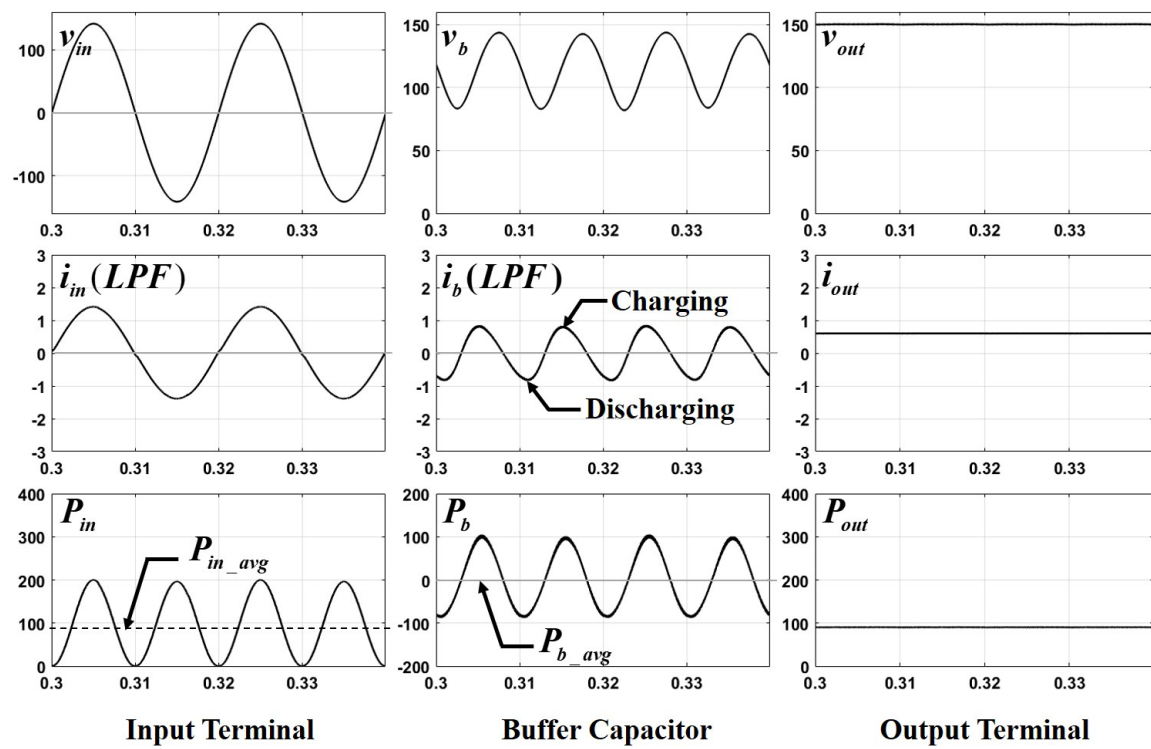


Figure 2.3: Key waveforms of the ideal AC-DC converter applied to the decoupling circuit

CHAPTER 3

Independent decoupling plus Inductor multiplexing method

In this section, we propose a new APD circuit to solve the problems of the conventional switch and inductor multiplexing method.

3.1 Contribution Summary

Fig. 3.1 shows the capacitor per volume ratio of film capacitors according to the rated voltage. As shown in the figure, as the rated voltage of the film capacitor increases, the volume increases and the price becomes higher. That is, it is necessary to lower the rated voltage of the film capacitor in order to miniaturize the circuit and reduce the manufacturing cost. The proposed circuit applied independent decoupling method with three switches, which

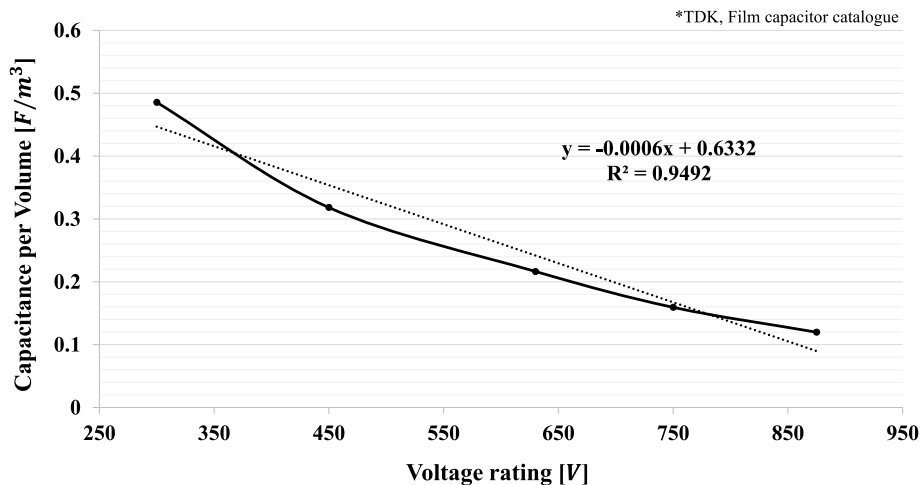


Figure 3.1: Capacitance per volume ratio of film capacitor according to rated voltage

reduces the voltage stress on each IGBT and capacitor. Also, the number of magnetic cores can be reduced by applying inductor-multiplexing scheme using a coupled-inductor. Sliding mode control scheme is applied to guarantee stability under that the model uncertainties

and non-linearities in APD circuit. Owing to the above contributions, long lifespan, low voltage stress, and robust operation of the buck-boost converter can be realized.

3.2 Proposed APD circuit

Fig. 3.2 describes the buck-boost converter circuit with the proposed APD topology in discontinuous conduction mode(DCM). In the proposed topology, the buck-boost converter and the decoupling circuit share the coupled-inductor whereas conventional APD topology uses two inductors.

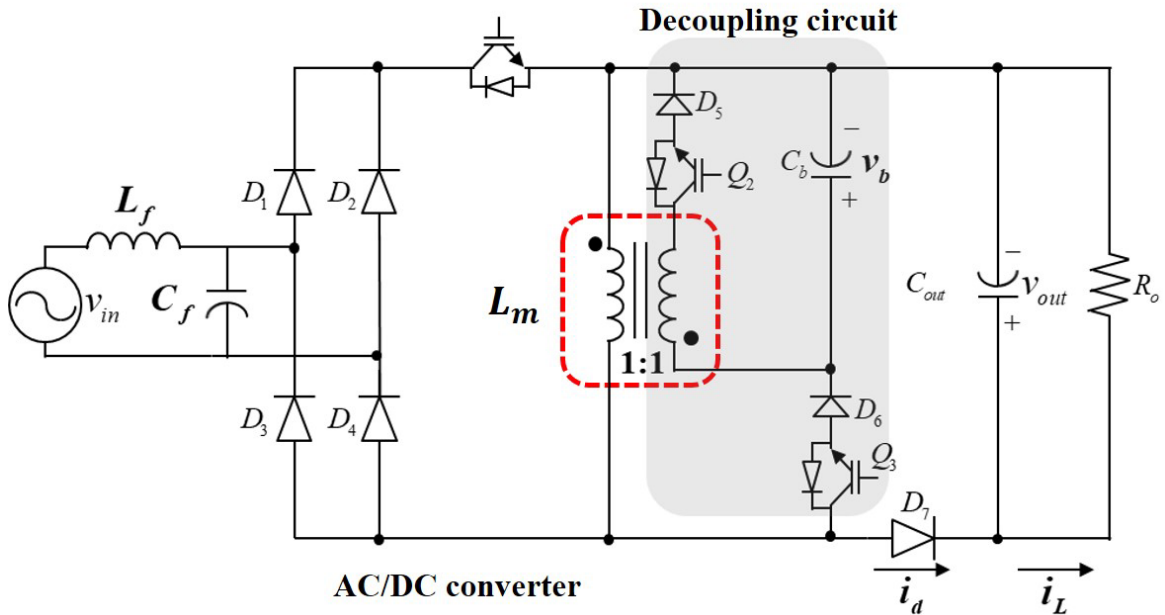


Figure 3.2: The proposed buck-boost converter with the APD circuit

3.2.1 Basic operation of the proposed circuit

Fig. 3.3 shows the operation modes and current flow. The proposed circuit can be operated in 4 different modes, each of which is controlled by a unique combination of switch orientations.

Chapter 3. Independent decoupling plus Inductor multiplexing method 16

State1. All switches (Q_1, Q_2, Q_3) are off and stored energy in the coupled-inductor is discharged to the output terminal through diode D_7 .

State2. Switch1(Q_1) is on and the other switches (Q_2, Q_3) are off. The primary side of the

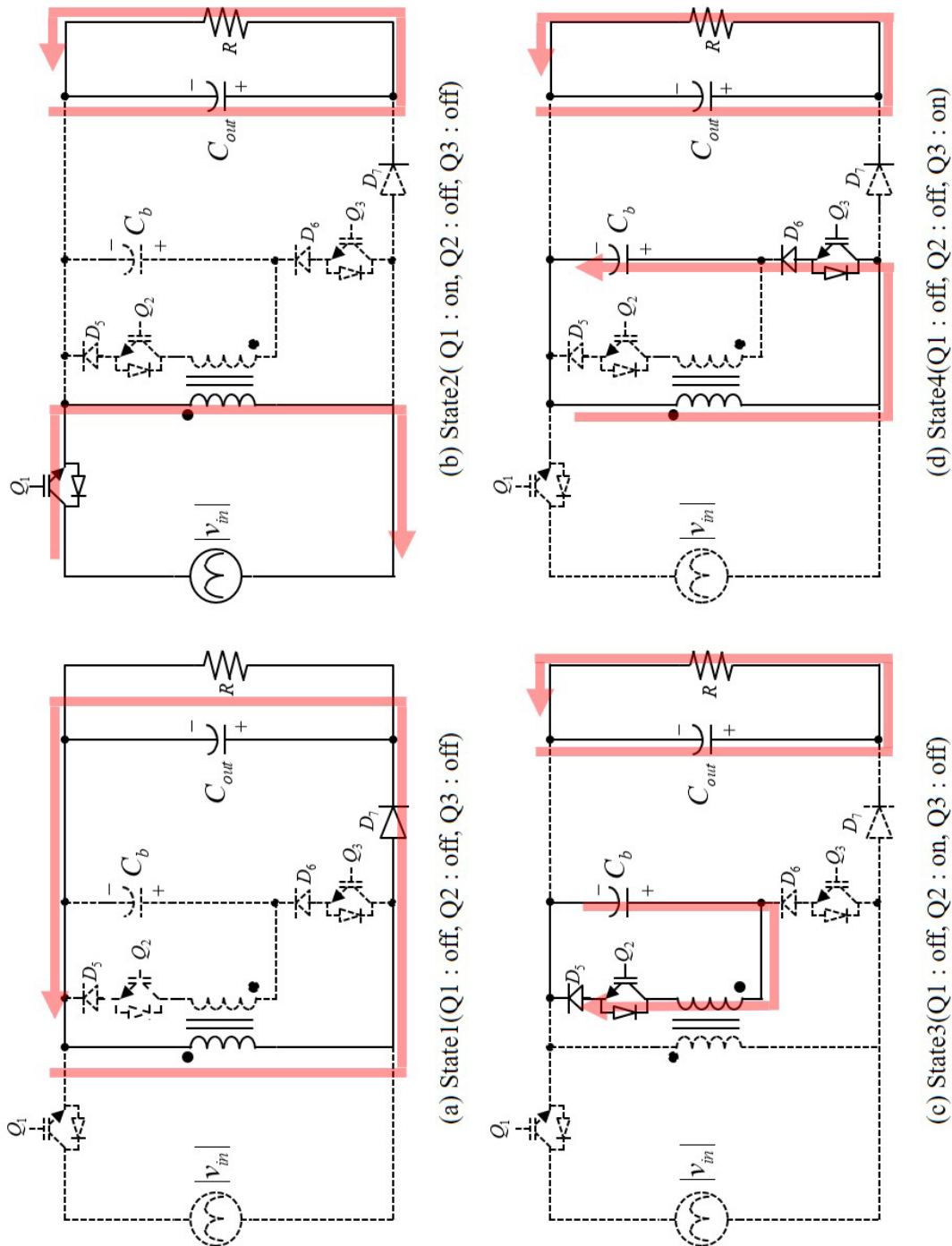


Figure 3.3: Current flows for each switch combination: (a) State1, (b) State2, (c) State3, and (d) State4

Chapter 3. Independent decoupling plus Inductor multiplexing method 17

coupled-inductor is charged by the energy from the power system.

State3. Switch2(Q_2) is on and the other switches (Q_1, Q_3) are off. The decoupling circuit works as a fly-back converter. Stored energy in the buffer capacitor is transferred from the secondary side to the primary side of the coupled-inductor.

State4. Switch3(Q_3) is on and the other switches (Q_1, Q_2) are off. Stored energy in the primary side of the coupled-inductor moves to the buffer capacitor when the voltage of the buffer capacitor is below the output voltage.

The conventional buck-boost converter circuit feeds input power to the output terminal using **State1** and **State2** operation modes, although this generates power pulsation with twice the frequency of the input voltage. The decoupling circuit actively operates to absorb and release this pulsed power to make the output power constant. When the input power is below the target output power, **State3** is operated to release the energy stored in the buffer capacitor. Using this operation, insufficient energy is compensated. When the input power is higher than the target output power, **State4** is operated to absorb the excess energy and store it in the buffer capacitor.

3.2.2 Modulation Strategy of the Proposed Converter

As shown in Fig. 3.4, the proposed circuit has two control operations: discharging and charging. These operations are comprised of different combinations of each switching state mentioned in section 3.1. For the implementation of this operation, different pulse width modulation(PWM) output methods for each state were applied as follows:

State2

$$T[n] \leq T_{max}(1 - d_{sw1}) \rightarrow Q_1 : \mathbf{Turn\ on(1)}$$

$$T[n] > T_{max}(1 - d_{sw1}) \rightarrow Q_1 : \mathbf{Turn\ off(0)}$$

State3: Discharging

$$T[n] \geq T_{max}d_{sw2} \rightarrow Q_2 : \mathbf{Turn\ on(1)}$$

$$T[n] < T_{max}d_{sw2} \rightarrow Q_2 : \mathbf{Turn\ off(0)}$$

State4: Charging

$$T[n] \geq T_{max}d_{sw3} \rightarrow Q_3 : \mathbf{Turn\ on(1)}$$

$$T[n] < T_{max}d_{sw3} \rightarrow Q_3 : \mathbf{Turn\ off(0)}$$

where $T[n]$ and T_{max} are the current and maximum interrupt counts of a 16-bit timer,

respectively. While the proposed circuit works under the discharging operation, the circuit generates a PWM pattern as shown in Fig. 3.4(a). Each switch is changed in the order of **State1**, **State2**, and **State3**, and this procedure is repeated until the discharging operation is completed. Fig. 3.4(b) shows the switching pattern under the charging operation. Each switch is changed in the order of **State1**, **State2**, and **State4**, and this procedure is repeated until the charging operation has completed.

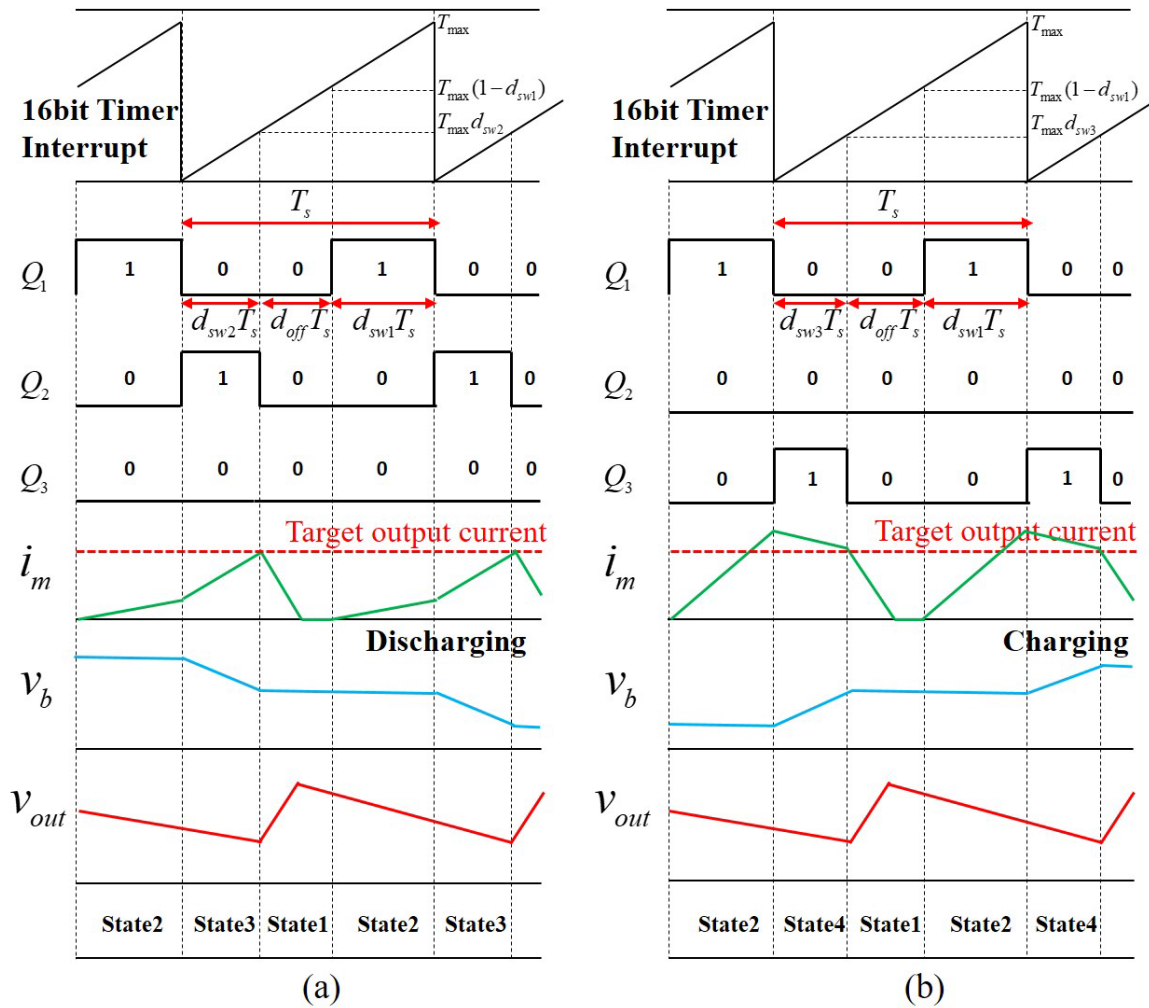


Figure 3.4: Switching pattern (a) discharging operation, (b) charging operation

3.3 Control System

Passive components have manufacturing tolerances in mass production. Especially in the case of inductors and transformers, there exist errors in the tensile force of windings, the size of the air-gap, and materials of the core. Thus, inductors and transformers with a significant difference from the design value can be produced. Therefore, for circuits that use many passive components with large tolerances, the error is superimposed, which increases the uncertainty of the model. Compared with conventional buck-boost converters with APD circuits are complex in structure and use a large number of passive components. Therefore, appropriate control methods are needed to consider characteristics of the APD circuit. In this paper, the proposed control system consists two parts, which are buffer voltage and and APD controller. To guarantee the stability and regulation performance of the output voltage, we applied a sliding mode control scheme in the proposed circuit.

3.3.1 Buffer voltage control

The object of buffer voltage control is to regulate the V_b and generate sinusoidal input current waveform for the unity power factor. V_b is the root mean square(RMS) value of v_b . At steady-state conditions and neglecting circuit loss, the power of each stage in the proposed converter can be derived as follows,[22]

$$P_{in_avg} + P_{in_r} = P_{out} + P_{b_r} + P_{b_avg} \quad (3.1)$$

Assuming that ripple power is removed by the decoupling circuit, we can eliminate P_{in_r} and P_{b_r} in (3.1) to give

$$P_{in_avg} = \frac{V_m I_m}{2} = P_{out} + P_{b_avg} \quad (3.2)$$

If the proposed converter works in DCM, I_m can be rewritten as

$$\begin{aligned} i_{in_peak} &= \frac{V_m \sin \omega t}{L_m} T_s d_{sw1} \\ i_{in}^- &= \frac{1}{T_s} \left(\frac{i_{in_peak}}{2} \right) T_s d_{sw1} = \frac{V_m d_{sw1}^2 T_s}{2L_m} \sin \omega t = I_m \sin \omega t \end{aligned} \quad (3.3)$$

$$I_m = \frac{V_m d_{sw1}^2 T_s}{2L_m} \quad (3.4)$$

where i_{in_peak} shown in Fig. 3.6 is the peak value of the instantaneous input current, and i_{in}^- is the average input current. According to (3.3), under the condition that d_{sw1} is unchanged, the average input current(i_{in}^-) has the same phase as the input voltage. Using (3.2) and

Chapter 3. Independent decoupling plus Inductor multiplexing method 20

(3.4), we can calculate the duty ratio of Q1 as

$$d_{sw1} = \sqrt{\frac{4L_m(P_{out} + P_{b_avg})}{V_m^2 T_s}} \quad (3.5)$$

P_{b_avg} can be regarded as the control input for regulating V_b . In order to control V_b , we use a simple proportional-integral controller:

$$P_{b_avg} = K_p(V_b^* - V_b) + K_i \int (V_b^* - V_b) dt \quad (3.6)$$

where V_b^* is the target RMS buffer voltage. The moving RMS is implemented in the control system to obtain V_b at time k as follows:

$$V_b(k) = \sqrt{\frac{1}{M} \sum_{i=0}^{M-1} v_b^2(k-i)} \quad (3.7)$$

where M is the number of points in the moving RMS. Assuming that P_{out} and P_{b_avg} are at steady state, then d_{sw1} is unchanged. Thus, the phase of \bar{i}_{in} is the same as for the input voltage, and due to this reason, the unity power factor and a sinusoidal wave form are achieved without harmonic distortion.

3.3.2 Active power decoupling control

The main purpose of APD control is to remove ripple power in input power using the actively controlled switches. In order to make the operation robust, a sliding mode control(SMC) scheme is used, which is a useful nonlinear control method to take into account model uncertainties and disturbances. [23][24]

3.4 Sliding Mode Control Algorithm

The control mechanism of SMC can explain as following two control phases. First is a reaching phase that moves the states in the small vicinity of a sliding surface. Suppose that the sliding surface are defined as follows:

$$s = x_1 + \alpha x_2$$

Chapter 3. Independent decoupling plus Inductor multiplexing method 21

where α is a gradient of the sliding surface. If the switching control law meets the following conditions, the reachability of surface s is ensured in finite time.

$$u = \begin{cases} u+ & \text{if } s > 0, \text{ which gives } \dot{s} < 0. \\ u- & \text{if } s < 0, \text{ which gives } \dot{s} > 0. \end{cases}$$

As shown Fig. 3.5, the states in $s < 0$ plane move to the sliding surface by applying switching control input $u-$ during reaching control phase. Second is a sliding phase that the state trajectory stays on the sliding surface by applying equivalent control input which makes $\dot{s} = 0$. As shown in Fig. 3.5, once the states reach on the sliding surface, the states move according to the designed control law without being affected by uncertainty.

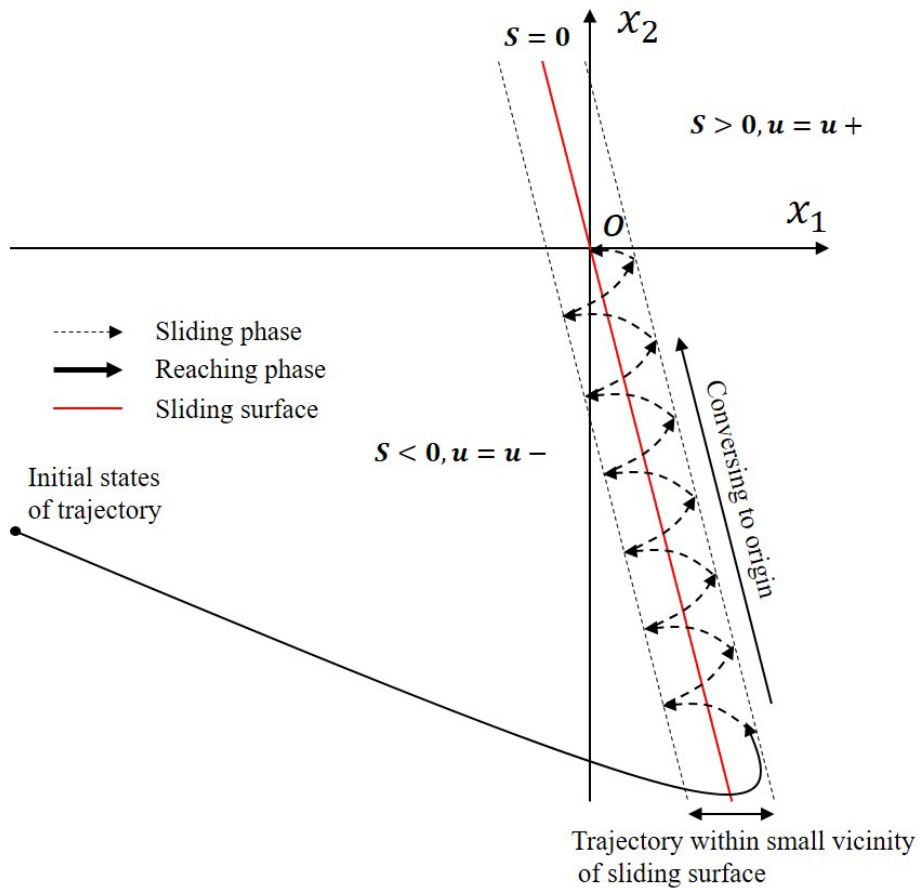


Figure 3.5: State trajectories of each control phases

There are two main advantages of sliding mode control. First is that the closed loop response becomes insensitive to uncertainties. Therefore, the stability and control performance of the system can be ensured even in the case where parameter uncertainties and disturbances exist and the nonlinearity is large. Secondly, the closed-loop response is the fastest possible response since it provides control inputs that can be fed directly into the converters without

Chapter 3. Independent decoupling plus Inductor multiplexing method 22

any supplementary modulation operation.[25] From a practical point of view, the SMC allows for controlling nonlinear system subject to disturbances and model uncertainties such as the APD circuit.

Proposed SMC strategy for APD

To make the output voltage constant and converge it to a reference value, we decided each state as follows

$$x_1 = v_{out} - V_{out}^*, \quad x_2 = \int x_1 dt \quad (3.8)$$

For easy implementation on a real system, we consider the sliding surface as a linear combination of the state variables, described in (3.8). Thus, we can specify the sliding surface as

$$s = \alpha_1 x_1 + \alpha_2 x_2 \quad (3.9)$$

Next, we define a Lyapunov candidate function as

$$V(s) = \frac{1}{2} s^2 \quad (3.10)$$

then to guarantee system stability and convergence of the state space trajectory to the sliding surface s , derivatives of the sliding surface should satisfy the following condition.

$$\dot{V}(s) = s\dot{s} < 0, \text{ if } s \neq 0 \quad (3.11)$$

Using (3.9), \dot{s} can be calculated as

$$\dot{s} = \alpha_1 \dot{v}_{out} + \alpha_2 x_1 = \alpha_1 \frac{\bar{i}_d - i_{out}}{C_{out}} + \alpha_2 x_1 \quad (3.12)$$

where \bar{i}_d and i_{out} are the average value of diode D_7 's current and output current, respectively. To calculate the equivalent control input, we can obtain the following equation under condition $\dot{s}(x) = 0$:

$$\bar{i}_d = -\frac{\alpha_2 C_{out} x_1}{\alpha_1} + i_{out} \quad (3.13)$$

The \bar{i}_d in equation (3.13) can be expressed using v_{in} , v_b , v_{dc} and duties as shown in Fig 3.6. Thus, \bar{i}_d can be derived as follows:

$$\bar{i}_d = \frac{1}{T_s} \int i_d(t) dt = \frac{d_{off} T_s}{2T_s} i_{d_peak} \quad (3.14)$$

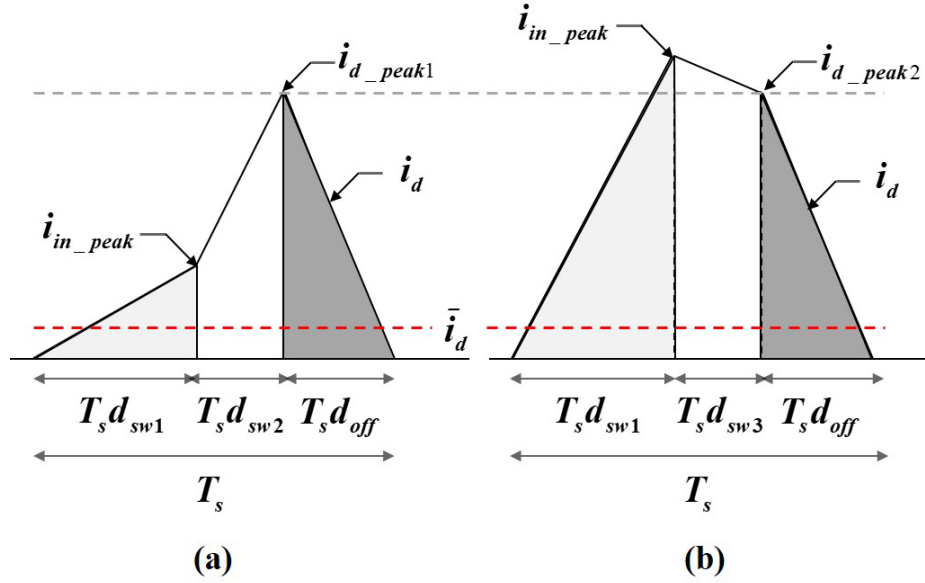


Figure 3.6: Magnetization current shapes in (a) discharging operation and (b) charging operation

where \bar{i}_d , i_d and i_{d_peak} are the average, instantaneous, and peak values of the diode current, respectively. Since the proposed circuit works in DCM, the i_{d_peak} can be written as

$$i_{d_peak1} = \frac{v_{in}}{L_m} d_{sw1} T_s + \frac{v_b}{L_m} d_{sw2} T_s \quad (3.15)$$

$$i_{d_peak2} = \frac{v_{in}}{L_m} d_{sw1} T_s - \frac{v_b}{L_m} d_{sw3} T_s \quad (3.16)$$

where i_{d_peak1} and i_{d_peak2} are the peak values of the diode current under the discharging and charging operations, respectively. By applying a temporary control input d_{temp} in (3.15) and (3.16), we can obtain a simple equation as follows:

$$i_{d_peak} = \frac{v_{in}}{L_m} d_{sw1} T_s + \frac{v_b}{L_m} d_{temp} T_s \quad (3.17)$$

where

$$-1 \leq d_{temp} \leq 1$$

Substituting (3.17) into (3.14) yields,

$$\bar{i}_d = \frac{d_{off}}{2} \left(\frac{v_{in}}{L_m} d_{sw1} T_s + \frac{v_b}{L_m} d_{temp} T_s \right) \quad (3.18)$$

Chapter 3. Independent decoupling plus Inductor multiplexing method 24

Control input d_{off} cannot also be directly manipulated, thus should be changed to a controllable value such as d_{sw1} or d_{temp} . In DCM, d_{off} can be redefined as

$$\begin{aligned} v_{out} &= L_m \frac{di_d}{dt} = L_m \frac{i_{d_peak}}{T_s d_{off}} \\ d_{off} &= L_m \frac{i_{d_peak}}{T_s v_{out}} \end{aligned} \quad (3.19)$$

Substituting (3.17) into (3.19) yields

$$\begin{aligned} d_{off} &= \frac{L_m}{T_s v_{out}} \left(\frac{v_{in}}{L_m} d_{sw1} T_s + \frac{v_b}{L_m} d_{temp} T_s \right) \\ &= \frac{v_{in} d_{sw1} + v_b d_{temp}}{v_{out}} \end{aligned} \quad (3.20)$$

By substituting (3.20) into (3.18), we obtain

$$\begin{aligned} \bar{i}_d &= \frac{v_{in} d_{sw1} + v_b d_{eq}}{2v_{out}} \left(\frac{v_{in}}{L_m} d_{sw1} T_s + \frac{v_b}{L_m} d_{temp} T_s \right) \\ &= \frac{T_s}{2L_m v_{out}} (v_{in} d_{sw1} + v_b d_{temp})^2 \end{aligned} \quad (3.21)$$

and by substituting (3.21) into (3.12), the \dot{s} can be rewritten as

$$\dot{s} = \frac{\alpha_1 T_s}{\alpha_2 L_m v_{out} C_{out}} (v_{in} d_{sw1} + v_b d_{temp})^2 - \frac{\alpha_1 i_{out}}{C_{out}} + \alpha_2 x_1 \quad (3.22)$$

The d_{temp} consists an equivalent control input d_{eq} and a switching control input u_{sw} . Using (3.22), d_{eq} in sliding mode, in which $\dot{s}(x) = 0$, can be calculated as

$$d_{eq} = \frac{1}{v_b} \sqrt{-\frac{2\alpha_2 L_m C_{out} x_1 v_{out}}{\alpha_1 T_s} + \frac{2L_m P_{out}}{T_s}} - \frac{v_{in}}{v_b} d_{sw1} \quad (3.23)$$

where

$$P_{out} = i_{out} v_{out}.$$

According to (3.11), $\dot{V}(s)$ should always be negative in order to guarantee controller stability and convergence to the sliding surface. To satisfy this condition, a saturation function is used as u_{sw} as follows:

$$u_{sw} = \rho \text{sat} \left(\frac{s}{\delta} \right) = \begin{cases} \rho \frac{s}{\delta} & \text{if } |s| \leq \delta \\ \rho & \text{if } s > \delta \\ -\rho & \text{if } s < -\delta \end{cases} \quad (3.24)$$

Chapter 3. Independent decoupling plus Inductor multiplexing method 25

where δ represents the thickness of boundary layers of the sliding surface and ρ is the control gain of the switching input. The function of these parameters will be described in section 5. According to (3.22), d_{temp} is included in squared term. Thus, the switching control input in (3.24) is added in the square root term of (3.23) for simplification. Subsequently, the final input of the proposed control system can be derived as

$$d_{temp} = \frac{1}{v_b} \sqrt{-\frac{2\alpha_2 L_m C_{out} x_1 v_{out}}{\alpha_1 T_s} + \frac{2L_m P_{out}}{T_s} - \rho \text{sat}\left(\frac{s}{\delta}\right) - \frac{v_{in}}{v_b} d_{sw1}} \quad (3.25)$$

and $\dot{V}(s)$ is calculated as

$$\begin{aligned} \dot{V}(s) &= s\dot{s} \\ &= s \left(\frac{\alpha_1 T_s}{2L_m v_{out} C_{out}} (v_{in} d_{sw1} + v_b d_{temp})^2 - \frac{\alpha_1 i_{out}}{C_{out}} + \alpha_2 x_1 \right) \\ &= s \left(0 - \frac{\alpha_1 \rho T_s}{2L_m v_{out} C_{out}} \text{sat}\left(\frac{s}{\delta}\right) \right) < 0 \end{aligned} \quad (3.26)$$

after which, the necessary condition to ensure the control stability and convergence to the sliding surface can be derived as

$$-\frac{\alpha_1 \rho T_s}{2L_m v_{out} C_{out}} |s| < 0, \text{ if } |s| > \delta \quad (3.27)$$

$$-\frac{\alpha_1 \rho T_s}{2L_m v_{out} C_{out}} \frac{s^2}{\delta} < 0, \text{ if } |s| \leq \delta \quad (3.28)$$

If design parameters α_1 , ρ , and δ have positive values when $s \neq 0$, then (3.27) and (3.28) are always negative.

Conditions for the existence of the sliding mode

For the afore-mentioned control input to be valid, d_{sw1} , d_{temp} , and d_{off} must exist between 0 and 1, and as proposed control system works under DCM, their summation must also satisfy the following inequality constraint:

$$0 \leq d_{sw1} + |d_{temp}| + d_{off} \leq 1 \quad (3.29)$$

Using equation (3.20), inequality (3.29) can be derived as the following inequality consisting of d_{sw1} and d_{temp} :

$$0 \leq (v_{out} + v_{in})d_{sw1} + \left(v_{out} \frac{|d_{temp}|}{d_{temp}} + v_b \right) d_{temp} \leq v_{out} \quad (3.30)$$

Chapter 3. Independent decoupling plus Inductor multiplexing method 26

Under the discharging condition, d_{temp} is positive, so (3.30) can be rewritten as

$$0 \leq (v_{out} + v_s)d_{sw1} + (v_{out} + v_b)d_{temp} \leq v_{out} \quad (3.31)$$

Assuming all the states are on the sliding surface($s = 0$), then we can obtain

$$\begin{aligned} d_{temp} &= \frac{1}{v_b} \sqrt{-\frac{\alpha_2 L_m C_{out} x_1 v_{out}}{\alpha_1} + \frac{2L_m P_{out}}{T_s} - \rho_{sat} \left(\frac{s}{\delta} \right)} \\ &\quad - \frac{v_{in}}{v_b} d_{sw1} \\ &\approx \frac{1}{v_b} \sqrt{\frac{2L_m P_{out}}{T_s}} - \frac{v_{in}}{v_b} d_{sw1} \end{aligned} \quad (3.32)$$

By substituting (3.32) into (3.31), (3.31) can be rewritten as

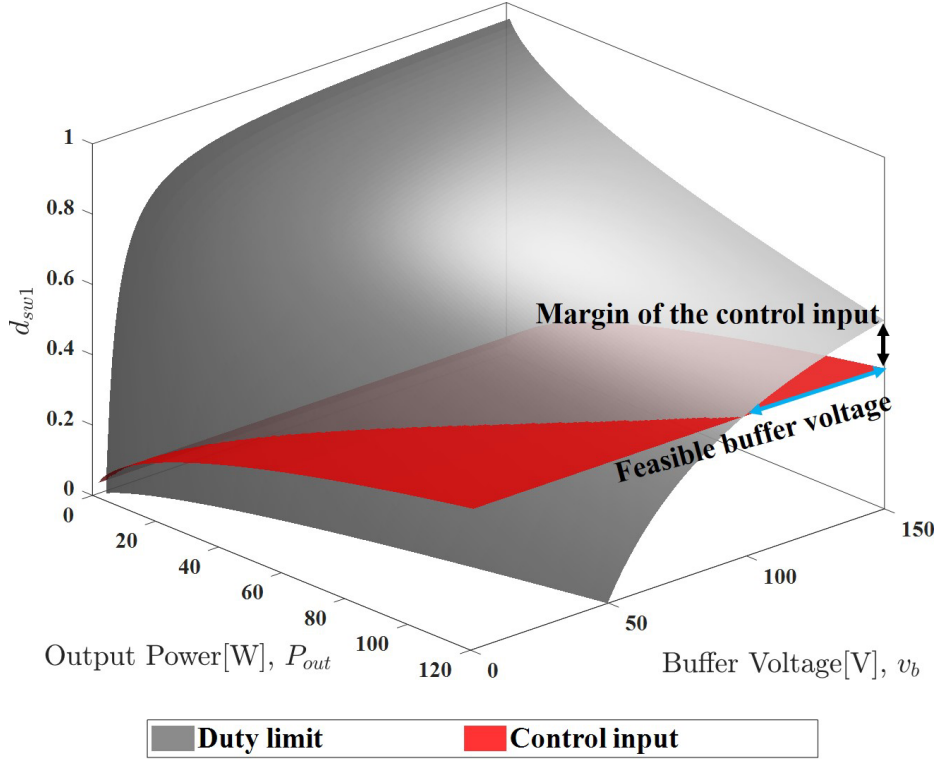


Figure 3.7: Existence region of the sliding motion during the discharging operation ($v_{out} = 150V$, $v_{in} = 0V$)

$$0 \leq d_{sw1} \leq \frac{1}{(v_b - v_{in})} \left(v_b - \frac{v_{out} + v_b}{v_{out}} \sqrt{\frac{2L_m P_{out}}{T_s}} \right) \quad (3.33)$$

In the discharge mode, a worst case is $v_{in} = 0$ where the instantaneous input power is the lowest. Using (3.5) and (3.33), we can describe a feasible buffer voltage region to satisfy (3.29) under the worst case, as shown in Fig. 3.7.

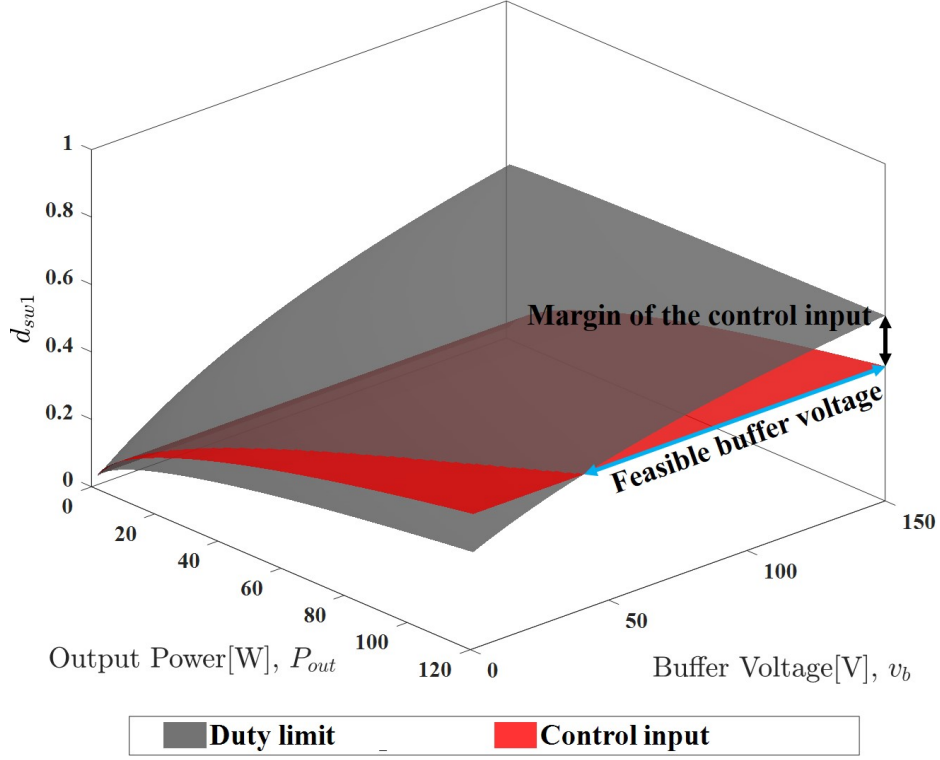


Figure 3.8: Existence of the sliding motion region during the charging operation ($v_{out} = 150$ V and $v_{in} = 141$ V)

Under the charging condition, d_{temp} is negative, so inequality constraint (3.7) can be rewritten as

$$0 \leq (v_{out} + v_{in})d_{sw1} - (v_{out} - v_b)d_{temp} \leq v_{out} \quad (3.34)$$

By substituting (3.32) into (3.34), inequality condition (3.34) becomes

$$0 \leq d_{sw1} \leq \frac{1}{(v_b + v_{in})} \left(v_b + \frac{v_{out} - v_b}{v_{out}} \sqrt{\frac{2L_m P_{out}}{T_s}} \right) \quad (3.35)$$

In the charge mode, a worst case is $v_{in} = 141$ where the instantaneous input power is the highest. we can obtain a feasible region to ensure the sliding mode under the worst case, as shown in Fig. 3.8.

The gray areas of each Figs. 3.7 and 3.8 represent the limits of duty to operate with DCM, and the red areas indicate the duty obtained from (3.5). Each blue line indicates a feasible buffer voltage region that satisfy (3.29). As the output power increases, the feasible buffer voltage region decreases. To ensure the sliding motion, v_b should be controlled within

Chapter 3. Independent decoupling plus Inductor multiplexing method 28

these feasible regions, and for this reason, deciding on an appropriate reference value for the buffer voltage is important. The following equation describes P_b and the energy of the buffer capacitor (W_b) counterparts when the power pulsation is compensated for by the decoupling circuit:

$$W_b = \int_{t_0}^t P_b dt = \frac{1}{2} C_b v_b^2(t) - \frac{1}{2} C_b v_b^2(t_0) \quad (3.36)$$

(3.36) can be rewritten using (2.3) as

$$\begin{aligned} W_b &= -\frac{P_{out}}{2\omega} (\sin 2\omega t - \sin 2\omega t_0) \\ &= \frac{1}{2} C_b v_b^2(t) - \frac{1}{2} C_b v_b^2(t_0) \end{aligned} \quad (3.37)$$

Assume that $\sin 2\omega t_0$ is 0, then $v_b(t_0)$ can be regarded as V_b . Subsequently, v_b can be derived using (3.37) as

$$v_b = \sqrt{V_b^2 - \frac{P_{out}}{\omega C_b} \sin 2\omega t} \quad (3.38)$$

Using (3.38), we can estimate the voltage range of v_b . As shown in Figs. 3.7 and 3.8, it is better for v_b to exist in the vicinity of the output voltage to maximize the operational range. Assuming that $\sin 2\omega t$ is -1, v_b reaches its maximum value v_{b_max} , then the reference buffer voltage V_b^* which can maximize the operational range can be derived as follows:

$$\begin{aligned} v_{b_max} &= V_{out}^* = \sqrt{(V_b^*)^2 + \frac{P_{out}}{\omega C_b}} \\ V_b^* &= \sqrt{(V_{out}^*)^2 - \frac{P_{out}}{\omega C_b}} \end{aligned} \quad (3.39)$$

Fig. 3.9 represents the overall control systems of the proposed converter. The final duty ratios of Q_2 and Q_3 are decided by the table in Fig. 3.9.

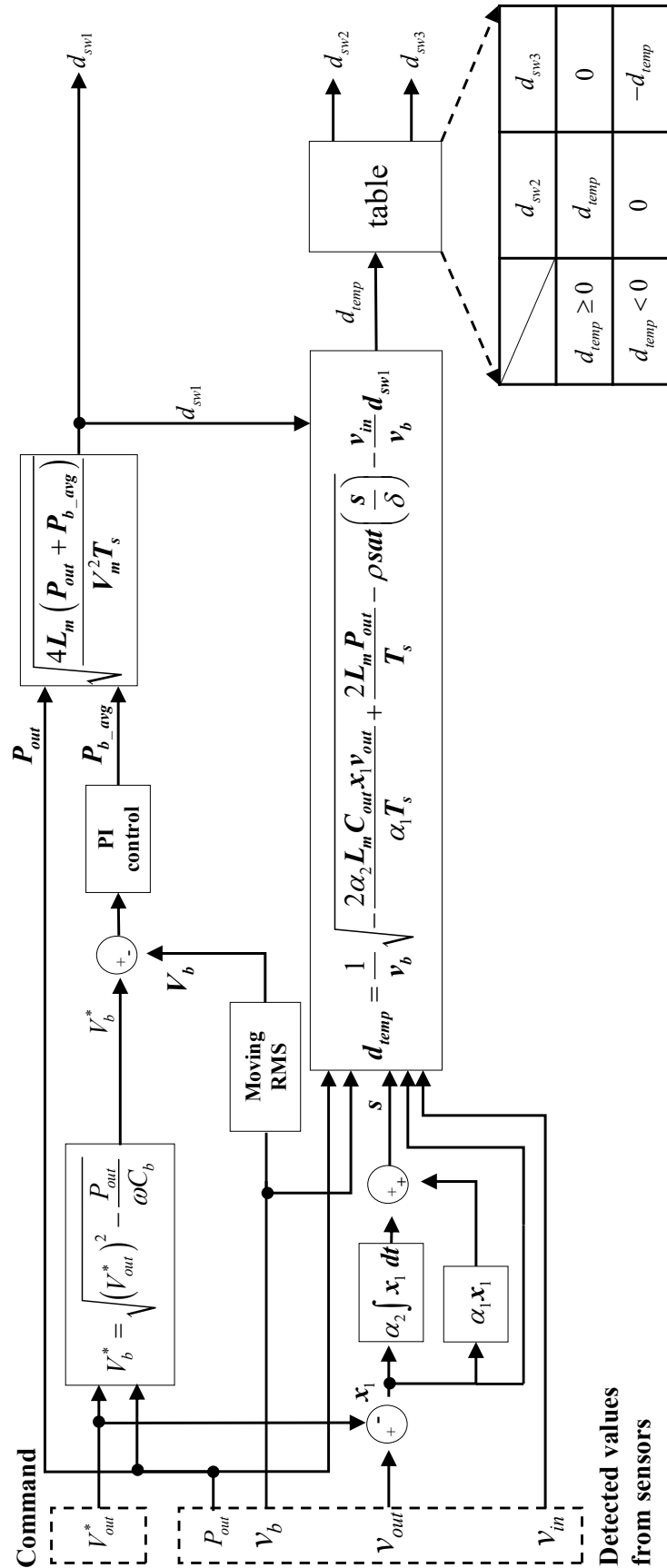


Figure 3.9: Overall control scheme of the proposed converter

Chapter 3. Independent decoupling plus Inductor multiplexing method 30

Parameter selection for the proposed SMC

The important parameters of the controller that affect the performance and stability of the SMC as described previously are α_1, α_2, ρ , and δ . In this section, we explain how to select appropriate parameter values to ensure stable operation of and convergence to the sliding surface.

Assuming that states x_1 and x_2 reach onto the sliding surface s , each state moves following the dynamic characteristic

$$\dot{s} = \alpha_1 \dot{x}_1 + \alpha_2 x_1 = 0 \quad (3.40)$$

To verify the characteristics of α_1 and α_2 , we solve the above 1st order differential equation as follows:

$$x_1(t) = x_1(0) \exp\left(-\frac{\alpha_2}{\alpha_1}t\right) \quad (3.41)$$

If we set $\frac{\alpha_2}{\alpha_1}$ in (3.41) as a positive value, then x_1 will be exponentially decreased toward the equilibrium point. Transient performance such as convergence speed and overshooting of SMC depends on these parameters.

The parameters ρ and δ are related to the stability margin and the chattering suppression of the controller, respectively. We assume that there is uncertainty in the passive elements to verify the characteristics of parameter ρ and δ . In general, passive components such as inductors have relatively large manufacturing tolerances, due to which actual inductance L_m in control input (3.25) is not exactly known but estimated as \hat{L}_m , which is provided on a data sheet by the manufacturers. If the difference between L_m and \hat{L}_m is increased, this causes reduced performance and stability of the system. To consider this uncertainty on the proposed control, we assume that the uncertainty of the magnetization inductance is bounded as follows:

$$|\hat{L}_m - L_m| \leq \Delta L \quad (3.42)$$

where \hat{L}_m and ΔL are estimated magnetization inductance and maximum manufacturing tolerance, respectively. Subsequently, the control input in (3.25) can be rewritten using estimated inductance \hat{L}_m as

$$d_{temp} = \frac{1}{v_b} \sqrt{-\frac{2\alpha_2 \hat{L}_m C_{out} x_1 v_{out}}{\alpha_1 T_s} + \frac{2\hat{L}_m P_{out}}{T_s} - \rho sat\left(\frac{s}{\delta}\right) - \frac{v_{in}}{v_b} d_{sw1}} \quad (3.43)$$

By substituting (3.43) into (3.22) and using (3.42), the $\dot{V}(s)$ and its upper limit can be

calculated as

$$\begin{aligned}
 \dot{V}(s) &= s\dot{s} \\
 &= s \frac{1}{L_m} \left((\hat{L} - L_m) \left(\frac{\alpha_1 i_{out}}{C_{out}} - \alpha_2 x_1 \right) - \frac{\alpha_1 T_s}{2C_{out}v_{out}} \rho \text{sat} \left(\frac{s}{\delta} \right) \right) \\
 &\leq \frac{1}{L_m} \left(\Delta L \left| \frac{\alpha_1 i_{out}}{C_{out}} - \alpha_2 x_1 \right| |s| - \frac{\alpha_1 T_s}{2C_{out}v_{out}} \rho |s| \right)
 \end{aligned} \tag{3.44}$$

so that by letting

$$\rho = \frac{2C_{out}v_{out}}{\alpha_1 T_s} \left(\Delta L \left| \frac{\alpha_1 i_{out}}{C_{out}} - \alpha_2 x_1 \right| + \eta \right) \tag{3.45}$$

where η is a strictly positive constant. After that from (3.44), we obtain

$$\dot{V}(s) = s\dot{s} \leq -\frac{\eta}{L_m} |s| \tag{3.46}$$

According to (3.46), the proposed controller can ensure the stable operation and convergence to the sliding surface in finite time even if disturbances and parameter uncertainties, such as output load variation and manufacturing tolerance of the coupled-inductor, exist in the APD circuit. In (3.45), if we set i_{out} and x_1 as the maximum values allowed by the circuit, a fixed value of ρ that can guarantee stability in the entire operating range can be obtained.

Parameter δ is the thickness of the boundary layer of the sliding surface. Chattering reduction by the saturation function in the proposed control system is possible only if the value of δ is sufficiently large. However, this would reduce the system performance, which reveals a trade-off between the possibility of chattering reduction and system performance.[26]

3.5 Simulation studies and experimental results

3.5.1 System configuration

To check the feasibility and overall operations of the proposed control scheme, simulation studies were conducted under the following conditions. In this simulation, MATLAB/SIMULINK was used as a testing environment and the parameters used are described in Table 3.1. Reference values of the output voltage and the control frequency of the buffer voltage and sliding mode control were 150 V and 20 kHz, respectively.

The experimental test bed was a 100 W converter with design specifications provided in Table 3.2. A Panasonic micro-controller MN103SFK1K with externally attached voltage and current sensors was used for the implementation of the control algorithm. Fig. 3.10

Chapter 3. Independent decoupling plus Inductor multiplexing method 32

Table 3.1: Simulation parameters

Parameter	Value	Parameter	Value
Grid voltage[Vrms]	100	Grid frequency[Hz]	50
EMI filter cut-off frequency[kHz]	3.5	Magnetization inductance[μ H]	320
Buffer capacitor[μ F]	45	Output capacitor[μ F]	45
Switching frequency[kHz]	20	Design parameter α_1, α_2	1, 0.01
Design parameter ρ, δ	2500, 8	Window size of moving average filter	40
Proportional-Integral gain(K_p, K_i)	2, 0.01		

Table 3.2: Hardware specification

Part Name	Specification
Diode(D_1, D_2, D_3, D_4)	ER504(400 V, 5 A)
MOSFET(Q_1, Q_2, Q_3)	TK31N60X(600 V, 30 A)
Diode(D_5, D_6, D_7)	SCS106AGC
Film Capacitor(C_{out}, C_b)	PCPW245MKP(45 uF, 450 V, 14.4 Arms)
Coupled-inductor	320 uH, 26 turn, Ferrite, Litz wire, 1 Arms, 7 Apeak
Cut-off frequency of the input filter	3.6 kHz

shows a photograph of the main circuit. All external sensors and a micro-controller were mounted on the same printed circuit board. In order to eliminate noise, these sensors were connected close to the micro-controller. To design the coupled-inductor, we have stacked wires in a sandwich structure on the center tab on ferrite EE-core and used Litz wire to minimize AC resistance. Experimental testing was performed using the setup shown in Fig. 3.11. In addition, an LC input filter was used to reduce the harmonic current due to DCM. When we were verifying the overall operation and performance, an MSO4034(oscilloscope, Tektronics) and a TW1800(Power analyzer, Yokogawa) were used as measuring instruments.

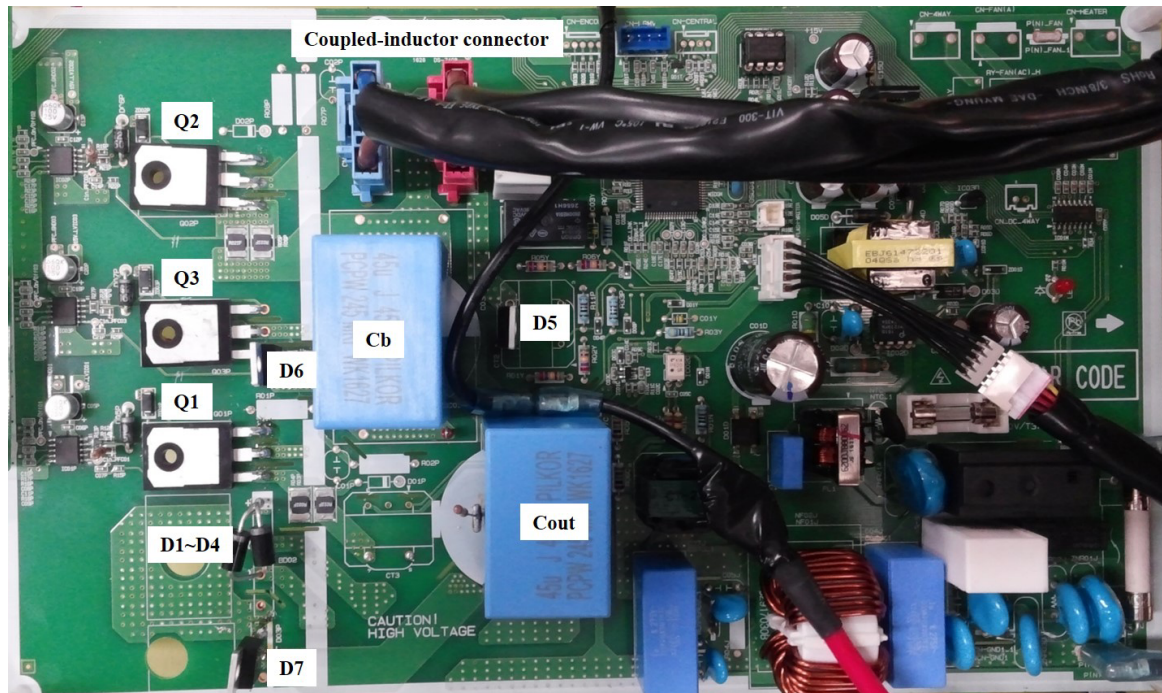


Figure 3.10: Hardware prototype

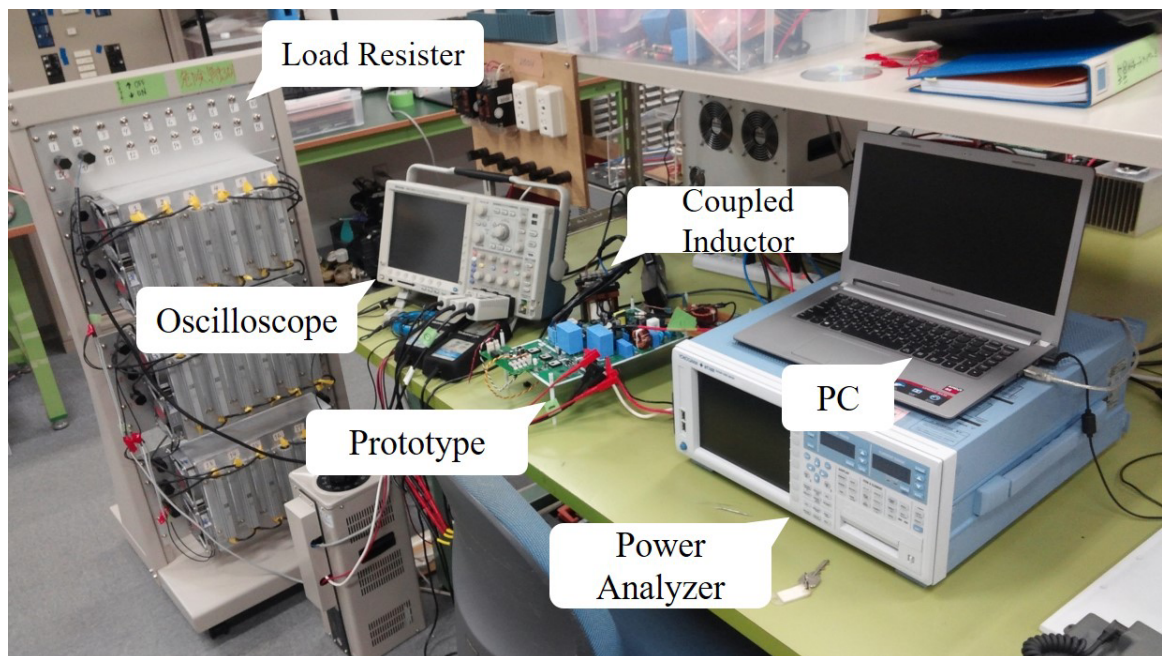


Figure 3.11: Laboratory test bed

3.5.2 Allowable voltage and ripple current of the buffer capacitor

Due to the buffer capacitor is an essential part of the APD circuit to remove ripple power, it should be selected considering the rated voltage and the allowable ripple current. In the proposed circuit, the maximum voltage applied to the buffer capacitor is equal to v_{out} . Therefore, the output voltage required by the application should be considered. Also, since the required ripple current is large due to the characteristics of the APD circuit, the allowable value is determined using the following equation.

$$\begin{aligned} P_{b_r} &= -\frac{V_m I_m}{2} \cos 2\omega t = -P_{out} \cos 2\omega t \\ P_{b_rms} &= \frac{P_{out}}{\sqrt{2}} \\ I_{b_rms} &= \frac{P_{out}}{\sqrt{2} V_{b_rms}} \end{aligned} \quad (3.47)$$

In equation (3.47), if P_{out} is the maximum power consumption, the required ripple current rating (I_{b_rms}) of the buffer capacitor can be obtained. Considering the lifetime and the allowable ripple current, the film capacitor is suitable as the buffer capacitor.

3.5.3 Simulation and experimental results

Fig. 3.12 is the simulation results of the proposed circuit. The simulation results show voltage waveform and state trajectories when the converter was operated with an output power of 100 W. Before the decoupling operation, the ripple voltage appeared in the output voltage, but after the operation, the former was absorbed by the buffer capacitor. As a result, the buffer voltage was pulsed. The red line indicates the sliding surface, which was derived in (3.9). Under the decoupling function operation, initial states went directly onto the sliding surface. After that, the errors were exponentially decreased when moving toward the equilibrium point.

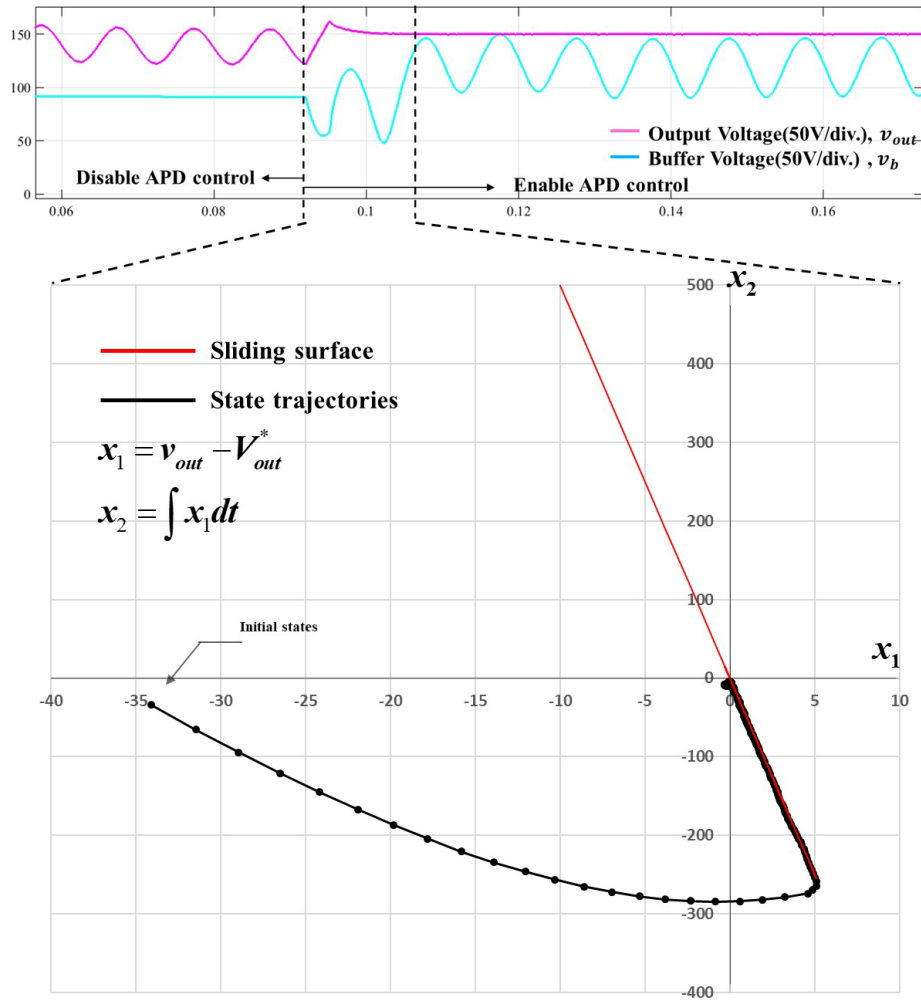


Figure 3.12: Simulation waveforms and the sliding motion of states

Fig. 3.13 shows the experimental operational results of the proposed converter under an output power of 100 W. Based on these, a sinusoidal waveform without harmonic distortion was obtained as the input current and ripple power on the output terminal was successfully removed. Ripple voltage was under 5 V and the buffer voltage was maintained below the

Chapter 3. Independent decoupling plus Inductor multiplexing method 36

output voltage. As a result, voltage stress on the decoupling circuit was lower than the conventional inductor-multiplexing method.[?]

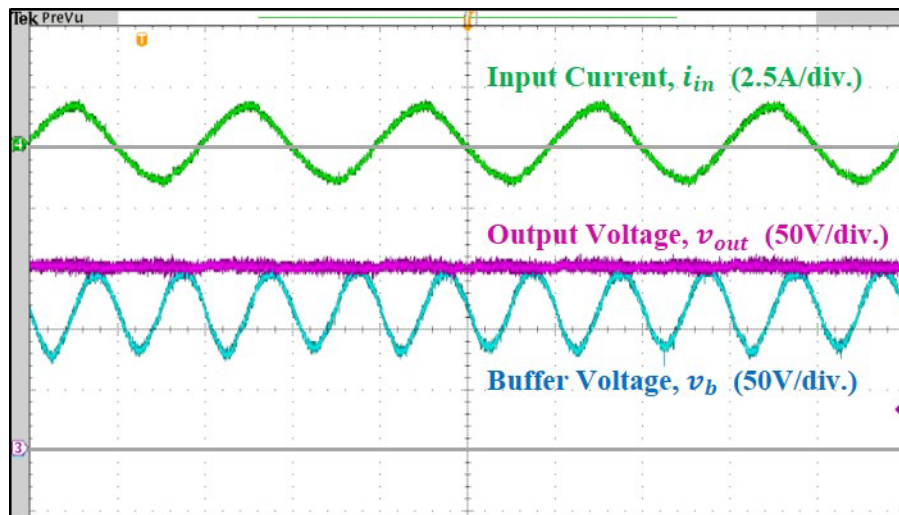


Figure 3.13: Experimental waveform produced by the proposed control mechanism

Fig. 3.14 shows the coupled-inductor current waveform during APD control. As shown in the figure, when the input current(i_s) is low, the current is compensated through the discharge of the buffer capacitor to produce a constant diode current(i_d).

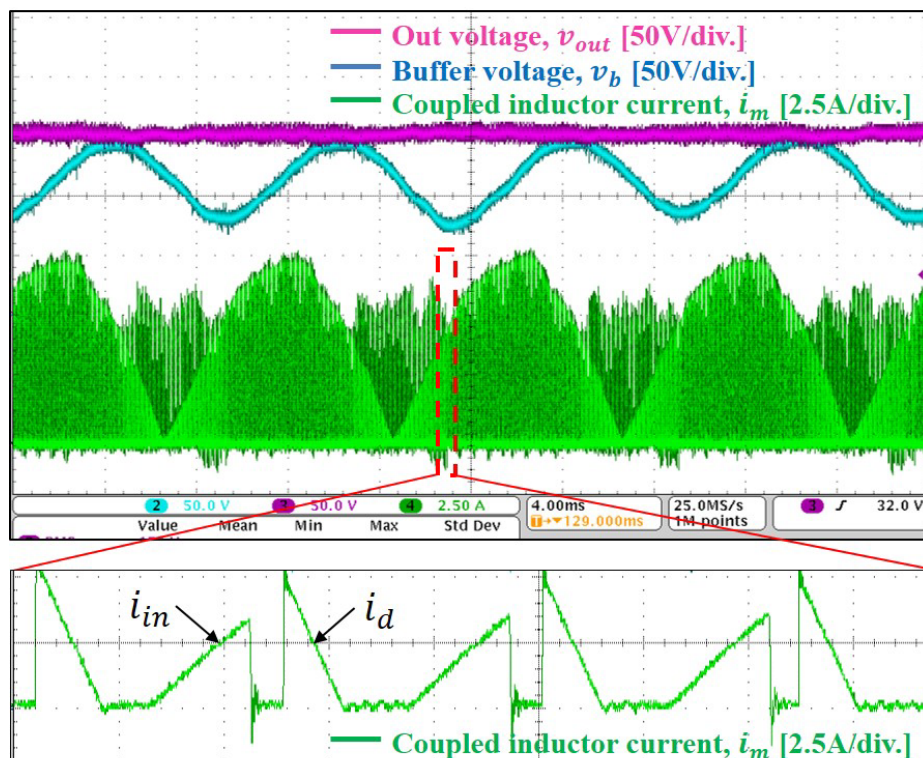


Figure 3.14: Experimental waveform of the coupled-inductor current

Fig. 3.15 and Fig. 3.16 show the experimental waveforms of the prototype in a transient state operation when the load was varied from 50 % to 75 %. From the test results, we can see that when the output load disturbance exists, the output voltage and input current were stable without distortion or overshoot. Therefore, the proposed sliding mode control was shown to be robust for transient state operation.

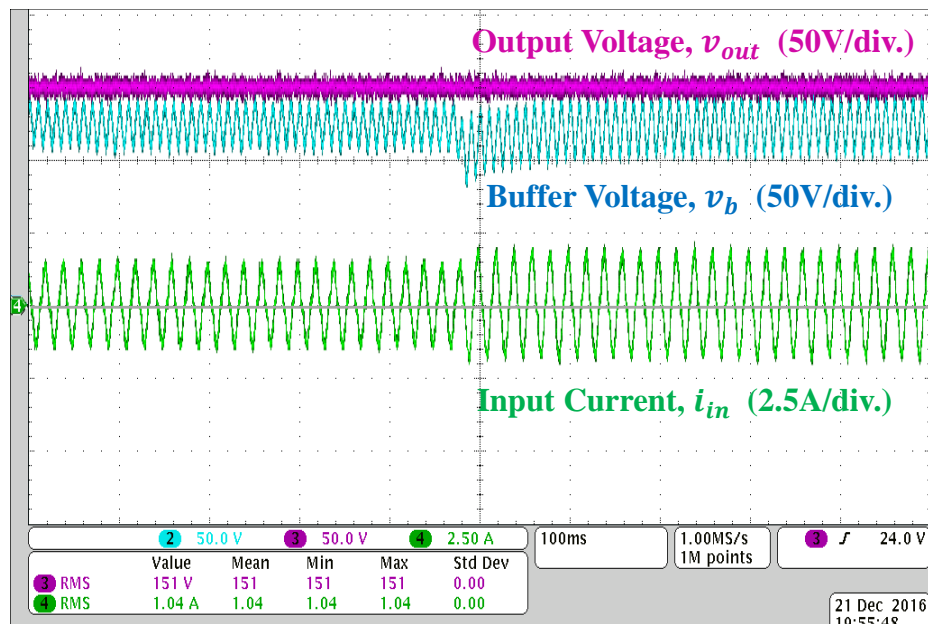


Figure 3.15: Experimental waveform in the transient response during 50 % to 75 % load steps

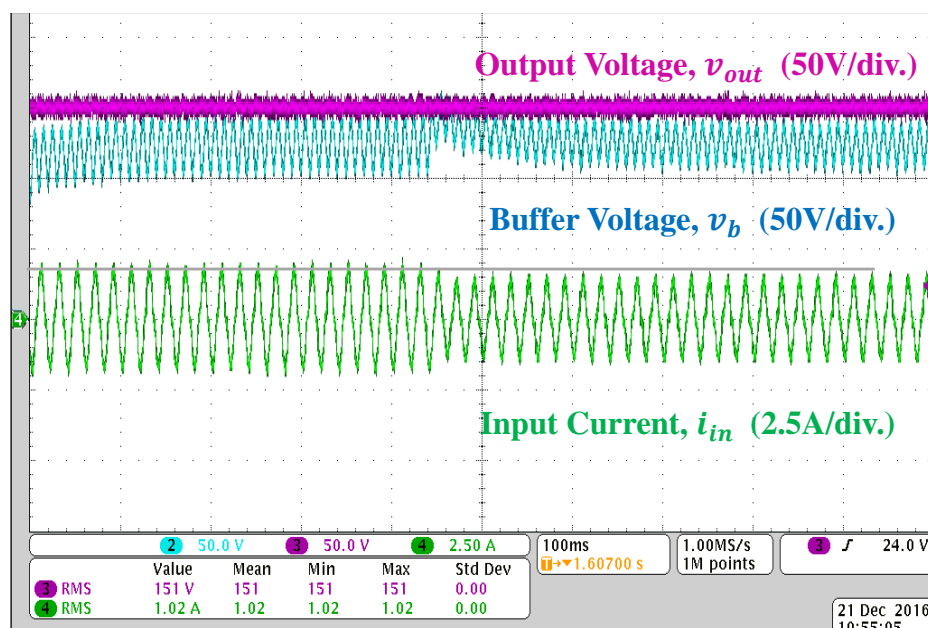


Figure 3.16: Experimental waveform in the transient response during 75 % to 50 % load steps

Fig. 3.17 shows the simulation result of the transient response when a 10% inductance error exists in the coupled-inductor. The error is immediately compensated by the proposed APD control, and distortion of the output voltage does not occur. Since the buffer energy is used for error compensation, the buffer voltage fluctuates.

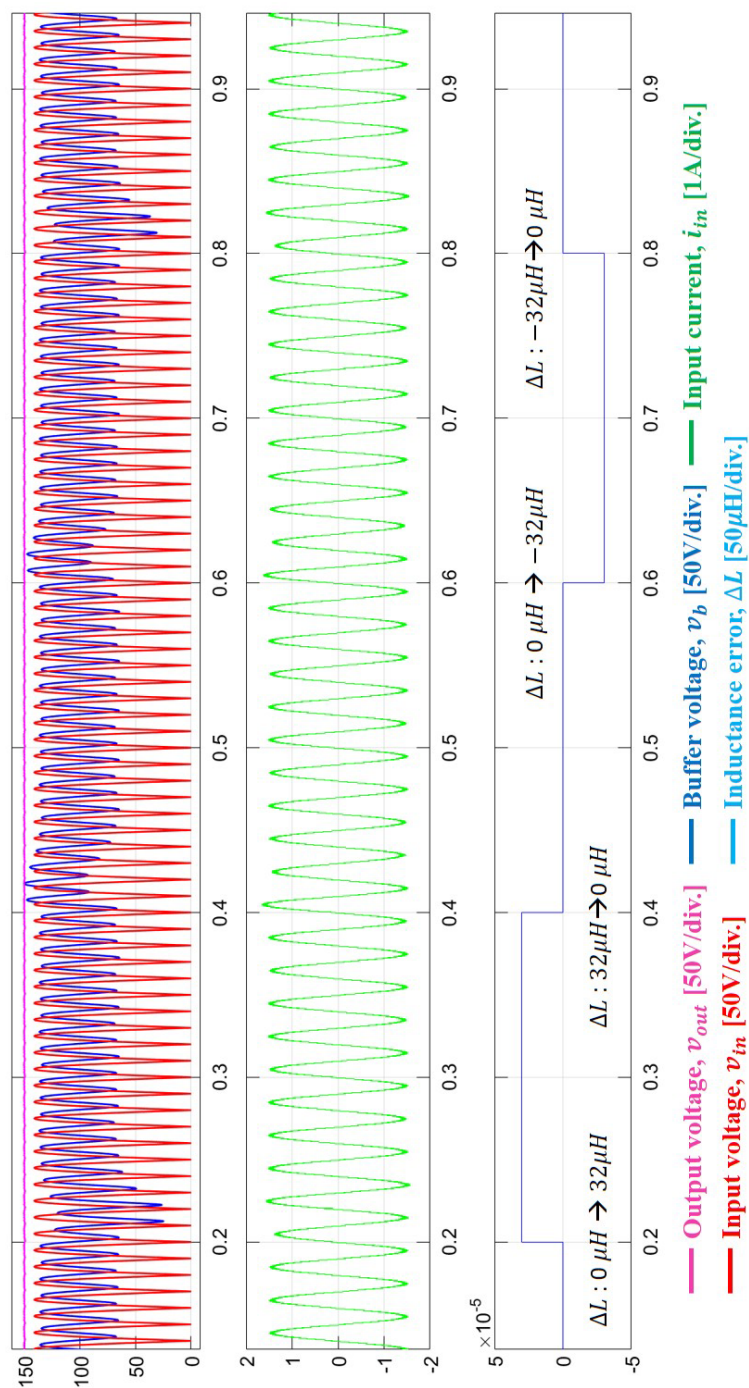


Figure 3.17: Simulation results of the transient response under the inductance change

Fig. 3.18 shows the efficiency and power factor under each load condition. From measurement results, we can see that the minimum power factor was over 98 % and the maximum

efficiency was 90.3 %.

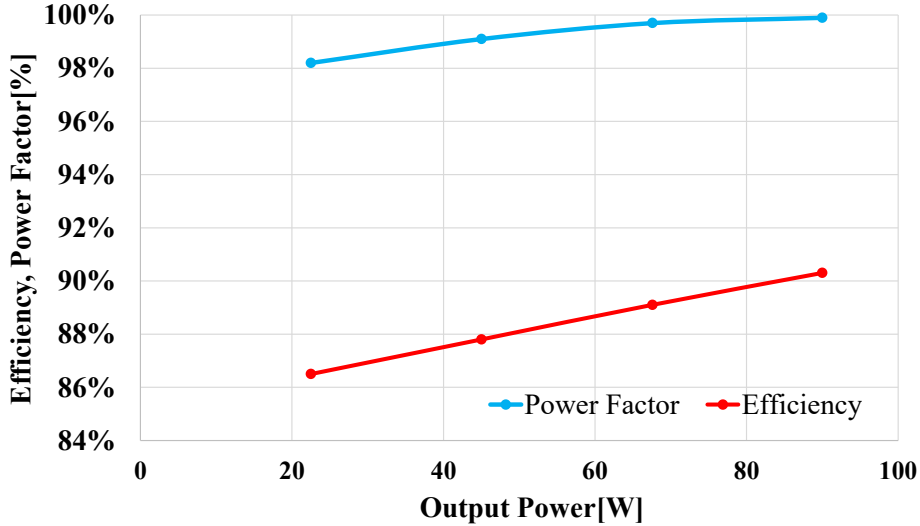


Figure 3.18: Power factor and efficiency of the proposed converter

3.6 Conclusion

Despite the benefit of a long lifespan, the conventional decoupling topology applied to buck-boost converters has relatively high manufacturing costs, high voltage stress, and large parametric uncertainties due to manufacturing tolerances and the non-linearity of passive components. To solve these problems, we propose a new circuit that operates at low buffer voltage and does not require additional inductors. The proposed sliding mode control method ensures a constant output, even if there are parametric uncertainties and disturbances. The proposed solution was experimentally verified by means of a 100 W laboratory system, the results from which indicate well-regulated output voltage. The output voltage ripple was under 5 V and the input current THD was 4.24 %. In addition, we obtained an output power factor of over 98 % and a maximum efficiency of 90.3 %.

Table 3.3 compares the conventional switch and input multiplying method with the proposed method. Although the proposed method is less efficient than the conventional method, it has an advantage in terms of volume, voltage stress, power factor, and THD.

Chapter 3. Independent decoupling plus Inductor multiplexing method 40

	Conventional method	Proposed method
Rated voltage of C_b	450 V ($v_{in_max} + v_{out} + \Delta v_b < v_{b_max}$)	200 V ($v_{b_max} < v_{out}$)
Volume of C_b	35.0 mm X 50.0 mm X 57.5 mm	20.0 mm X 39.5 mm X 41.5 mm (-67.4%)
Volume of IGBT	.	19.7 mm X 15.7 mm X 5.3 mm
Volume of diode	.	6.2 mm X 6.7 mm X 2.4 mm X 2
Total volume	100.6 cm^3	34.4 cm^3 (-65.5%)
Power Factor, THD	99.2%, 8.4%	99.9%(+0.7%), 4.2%(-4.2%)
Efficiency	92.8%	90.3%(-2.5%)

Table 3.3: Comparison between conventional method and proposed method

CHAPTER 4

Lyapunov function based control strategy

Conventional control methods of the APD circuit are mainly divided into the open-loop control method and the closed-loop method. The open-loop method can be easily implemented in many applications, but it is sensitive to the parameter variations. Repetitive control, multi-resonant control, Proportional integral plus resonant control method is a typical closed-loop control method of APD circuit. Closed-loop methods have good performance even under the various disturbance conditions, but conventional closed-loop control methods do not guarantee the global stability due to highly non-linearities and complex structure of the dependent APD circuit.

As shown in Fig. 4.1, the value and characteristics of inductance and capacitance change depending on temperature, current, and materials. If the tolerances are considered, the parameter uncertainty is increased. In the case of a converter with APD circuit, the number of passive components increases, so it is necessary to design the controller considering the uncertainty of the model.

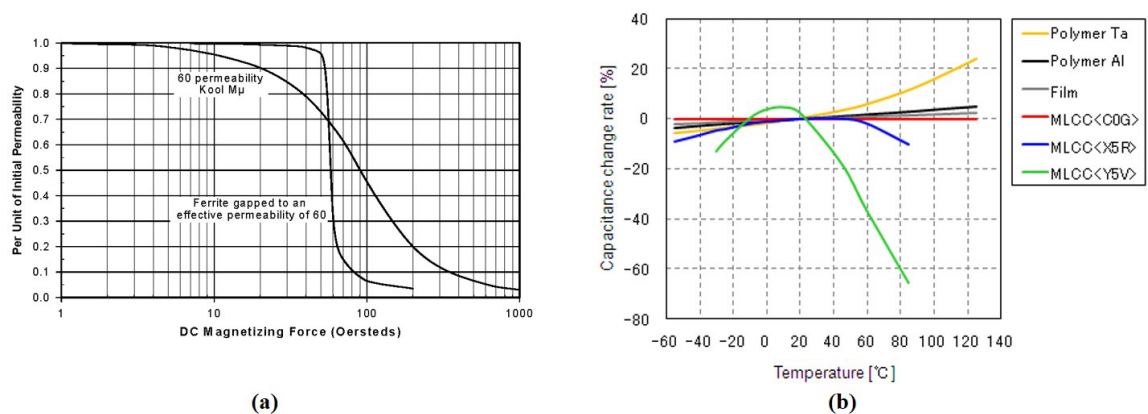


Figure 4.1: Nonlinear characteristics of passive devices (a) Inductor, (b) Capacitor

4.1 Contribution Summary

We apply Lyapunov-function based control approach to control of the APD circuit which was introduced in Chapter 3. This control scheme guarantees the global stability of the entire control system, even if model uncertainties, such as parameter variation, exist. In addition, the number of design parameters is greatly reduced, and parameter selection criteria based on control theory are also presented. Through MATLAB simulation and prototype experiments, we verified the global stability and effectiveness of the proposed control scheme.

4.2 Modeling of the buck-boost converter with the APD circuit

In the APD circuit, the v_b represents a compensable amount of P_{in_r} and generally controls the average value over the period of the twice input frequency. At steady-state conditions and neglecting circuit loss, the power of each stage can be derived as follows,

$$P_{in_avg} + P_{in_r} = P_{out} + P_{b_avg} + P_{b_r} \quad (4.1)$$

where P_{b_avg} and P_{b_r} are average and ripple power values of the buffer capacitor, respectively. Assuming that P_{in_r} is removed by the decoupling circuit, we can eliminate P_{in_r} and P_{b_r} in (4.1) to give

$$P_{in_avg} = P_{out} + P_{b_avg} = P_{out} + v_{b_avg} C_b \dot{v}_{b_avg} \quad (4.2)$$

where v_{b_avg} is an average value of v_b during period of the twice input frequency. Then, we can obtain \dot{v}_{b_avg} as follows

$$\dot{v}_{b_avg} = \frac{P_{in_avg} - P_{out}}{C_b v_{b_avg}} = \frac{V_m I_m}{2C_b v_{b_avg}} - \frac{v_{out}^2}{C_b v_{b_avg} R} \quad (4.3)$$

Magnitude of the average input current (I_m) can be calculated as

$$\begin{aligned} i_{in_peak} &= \frac{v_{in}}{L_m} d_{sw1} T_s = \frac{V_m d_{sw1} T_s}{L_m} \sin \omega t \\ \bar{i}_{in} &= \frac{i_{in_peak}}{2} d_{sw1} = \frac{V_m d_{sw1}^2 T_s}{2L_m} \sin \omega t \\ I_m &= \frac{V_m d_{sw1}^2 T_s}{2L_m} \end{aligned} \quad (4.4)$$

Substituting (4.4) into (4.3), we can obtain the differential equation of v_{b_avg} as follows

$$\dot{v}_{b_avg} = \frac{V_m^2 d_{sw1}^2 T_s}{4C_b L_m v_{b_avg}} - \frac{v_{out}^2}{C_b v_{b_avg} R} \quad (4.5)$$

4.3 Lyapunov-function based control strategy

The object of the proposed control scheme is to regulate v_{b_avg} and v_{out} . The errors for these states can be defined as:

$$e_1 = v_{out} - v_{out}^*, \quad e_2 = v_{b_avg} - v_{b_avg}^* \quad (4.6)$$

where $v_{b_avg}^*$ and v_{out}^* are constant reference values of v_{b_avg} and v_{out} . Using (4.6) and average state space equations obtained previous section, the error dynamics of the buck-boost converter with the dependent APD circuit can be calculated as follows.

$$\begin{aligned} \dot{e}_1 = \dot{v}_{out} &= \frac{1}{C_{out}} \left(\frac{T_s}{2L_m v_{out}} (v_s d_{sw1} + v_b d_{temp})^2 - \frac{v_{out}}{R} \right) \\ \dot{e}_2 = \dot{v}_{b_avg} &= \frac{V_m^2 d_{sw1}^2 T_s}{4C_b L_m v_{b_avg}} - \frac{v_{out}^2}{C_b v_{b_avg} R} \end{aligned} \quad (4.7)$$

According to Lyapunov's direct method, the equilibrium point is globally asymptotically stable if $V(e)$ satisfies following properties.

1. $V(0) = 0$
2. $V(e) > 0, \forall e \neq 0$
3. $V(e) \rightarrow \infty$ as $\|e\| \rightarrow \infty$
4. $\dot{V}(e) < 0, \forall e \neq 0$

To obtain nonlinear control inputs which make the globally asymptotic stable, following Lyapunov candidate is used.

$$V(e_1, e_2) = \frac{1}{2} C_{out} e_1^2 + \frac{1}{2} C_b e_2^2 \quad (4.8)$$

This function satisfies three properties(1 ~ 3) of Lyapunov's direct method. The aim is to make the derivative of V negative definite. Thus, \dot{V} is obtained from (4.8) which yields to

$$\dot{V}(e_1, e_2) = C_{out} e_1 \dot{e}_1 + C_b e_2 \dot{e}_2 \quad (4.9)$$

Let \dot{e}_1 and \dot{e}_2 be defined as follows.

$$\dot{e}_1 = -k_1 e_1, \quad \dot{e}_2 = -k_2 e_2 \quad (4.10)$$

where k_1 and k_2 are strictly positive design values. Then, \dot{V} is negative definite as follows.

$$\dot{V}(e_1, e_2) = -k_1 e_1^2 - k_2 e_2^2 < 0, \quad \forall (e_1, e_2) \neq (0, 0) \quad (4.11)$$

Substituting (4.7) into (4.10), control inputs can be obtained as follows.

$$\begin{aligned} d_{temp} &= \frac{1}{v_b} \sqrt{\frac{2L_m v_{out}^2}{T_s R} - \frac{2L_m C_{out} v_{out} k_1 e_1}{T_s}} - \frac{v_{in}}{v_b} d_{sw1} \\ d_{sw1} &= \frac{1}{V_m} \sqrt{\frac{4L_m v_{out}^2}{T_s R} - \frac{4L_m C_b k_2 v_{b_avg} e_2}{T_s}} \end{aligned} \quad (4.12)$$

Fig.4.2 represents the proposed control systems. The final duty ratios of Q_2 and Q_3 are decided by a table in Fig. 4.2. To obtain the average voltage of buffer capacitor, moving average filter is used.

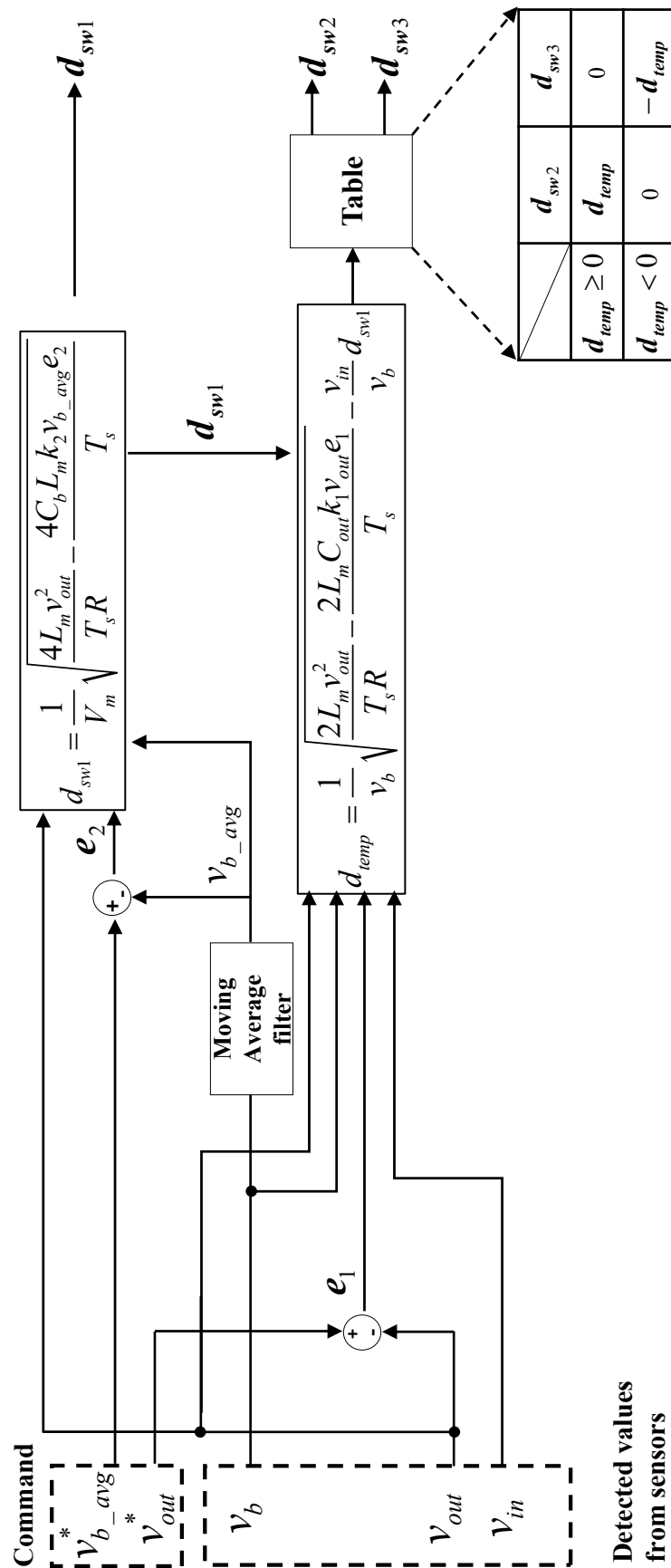


Figure 4.2: Proposed control system

4.3.1 Robustness of the proposed control system to converter parameter's variations

Suppose that the measured load resistance \hat{R} is different from the actual resistance value R , then the control input d_{temp} and d_{sw1} are expressed as

$$\begin{aligned} d_{temp} &= \frac{1}{v_b} \sqrt{\frac{2L_m v_{out}^2}{T_s \hat{R}} - \frac{2L_m C_{out} v_{out} k_1 e_1}{T_s}} - \frac{v_{in}}{v_b} d_{sw1} \\ d_{sw1} &= \frac{1}{V_m} \sqrt{\frac{4L_m v_{out}^2}{T_s \hat{R}} - \frac{4L_m C_b k_2 v_{b_avg} e_2}{T_s}} \end{aligned} \quad (4.13)$$

Substituting (4.13) into (4.9) yields

$$\dot{V}(e_1, e_2) = \left(v_{out} \left(\frac{R - \hat{R}}{R\hat{R}} \right) e_1 - C_{out} \frac{k_1 e_1^2}{v_{out}} \right) + \left(v_{out}^2 \left(\frac{R - \hat{R}}{R\hat{R}} \right) e_2 - C_b k_2 e_2^2 \right) \quad (4.14)$$

Assuming that an error of the load resistance is bounded as $|R - \hat{R}| < \Delta R$, then the upper boundary of (4.14) can be obtain as follows:

$$\dot{V}(e_1, e_2) \leq \left(\frac{v_{out} |e_1|}{R\hat{R}} \Delta R - C_{out} \frac{k_1 e_1^2}{v_{out}} \right) + \left(\frac{v_{out}^2 |e_2|}{R\hat{R}} \Delta R - C_b k_2 e_2^2 \right) \leq -\eta \quad (4.15)$$

where η is a strictly positive constant. If k_1 and k_2 are properly selected to satisfy the above conditions, the system becomes globally stable even in the presence of uncertainty in the load resistance. In the same manner, we can determine k_1 and k_2 that can guarantee global stability against changes in C_b , C_{out} , and L_m .

4.4 Simulation studies and experimental results

To verify performances of the proposed control method, simulation studies and experiments were conducted using parameters and specifications in Table 3.1. MATLAB/SIMULINK was used as a simulation environment, and Panasonic micro-controller MN103SFK1K with externally attached voltage sensors was used for the testing of the control algorithm. Reference values of the output voltage and buffer voltage were 150 V and 120V, respectively.

Fig. 4.3 shows the simulation results when the converter was operated with an output power of 90 W. Before the decoupling operation, the ripple power appeared in the output voltage, but after the operation, the ripple power was eliminated by the APD circuit. Also, it can be confirmed that the unity power factor is achieved after reaching the steady state. $\dot{V}(e_1, e_2)$ is always negative, which shows that the control system is globally asymptotically stable.

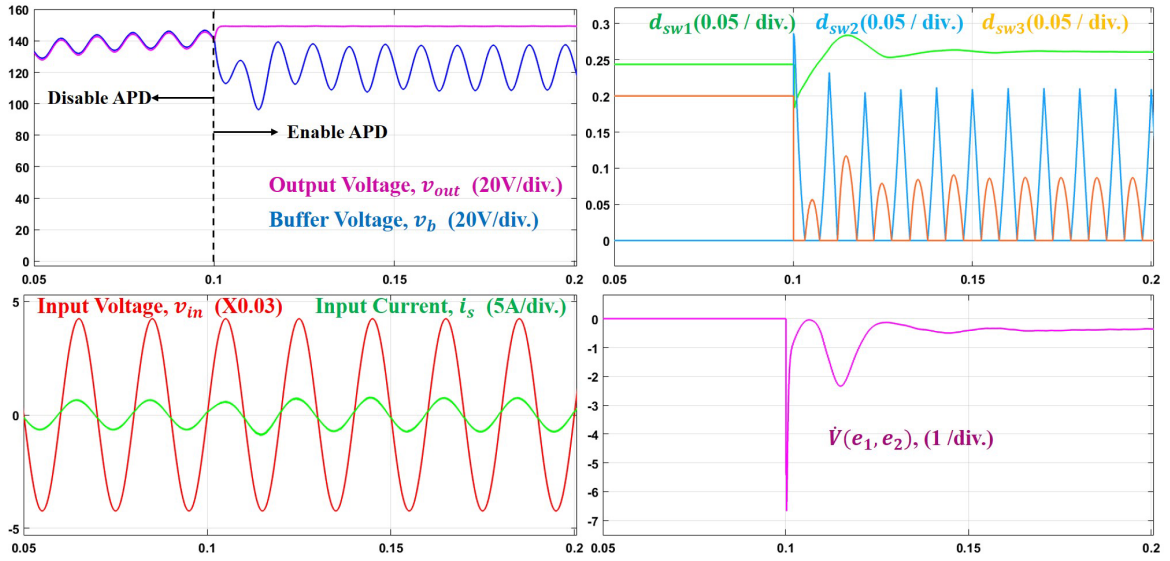


Figure 4.3: Simulation results of the prototype

Fig. 4.4 is the experimental results when the output power is 100W. Fig. 4.4(a), the ripple power is compensated by the APD circuit to produce a constant output voltage. At this time, the ripple of the output voltage is 8V or less. Fig. 4.4(b) shows the current waveform of the coupled-inductor. The current of the Q_7 is always controlled constantly regardless of the input voltage.

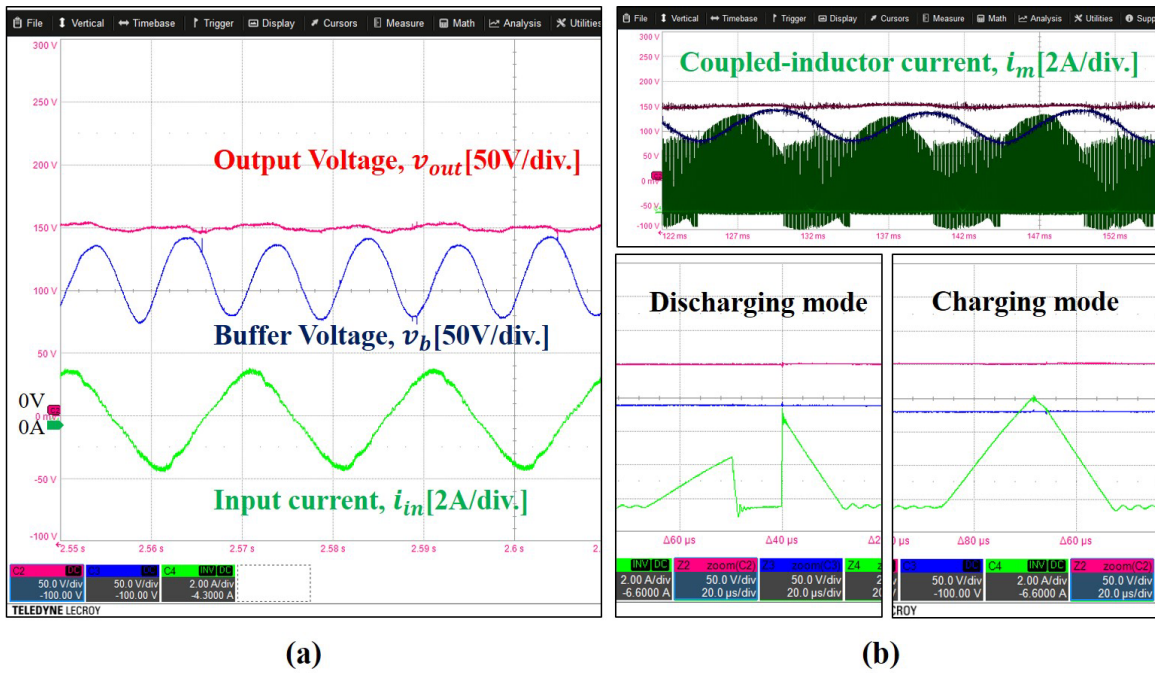


Figure 4.4: Experimental waveforms (a) steady state and (b) current of the coupled-inductor

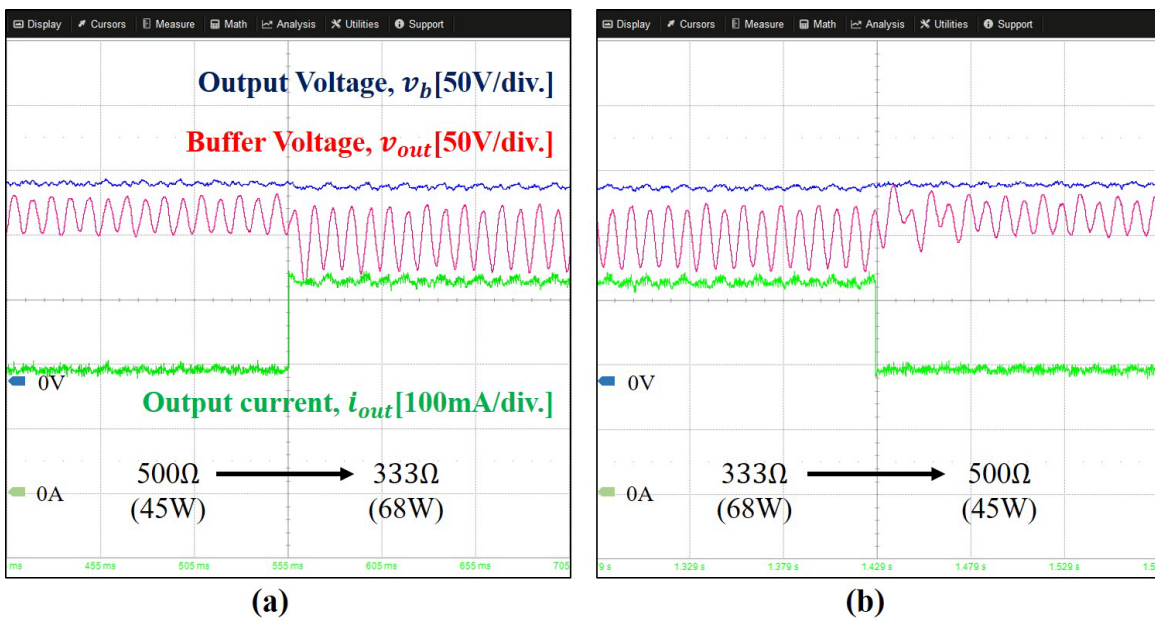


Figure 4.5: Transient response during (a) 500 Ω to 333 Ω and (b) 333 Ω to 500 Ω resistance change

Fig. 4.5 shows experimental result when the output resistor was varied from 500 Ω to 333 Ω and 333 Ω to 500 Ω . From the test results, we can see that when the output resistor is changed, the output voltage was stable without distortion or overshoot. Therefore, the proposed control scheme was shown to be robust for parameter variation.

4.5 Conclusion

In the conventional APD control method, it is difficult to guarantee the global stability when the model has nonlinearities and uncertainties. In this paper, we propose a nonlinear feedback control system based on the Lyapunov's direct method. With this control scheme, global stability can be guaranteed even in the presence of uncertainties in parameters. In addition, there are only two parameters required for the design, and it is possible to provide a theory-based design criterion for parameter selection. Through the MATLAB / SIMULINK simulation and the prototype experiment, we could verify the APD operation and the global stability of the proposed control system.

CHAPTER 5

Modular design and interleaving structure of APD circuit based converter

5.1 Contribution Summary

The interleaving technique is a strategy that increases the effective pulse frequency through phase shift and synchronization of several switching cells. This effectively reduces the size of the input and output filters and improves efficiency and conducted electromagnetic emission. It can also be a suitable solution for high power applications because it can effectively reduce current stress.[38] So far, several interleaving techniques have been applied to various converter topologies such as boost, buck, and buck-boost converter. However, it is difficult to apply the interleaving technique to APD circuit which is being studied recently. The APD method is a technique that can replace electrolytic capacitors with small capacity film capacitors. This method can improve the short lifespan and low reliability of electrolytic capacitors. However, in order to use the small film capacitor, additional switches and inductors are required. This means that the volume and complexity of the entire circuit increases, making it difficult to apply interleaved techniques. In order to apply interleaving technique to the APD circuit, the following conditions must be satisfied.

- 1) The complexity of the basic switching cell should be low.
- 2) Robust controller design for non-linearities and model uncertainties is needed.

In this Chapter, we design a decoupling circuit module that solves the problem in 1) and proposed a multi-phase interleaved circuit using it. We also propose a robust controller for model uncertainties and nonlinearities of the proposed circuit by applying sliding mode control. The proposed circuit and control method are verified by MATLAB simulation.

5.2 APD circuit based AC/DC interleaved buck-boost converter

Fig.5.1 shows the structure of the proposed interleaved circuit and the basic module. The basic modules are connected in parallel, and the reverse blocking(RB) IGBTs of each module

are controlled by an interleaved gate signal. The basic module has a primary side and a secondary side, the secondary side including the decoupling circuit.

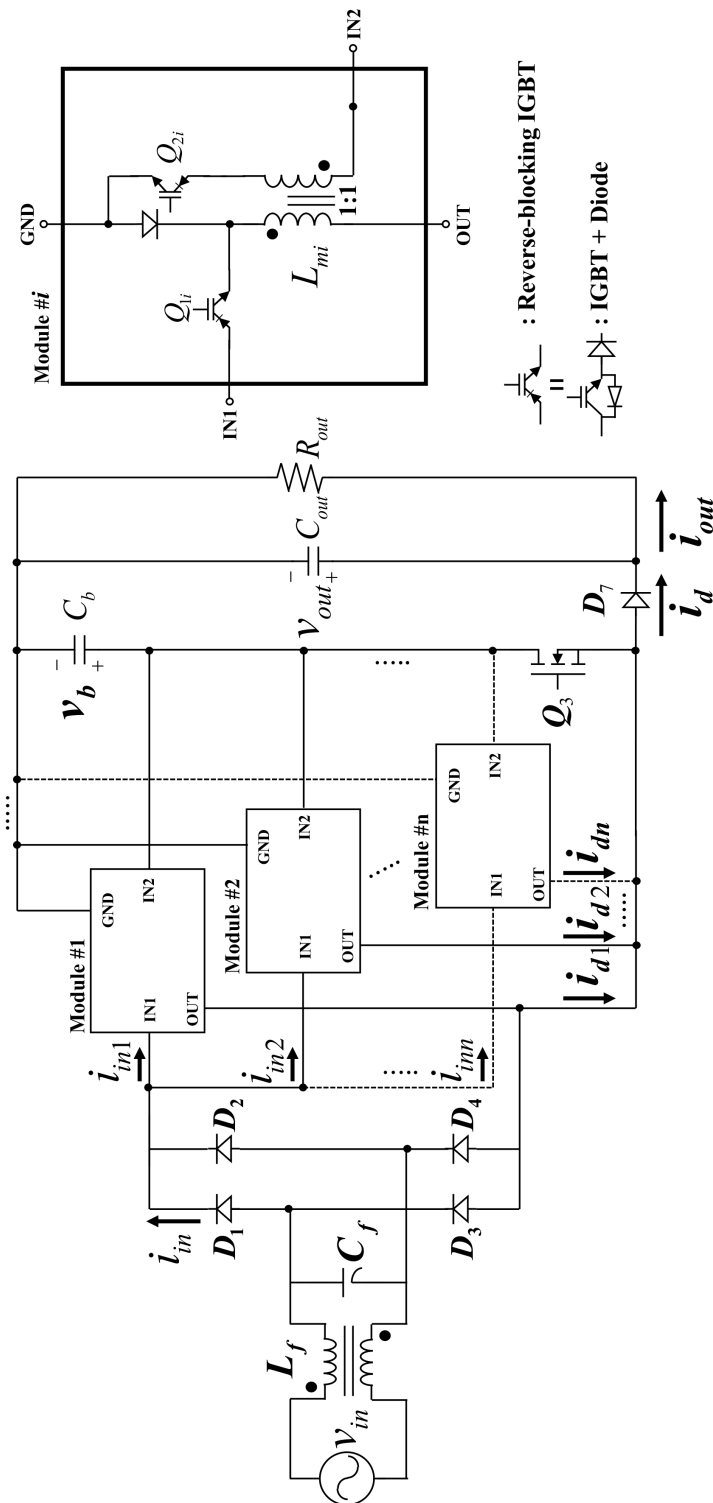


Figure 5.1: Proposed circuit (left) and basic module (right).

Fig.5.2 shows the overall operation of the proposed circuit and it operates as a buck-boot converter or decoupling circuit depending on the combination of the states of each switch.

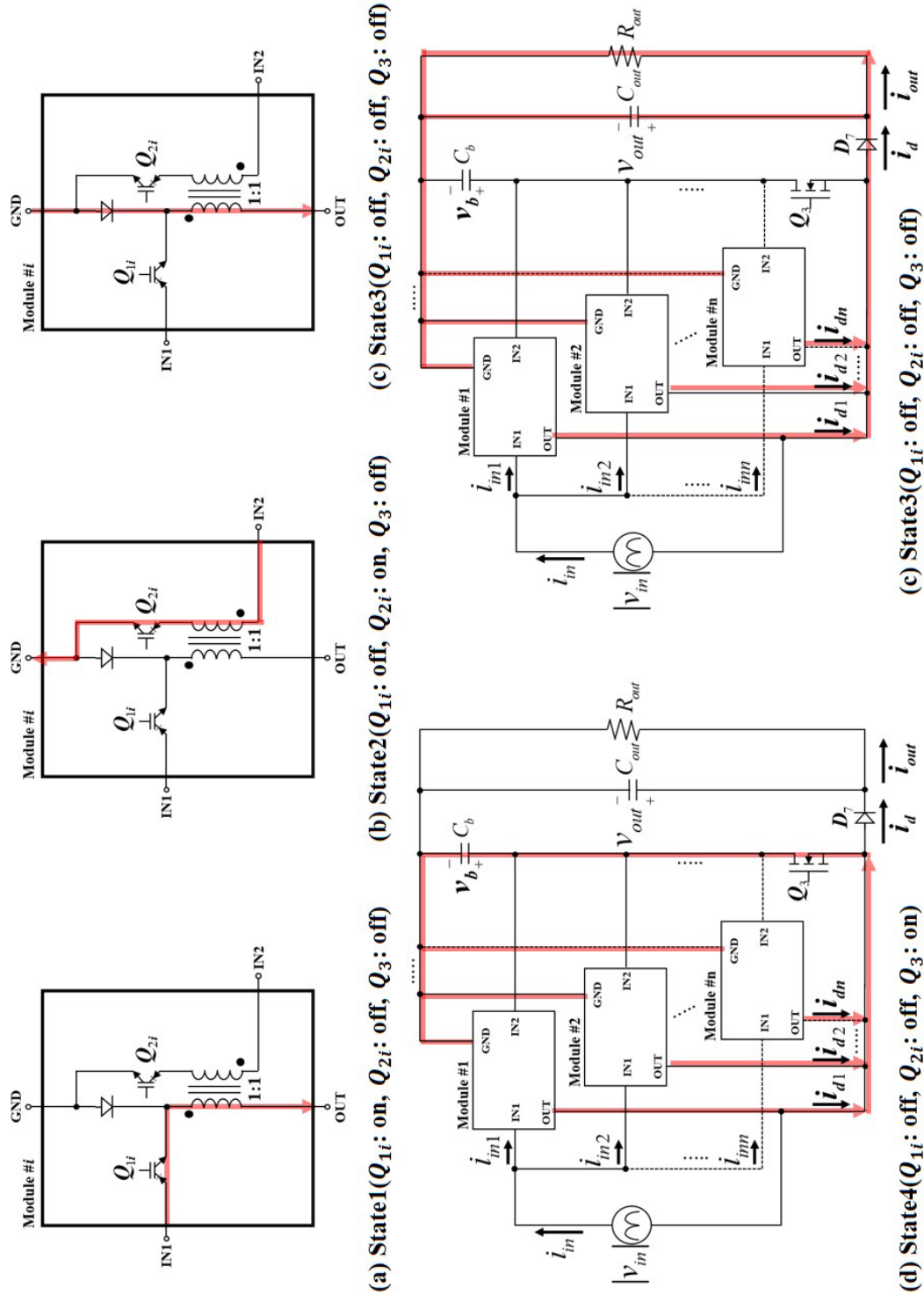


Figure 5.2: Overall operations of proposed active power decoupling (APD) circuit.(a) State1, (b) State2, (c) State3, (d) State4, (e) State5

- State1:** Switch1(Q_{1i}) is on and all other switches (Q_{2i}, Q_3) are off. The primary side of the coupled-inductor charges magnetic energy from the power system.

- State2:** Switch2(Q_{2i}) is on and all other switches (Q_{1i}, Q_3) are off. Each decoupling circuit works as a fly-back converter. Stored energy in the buffer capacitor is transferred to the secondary side of the coupled-inductor. In this state, insufficient energy is compensated.

- State3:** All switches (Q_{1i}, Q_{2i}, Q_3) are off, stored energy in each coupled-inductor is discharged to the output terminal through the diode(D_7).

- State4:** Switch3(Q_3) is on and all other switches (Q_{1i}, Q_{2i}) are off. redundant energy in the primary side of the coupled-inductor moves to the buffer capacitor.

5.3 Control System

The proposed control system consists two parts, which are buffer voltage and APD controller. To guarantee the stability and regulation performance of output voltage, we applied a sliding mode control algorithm for the APD controller.

5.3.1 Buffer voltage control

The object of buffer voltage control is to regulate the V_b and generate sinusoidal input current waveform for the unity power factor. V_b is the root mean square(RMS) value of v_b . At steady-state conditions and neglecting circuit loss, the power of each stage in the proposed converter can be derived as follows,

$$P_{in_avg} + P_{in_r} = P_{out} + P_{b_avg} + P_{b_r} \quad (5.1)$$

Assuming that AC power is removed by the decoupling circuit, we can eliminate P_{in_ac} and P_{b_r} in (5.1) to give

$$P_{in_avg} = \frac{V_{s_m} I_{s_m}}{2} = P_{out} + P_{b_avg} \quad (5.2)$$

If the proposed converter works in discontinuous current mode(DCM), peak input current of i th decoupling module($i_{s_peak_i}$) can be obtained as

$$i_{s_peak_i} = \frac{V_{s_m} \sin \omega t}{L_{mi}} T_s d_{sw1} \quad (5.3)$$

Then, sum of the average input currents(\bar{i}_{in}) of each module can be calculated as follows:

$$\begin{aligned} \bar{i}_{in} &= \sum_{i=1}^n \bar{i}_{si} = \sum_{i=1}^n \left(\frac{i_{s_peak_i}}{2} \right) d_{sw1} \\ &= \sum_{i=1}^n \frac{V_{s_m} d_{sw1}^2 T_s}{2L_{mi}} \sin \omega t = I_{s_m} \sin \omega t \end{aligned} \quad (5.4)$$

where n and L_{mi} are the total number of phases and the inductance of each coupled-inductor, respectively. Using (5.4), we can obtain magnitude of input current(I_{s_m}) as

$$I_{s_m} = \sum_{i=1}^n \frac{V_{s_m} d_{sw1}^2 T_s}{2L_{mi}} \quad (5.5)$$

Assuming that each inductance has a same inductance, (5.5) can be approximated as:

$$I_{s_m} = \frac{nV_{s_m}d_{sw1}^2T_s}{2L_m} \quad (5.6)$$

Using (5.2) and (5.6), we can calculate the duty ratio of Q1 as

$$d_{sw1} = \sqrt{\frac{4L_m(P_{out} + P_{b_avg})}{nV_{s_m}^2T_s}} \quad (5.7)$$

P_{b_avg} can be regarded as the control input for regulating V_b . In order to control V_b , we use a simple proportional-integral controller:

$$P_{b_avg} = K_p(V_b^* - V_b) + K_i \int (V_b^* - V_b)dt \quad (5.8)$$

where V_b^* is the target buffer voltage. The moving RMS is implemented in the control system to obtain V_b at time k as follows:

$$V_b(k) = \sqrt{\frac{1}{M} \sum_{j=0}^{M-1} v_b^2(k-j)}$$

where M is the number of points in the moving RMS. Assuming that P_{out} and P_{b_avg} are at steady state, then d_{sw1} is unchanged. Thus, the phase of \bar{i}_{in} is the same as for the input voltage, and due to this reason, the unity power factor and a sinusoidal wave form are achieved without harmonic distortion. The reference value of V_b can be calculated using that P_{b_r} and the energy of the buffer capacitor(W_b) counterparts when the power pulsation is compensated for by the decoupling circuit:

$$W_b = \int_{t_0}^t P_b dt = \frac{1}{2}C_b v_b^2(t) - \frac{1}{2}C_b v_b^2(t_0) \quad (5.9)$$

(5.9) can be rewritten using (2.3) as

$$\begin{aligned} W_b &= -\frac{P_{out}}{2\omega} (\sin 2\omega t - \sin 2\omega t_0) \\ &= \frac{1}{2}C_b v_b^2(t) - \frac{1}{2}C_b v_b^2(t_0) \end{aligned} \quad (5.10)$$

Assume that $\sin 2\omega t_0$ is 0, then $v_b(t_0)$ can be regarded as V_b . Subsequently, v_b can be derived using (5.10) as

$$v_b = \sqrt{V_b^2 - \frac{P_{out}}{\omega C_b} \sin 2\omega t} \quad (5.11)$$

Using (5.11), we can estimate the voltage range of v_b . It is better for v_b to exist in the vicinity of the output voltage to maximize the operational range. Assuming that $\sin 2\omega t$ is

-1, v_b reaches its maximum value v_{b_max} , then the reference buffer voltage V_b^* which can maximize the operational range can be derived as follows:

$$\begin{aligned} v_{b_max} &= V_{out}^* = \sqrt{(V_b^*)^2 + \frac{P_{out}}{\omega C_b}} \\ V_b^* &= \sqrt{(V_{out}^*)^2 - \frac{P_{out}}{\omega C_b}} \end{aligned} \quad (5.12)$$

5.3.2 Active power decoupling control

The main purpose of APD control is to remove AC power form the power system with the actively controlled switches. In order to make the operation robust, a sliding mode control(SMC) scheme is used, which is a useful nonlinear control method to take into account parametric uncertainties and disturbances. In addition, this method provides simple and robust solutions within a well-established theoretical framework. The closed-loop response is the fastest possible response since it provides control input signals that can be fed directly into the converters without any supplementary modulation operation.[?]

To make a output voltage constant and converge it to a reference value, we decided each state as follows

$$x_1 = v_{out} - V_{out}^*, \quad x_2 = \int x_1 dt \quad (5.13)$$

For easy implementation on a real system, we consider the sliding surface as a linear combination of the state variables, described in (5.13). Thus, we can specify the sliding surface as

$$s = \alpha_1 x_1 + \alpha_2 x_2 \quad (5.14)$$

Next, we define a candidate Lyapunov function as

$$V(s) = \frac{1}{2} s^2 \quad (5.15)$$

then to guarantee system stability and convergence of the state space trajectory to the sliding surface s , derivatives of the Lyapunov function (5.15) should satisfy the following inequality:

$$\dot{V}(s) = s\dot{s} < 0, \text{ if } s \neq 0 \quad (5.16)$$

Using the sliding surface (5.14), a time derivative of s can be calculated as

$$\begin{aligned}\dot{s} = \alpha_1 \dot{v}_{out} + \alpha_2 x_1 &= \alpha_1 \frac{\bar{i}_d - i_{out}}{C_{out}} + \alpha_2 x_1 \\ &= \sum_{i=1}^n \frac{\alpha_1 \bar{i}_{di}}{C_{out}} - \frac{\alpha_1 i_{out}}{C_{out}} + \alpha_2 x_1\end{aligned}\quad (5.17)$$

where \bar{i}_d and i_{out} are the average value of diode D_7 's current and load current, respectively. To calculate the equivalent input, we can obtain the following supplementary equation under condition $\dot{s}(x) = 0$:

$$\sum_{i=1}^n \bar{i}_{di} = -\frac{\alpha_2 C_{out} x_1}{\alpha_1} + i_{out}\quad (5.18)$$

Nevertheless, \bar{i}_{d_i} is not a directly controllable input, and as a result, the control input must be derived using the relationship between (5.18) and the duty ratios of each switch. In the proposed circuit, the diode current is decided by the magnetization current, and this current can be determined by combinations of switch and operation mode, the relationship for which is shown in Fig.3.6 and through which, the average value of the i th diode current can be derived as follows:

$$\bar{i}_{di} = \frac{1}{T_s} \int i_{di}(t) dt = \frac{d_{off} T_s}{2T_s} i_{d_peaki}\quad (5.19)$$

where \bar{i}_{di} , i_{di} and i_{d_peaki} are the average, instantaneous, and peak values of the i th diode current, respectively. Since the proposed circuit works in DCM, the peak value of the diode current can be written as

$$i_{d_peak1i} = \frac{v_s}{L_{mi}} d_{sw1_i} T_s + \frac{v_b}{L_{mi}} d_{sw2_i} T_s\quad (5.20)$$

$$i_{d_peak2i} = \frac{v_s}{L_{mi}} d_{sw1_i} T_s - \frac{v_b}{L_{mi}} d_{sw3_i} T_s\quad (5.21)$$

where i_{d_peak1i} and i_{d_peak2i} are the peak values of the i th diode current under the discharging and charging operations, respectively. By applying the new control input d_{temp} in (5.20) and (5.21), we can obtain a simple representation as follows:

$$i_{d_peaki} = \frac{v_s}{L_{mi}} d_{sw1_i} T_s + \frac{v_b}{L_{mi}} d_{temp_i} T_s\quad (5.22)$$

where

$$-1 \leq d_{temp_i} \leq 1$$

Substituting (5.22) into (5.19) yields,

$$\bar{i}_{di} = \frac{d_{off_i}}{2} \left(\frac{v_s}{L_{mi}} d_{sw1_i} T_s + \frac{v_b}{L_{mi}} d_{temp_i} T_s \right)\quad (5.23)$$

Control input d_{off_i} cannot also be directly manipulated, thus should be changed to a controllable value such as d_{sw1} or d_{temp} . In DCM, d_{off} can be redefined as

$$\begin{aligned} v_{out} &= L_{mi} \frac{di_d}{dt} = L_{mi} \frac{i_{d_peak_i}}{T_s d_{off}} \\ d_{off_i} &= L_{mi} \frac{i_{d_peak_i}}{T_s v_{out}} \end{aligned} \quad (5.24)$$

Substituting (5.22) into (5.24) yields

$$\begin{aligned} d_{off_i} &= \frac{L_{m_i}}{T_s v_{out}} \left(\frac{v_{in}}{L_{m_i}} d_{sw1_i} T_s + \frac{v_b}{L_{m_i}} d_{temp_i} T_s \right) \\ &= \frac{v_{in} d_{sw1_i} + v_b d_{temp_i}}{v_{out}} \end{aligned} \quad (5.25)$$

By substituting (5.25) into (5.23), we obtain

$$\bar{i}_{di} = \frac{T_s}{2L_{m_i} v_{out}} (v_{in} d_{sw1_i} + v_b d_{temp_i})^2 \quad (5.26)$$

Assume that the L_{m_i} , d_{temp_i} and d_{sw1_i} have same values, (5.26) can be approximated as follows:

$$\bar{i}_{di} = \frac{T_s}{2L_m v_{out}} (v_{in} d_{sw1} + v_b d_{temp})^2 \quad (5.27)$$

and by substituting (5.27) into (5.18), the derivatives of s can be rewritten as

$$\dot{s} = \frac{\alpha_1 n T_s}{L_m v_{out} C_{out}} (v_{in} d_{sw1} + v_b d_{temp})^2 - \frac{\alpha_1 i_{out}}{C_{out}} + \alpha_2 x_1 \quad (5.28)$$

The control input d_{temp} consists an equivalent control input d_{eq} and a switching input u_{sw} . Using (5.28), d_{eq} in sliding mode, in which $\dot{s}(x) = 0$, can be calculated as

$$d_{eq} = \frac{1}{v_b} \sqrt{-\frac{2\alpha_2 L_m C_{out} x_1 v_{out}}{\alpha_1 n T_s} + \frac{2L_m P_{out}}{n T_s} - \frac{v_{in}}{v_b} d_{sw1}} \quad (5.29)$$

where

$$P_{out} = i_{out} v_{out}.$$

According to (5.16), $\dot{V}(s)$ should always be negative in order to guarantee controller stability and convergence to the sliding surface. To satisfy this condition, a saturation function is

used as u_{sw} as follows:

$$u_{sw} = \rho \text{sat} \left(\frac{s}{\delta} \right) = \begin{cases} \rho \frac{s}{\delta} & \text{if } |s| \leq \delta \\ \rho & \text{if } s > \delta \\ -\rho & \text{if } s < -\delta \end{cases} \quad (5.30)$$

where δ represents the thickness of boundary layers of the sliding surface and ρ is the control gain of the switching input. According to (5.28), sliding mode control input d_{temp} is included in squared term. Thus, the switching control input in (5.30) is added in the square root term of (5.29) for simplification. Subsequently, the final input of the proposed control system can be derived as

$$d_{temp} = \frac{1}{v_b} \sqrt{-\frac{2\alpha_2 L_m C_{out} x_1 v_{out}}{\alpha_1 n T_s} + \frac{2L_m P_{out}}{n T_s} - \rho \text{sat} \left(\frac{s}{\delta} \right) - \frac{v_{in}}{v_b} d_{sw1}} \quad (5.31)$$

and $\dot{V}(s)$ is calculated as

$$\begin{aligned} \dot{V}(s) &= s\dot{s} \\ &= s \left(\frac{\alpha_1 n T_s}{2L_m v_{out} C_{out}} (v_{in} d_{sw1} + v_b d_{temp})^2 - \frac{\alpha_1 i_{out}}{C_{out}} + \alpha_2 x_1 \right) \\ &= s \left(0 - \frac{\alpha_1 n \rho T_s}{2L_m v_{out} C_{out}} \text{sat} \left(\frac{s}{\delta} \right) \right) < 0 \end{aligned} \quad (5.32)$$

after which, the necessary condition to ensure the control stability and convergence to the sliding surface can be derived as

$$-\frac{\alpha_1 n \rho T_s}{2L_m v_{out} C_{out}} |s| < 0, \text{ if } |s| > \delta \quad (5.33)$$

$$-\frac{\alpha_1 n \rho T_s}{2L_m v_{out} C_{out}} \frac{s^2}{\delta} < 0, \text{ if } |s| \leq \delta \quad (5.34)$$

If design parameters α_1 , ρ , and δ have positive values when $s \neq 0$, then (5.33) and (5.34) are always negative. Fig.5.3 represents the overall control systems of the proposed converter. The final duty ratios of Q_2 and Q_3 are decided by the table in Fig. 5.3.

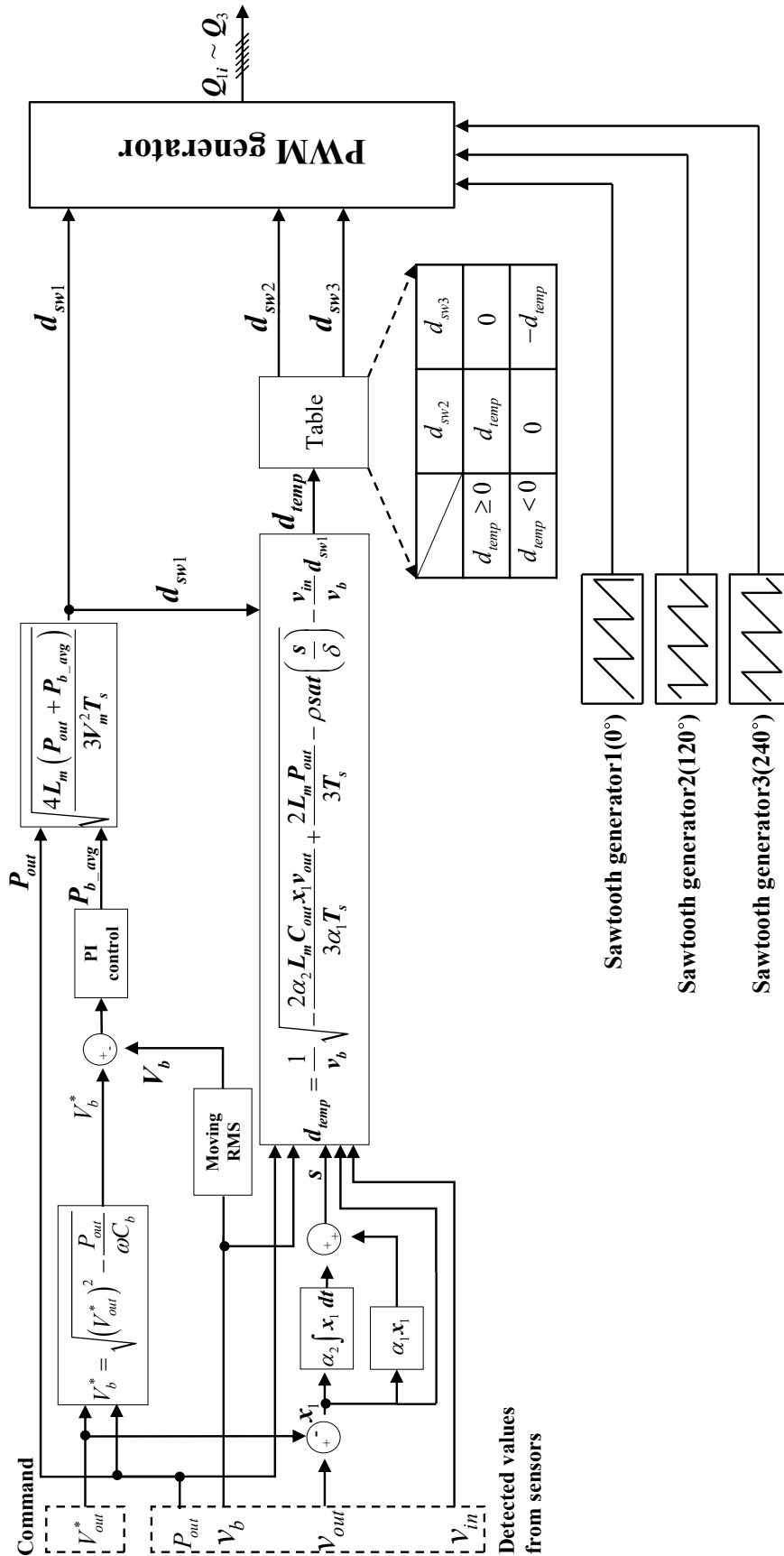


Figure 5.3: Overall control scheme of the proposed circuit

5.4 Circuit configuration of loss-less clamp snubber for proposed converter

The proposed circuit generates a reverse voltage during discharge operation. A snubber circuit is required to prevent component damage due to reverse voltage. However, the popular RCD snubber is not suitable for high power applications due to high losses. Under an output power of 2.5 kW, using a RCD snubber will result in a loss of about 31 W and requires a large volume of snubber resistance. For the miniaturization and high efficiency, it is necessary to apply a lossless snubber. The LC resonant circuit is applied to the secondary side as shown in table 5.1, and the detailed operation is shown in Fig. 5.4 This can significantly reduce losses and the volume of the snubber circuit.

Table 5.1: Snubber circuit comparison results

	RCD snubber	Loss-less clamp snubber
Snubber Loss	31W(1.24%, @2500W)	≈5W
Number of Components	3	4
Volume	●	●
Circuit Diagram		

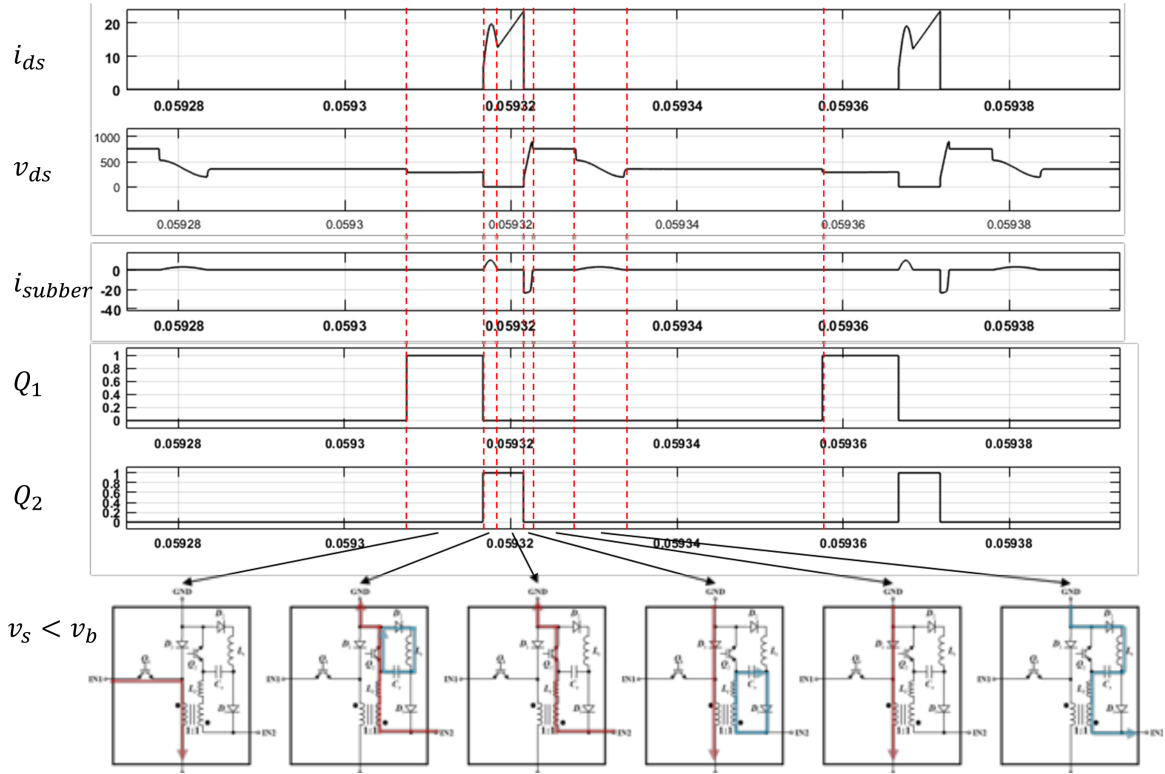


Figure 5.4: Lossless snubber operation and waveforms

5.5 Simulation studies

To check feasibility of the proposed circuit and the control system, MATLAB/SIMULINK is used as a test environment. Simulation parameters used are described in Table 5.2. Reference values of the output voltage and the control frequency of the buffer voltage and

Table 5.2: Simulation parameters

Parameter	Value	Parameter	Value
Grid voltage[Vrms]	220	Grid frequency[Hz]	50
Magnetization inductance[μH]	100	Buffer capacitor[μF]	135
Output capacitor[μF]	45	Switching frequency[kHz]	20
Design parameter α_1, α_2	1, 0.01	Design parameter ρ, δ	2500, 8
Window size of moving average filter	40	Proportional-Integral gain(K_p, K_i)	2, 0.01

sliding mode control were 400 V and 20 kHz, respectively.

Fig.5.5 shows simulation waveforms and control inputs before and after the APD operation. Before the APD operation, the ripple appeared at the output voltage, but after the APD operation, the ripple was removed. In Fig.5.6, we compare the waveforms of interleaved

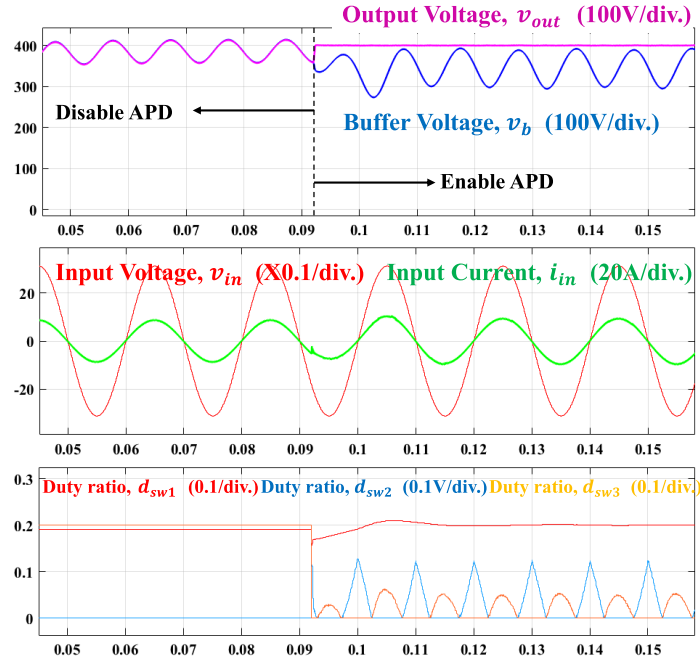


Figure 5.5: Waveforms and control inputs of the proposed control system

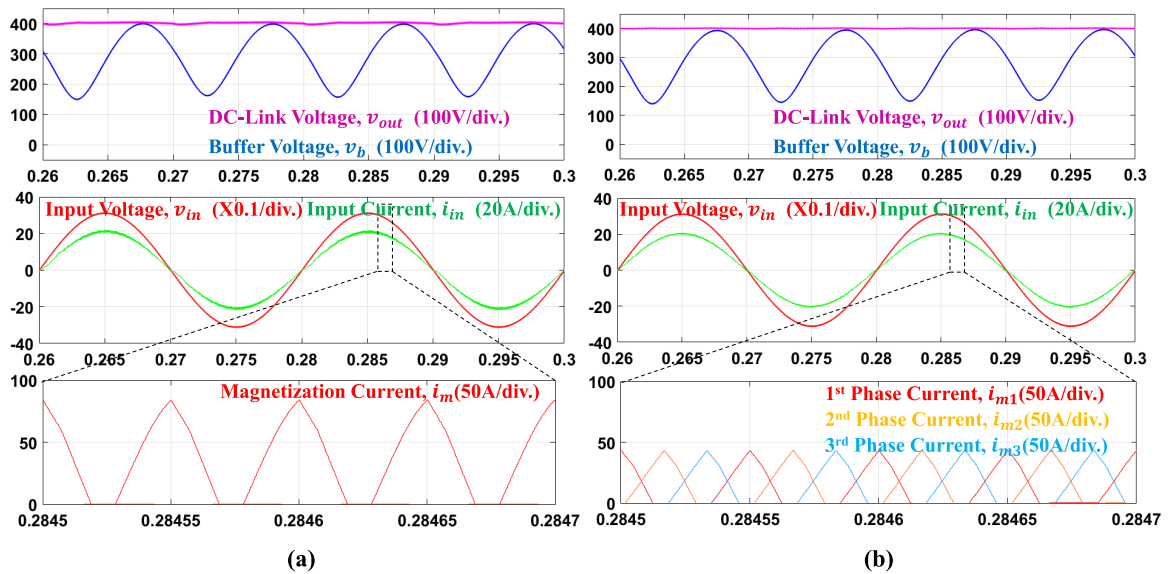


Figure 5.6: Waveform comparison (a) non-interleaved circuit [Input filter : $300\mu\text{H}$, $3\mu\text{F}$], (b) 3-phase interleaved circuit [Input filter : $30\mu\text{H}$, $3\mu\text{F}$]

and non-interleaved circuits. Fig.5.6(a) shows that a larger input filter(300 μ H) is needed to reduce the ripple of the input current to less than 1 A. In the case of Fig.5.6(b), the inductance of the input filter required to reduce the current ripple to the same level as (a) can be reduced to 30 μ H through the interleaving operation.

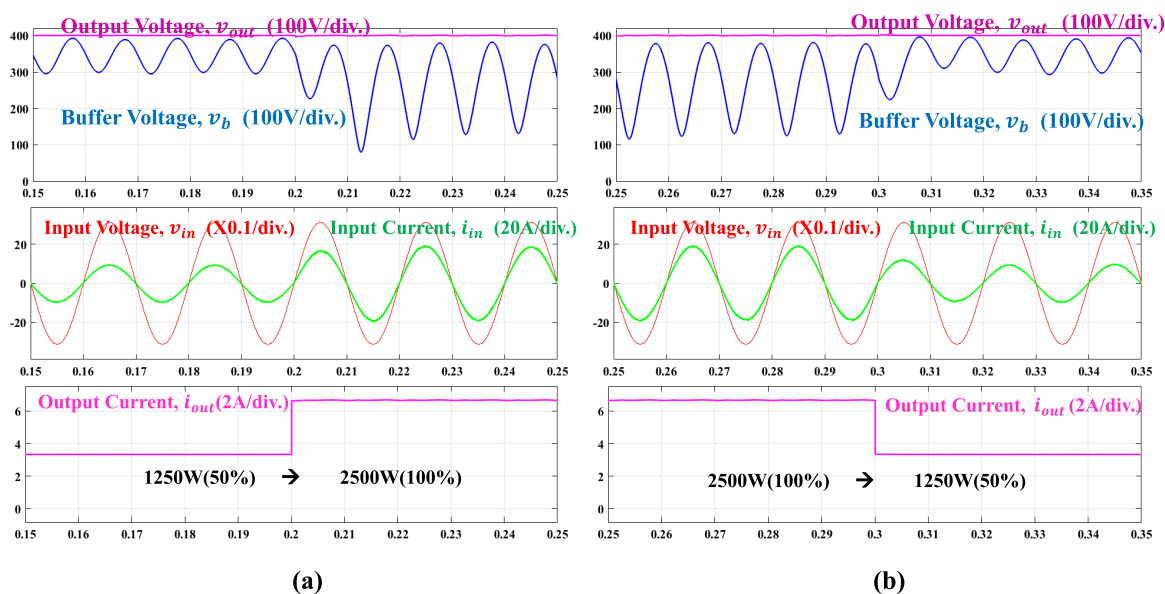


Figure 5.7: Waveform in the transient response during (a) 1250 W to 2500 W and (b) 2500 W to 1250 W load steps

Fig.5.7 shows the operation of the APD when sudden load changes. Even when the load power instantaneously rises or falls, the output voltage is stably controlled by the proposed control system.

The proposed sliding mode control ensures stability even if the inductance of the actual coupled-inductor does not match the design value. As a result of simulating 10 % inductance error, output voltage distortion and over and under shoot did not occur.

5.6 Conclusion

In this paper, we propose a interleaving topology of the APD circuit and SMC method. Through the MATLAB / SIMULINK simulation for the AC/DC buck-boost conveter circuit with APD function, we could verify the transient stability and tracking performance of the proposed control system during APD operation and load variation. In addition, The size of the input filter can be reduced to 10 % compare with the non-interleaved circuit. And,by minimizing the number of inductors, the size and manufacturing cost of the basic decoupling circuit can be reduced.

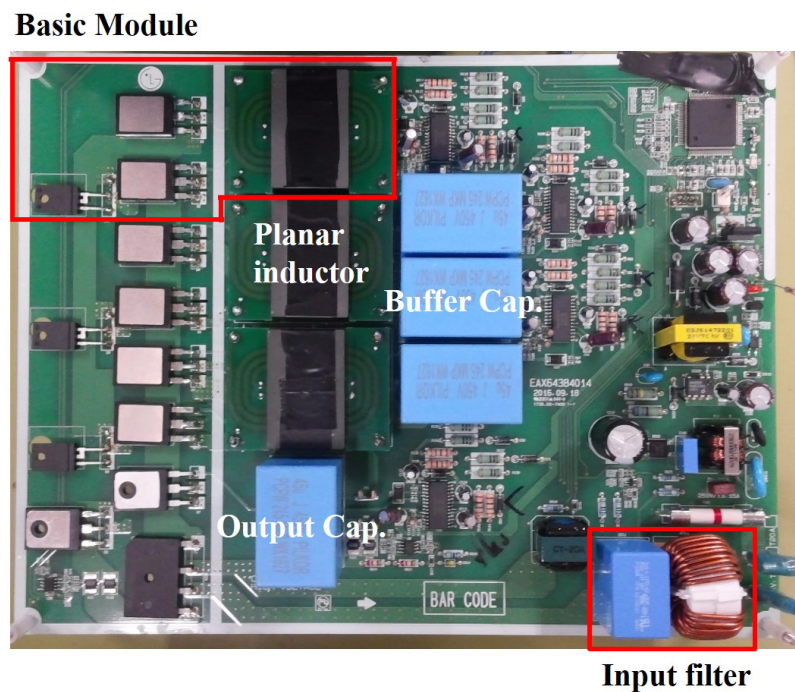


Figure 5.8: A prototype of the interleaved converter based on the proposed APD circuit

As shown in Fig. 5.8, the prototype of the proposed circuit is implemented on a single PCB, with both input filters and inductors. The proposed circuit achieves the power conversion device with miniaturization and long lifespan.

CHAPTER 6

Implement APD function for bridge-less SEPIC without auxiliary circuit

6.1 Contribution Summary

In this chapter, a control method is proposed to address the problem of control of APD circuits based on the bridge-less SEPIC. Previously, PI plus resonant control techniques were applied to APD control, but this method has the problem that global stability cannot be guaranteed under conditions where uncertainty exists in a parameter or model. To solve this problem, the Lyapunov function based control method was applied to the control system in this paper. This control method ensures the global stability of the system and performance at various operation conditions.[34] [35] It also changed the current control method to reduce the number of sensors required for control. The proposed control method uses MATLAB / SIMULINK to validate its effectiveness against the PI-Resonant control strategy.

6.2 Operation and Modeling of the Bridge-less SEPIC PFC Rectifier

Fig. 3 shows the bridge-less SEPIC proposed in [36]. They implemented a PFC converter without a diode bridge by placing two IGBTs, including freewheeling diodes, vertically. In [37], input power ripple is removed by using these two IGBTs and C_b and L_{m2} . The op-

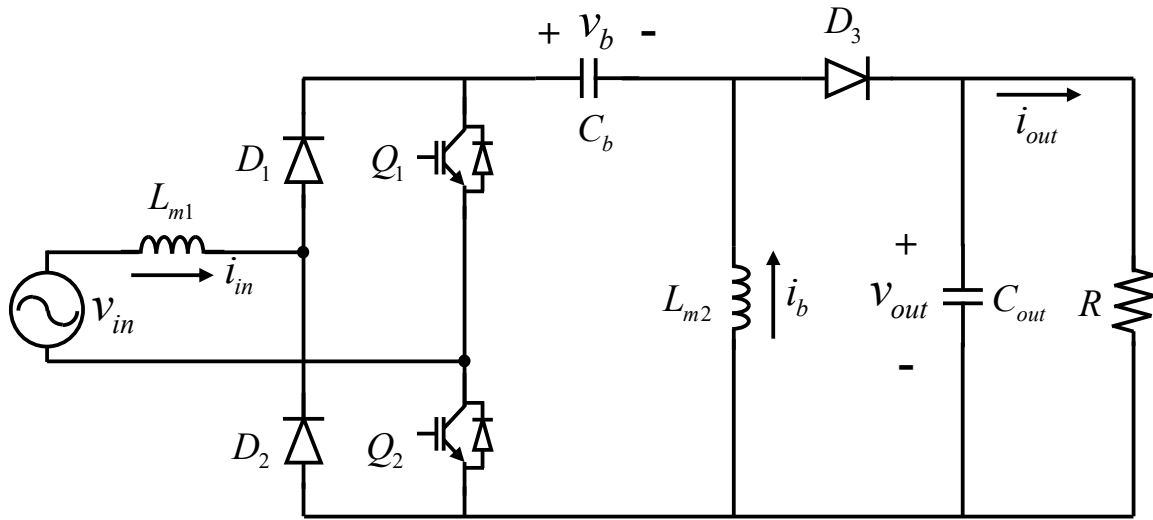


Figure 6.1: Bridge-less SEPIC PFC rectifier

eration of the bridge-less SEPIC proposed by [?] is divided into three operation modes as shown in Fig. 4.

-Mode1: Switch1(Q_1) and Switch2(Q_2) are on. L_{m1} and L_{m2} charge magnetic energy from the power system and the buffer capacitor.

-Mode2: Switch2(Q_1) is on and Switch2(Q_2) is off. Stored energy in the L_{m2} moves to the output terminal. In this mode, insufficient energy is compensating.

-Mode3: All switches (Q_1, Q_2) are off, storing energy in each inductor is discharging to the output terminal.

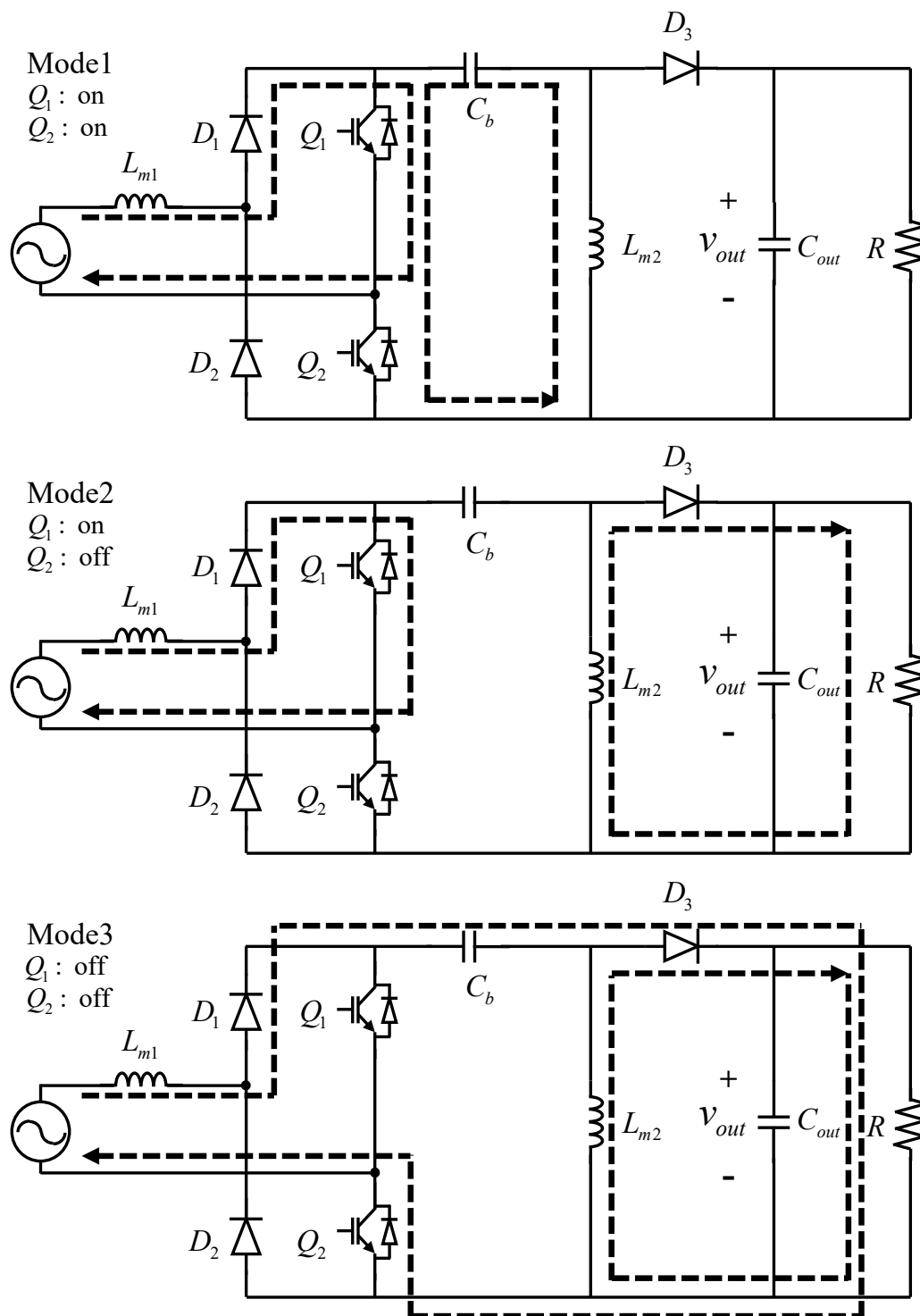


Figure 6.2: Bridge-less SEPIC PFC rectifier current flow according to a combination of switches.

In [3], only mode1 and mode3 used. In [4], mode2 was added to control the charge and

discharge amount of the buffer capacitors. The state space equations describing the APD operation of the bridge-less SEPIC PFC rectifier can be written as

$$L_{m1}\dot{i}_{in} = (v_{in} + v_b + v_{out})u_1 - (v_b + v_{out}) \quad (6.1)$$

$$C_{out}\dot{v}_{out} = (1 - u_1)i_{in} + (1 - u_2)\bar{i}_b - i_{out} \quad (6.2)$$

where \bar{i}_b , u_1 and u_2 are an average buffer current, duty ratios of the Q_1 and Q_2 , respectively.

6.3 Proposed Control Strategy

In this paper, input current and the output voltage is the control targets for unity power factor and constant output. Defining the state variables as

$$x_1 = i_{in} - i_{in}^* \quad (6.3)$$

$$x_2 = v_{out} - v_{out}^* \quad (6.4)$$

The input for the current control can be defined regarding its steady state and perturbed terms as follows

$$u_1 = U_0 + \Delta u \quad (6.5)$$

where U_0 and Δu are the steady state and perturbed values of control input, respectively. Assuming that all the states and input are in steady states, the steady state of (4) can easily be obtained as

$$L_{m1}\dot{i}_{in}^* = (v_{in} + v_b + v_{out}^*)U_0 - (v_b + v_{out}^*) \quad (6.6)$$

Then, the steady control input U_0 is as follows

$$U_0 = \frac{1}{v_{in} + v_b + v_{out}^*} (L_{m1}\dot{i}_{in}^* + v_b + v_{out}^*) \quad (6.7)$$

The error dynamics of x_1 can be obtained as follows

$$L_{m1}\dot{x}_1 = (v_{in} + v_b + v_{out})\Delta u + x_2U_0 - x_2 \quad (6.8)$$

Similarly, the error dynamics of (5) can be written as

$$C_{out}\dot{v}_{out} = C_{out}\dot{x}_2 = (1 - u_1)i_{in} + (1 - u_2)\bar{i}_b - i_{out} \quad (6.9)$$

Assume that the i_b works in DCM, than the $(1 - u_2)\bar{i}_b$ in (6.9) can be rewritten as follows

$$C_{out}\dot{x}_2 = i_{in} - i_L - i_{in}u_1 + \frac{v_b^2 T_s}{2L_{m2}v_{out}}u_2^2 \quad (6.10)$$

As shown in (13), when the buffer current operates with DCM, the buffer current can be estimated only by the buffer voltage and the output voltage. Therefore, the number of sensors required for control can be reduced by one.

According to Lyapunov's direct method, the equilibrium point is globally asymptotically stable if $V(x)$ satisfies following properties.

1. $V(0) = 0$
2. $V(x) > 0, \forall x \neq 0$
3. $V(x) \rightarrow \infty$ as $\|x\| \rightarrow \infty$
4. $\dot{V}(x) < 0, \forall x \neq 0$

To obtain nonlinear control inputs which make the globally asymptotic stable, following Lyapunov candidate function is used.

$$V(x_1, x_2) = \frac{1}{2}L_{m1}x_1^2 + \frac{1}{2}C_{out}x_2^2 \quad (6.11)$$

This function satisfies three properties(1 ~ 3) of Lyapunov's direct method. The aim is to make the derivative of V negative definite. Thus, \dot{V} is obtained from (14) which yields to

$$\dot{V}(x_1, x_2) = x_1 L_{m1} \dot{x}_1 + x_2 C_{out} \dot{x}_2 \quad (6.12)$$

Let $L_{m1}\dot{x}_1$ and $C_{out}\dot{x}_2$ be defined as follows.

$$L_{m1}\dot{x}_1 = -k_1 x_1, \quad C_{out}\dot{x}_2 = -k_2 x_2 \quad (6.13)$$

where k_1 and k_2 are strictly positive design values. Then, \dot{V} is negative definite as follows.

$$\dot{V} = -k_1 x_1^2 - k_2 x_2^2 < 0, \quad \forall (x_1, x_2) \neq (0, 0) \quad (6.14)$$

Using (6.13), perturbed control input Δu can be obtained as follows

$$\Delta u = \frac{1}{v_{in} + v_b + v_{out}} (x_2 - x_2 U_0 - k_1 x_1) \quad (6.15)$$

Then,

$$\begin{aligned}
 u_1 &= \Delta u + U_0 \\
 &= \frac{x_2 - k_1 x_1}{v_{in} + v_b + v_{out}} + \frac{1 - x_2 (L_{m1} \dot{i}_{in}^* + v_b + v_{out}^*)}{(v_{in} + v_b + v_{out}^*) (v_{in} + v_b + v_{out})}
 \end{aligned} \tag{6.16}$$

where

$$I_m = k_p (v_{b_avg}^* - v_{b_avg}) + k_i \int (v_{b_avg}^* - v_{b_avg}) dt \tag{6.17}$$

In the same manner, u_2 for the output voltage control can calculate as follows.

$$u_2 = \frac{1}{v_b} \sqrt{\frac{2L_{m2} (P_{out} + v_{out} i_{in} (u_1 - 1) - k_2 x_2)}{T_s}} \tag{6.18}$$

where

$$P_{out} = \frac{v_{out}^2}{R}$$

Fig. 6.3 shows the complete control system. A bandstop filter is used to obtain the average value of the buffer voltage. In addition, to obtain the phase of the input voltage for power factor control, the phase locked loop was used. According to the sign of the input voltage, it was decided by a separate table to vary the duty applied to Q_1 and Q_2 .

6.4 Simulation Results

To check the proposed feasibility, MATLAB/SIMULINK used as a testing environment. Table 6.1 and Table 6.2 show the parameters and conditions used in the simulations. Fig.6.4 shows the conventional control system proposed in [?]. Comparing Fig. 5 and Fig. 6, it can be seen that the number of PI controllers used in the proposed method is significantly reduced compared to the conventional method.

Table 6.1: Simulation parameters

Parameter	Value	Parameter	Value
Input voltage[V_{rms}]	230	Grid frequency[Hz]	50
Inductance of L_{m1} [mH]	10	Inductance of L_{m2} [mH]	0.3
Buffer capacitor[μ F]	60	Output capacitor[μ F]	60
Switching frequency[kHz]	20	Reference of the output voltage[V]	350

Table 6.2: Design parameters of the proposed method and PI+PR control

Parameter	PI+PR control[?]	Proposed method
k_1, k_2	-	200, 500
PI gain for I_m	0.05, 0.0001	0.05, 0.0001
PR gain for i_{in}	10, 300	-
PI gain for v_{out}	3, 0.004	-
PI gain for i_{out}	3, 0.004	-

The effectiveness of the proposed control method is verified against the conventional control method at various conditions, e.g., steady-state conditions, load variation conditions, and input voltage variation conditions.

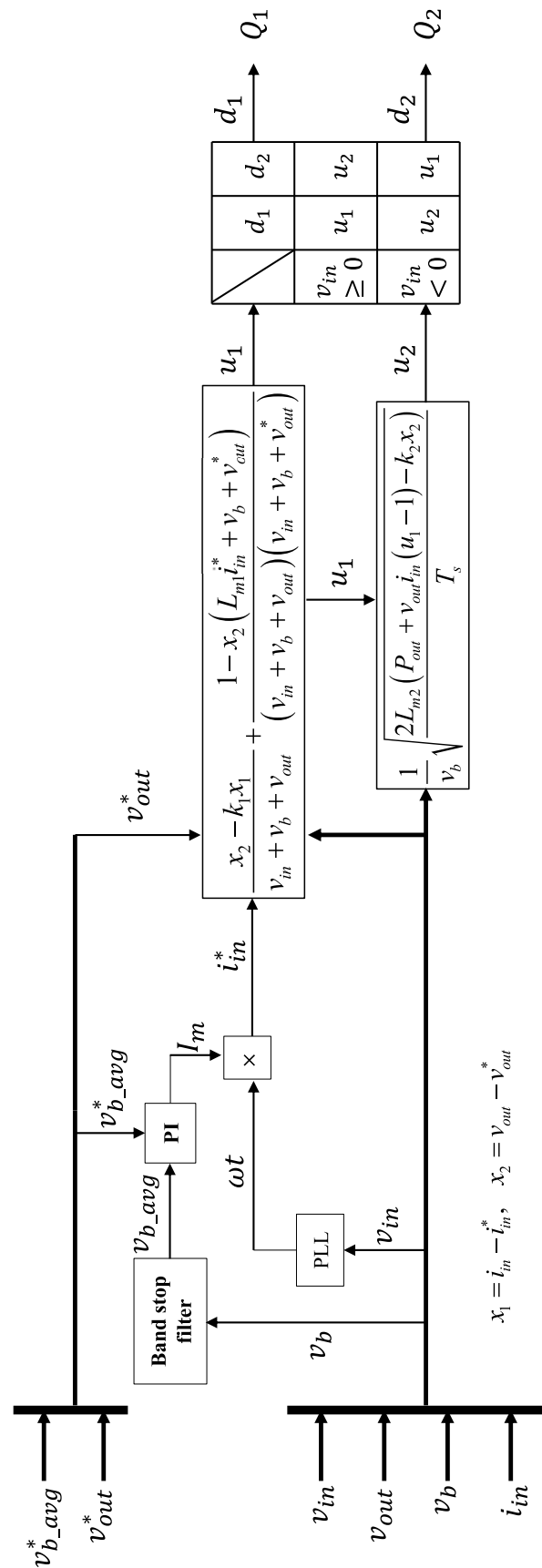


Figure 6.3: Proposed control system

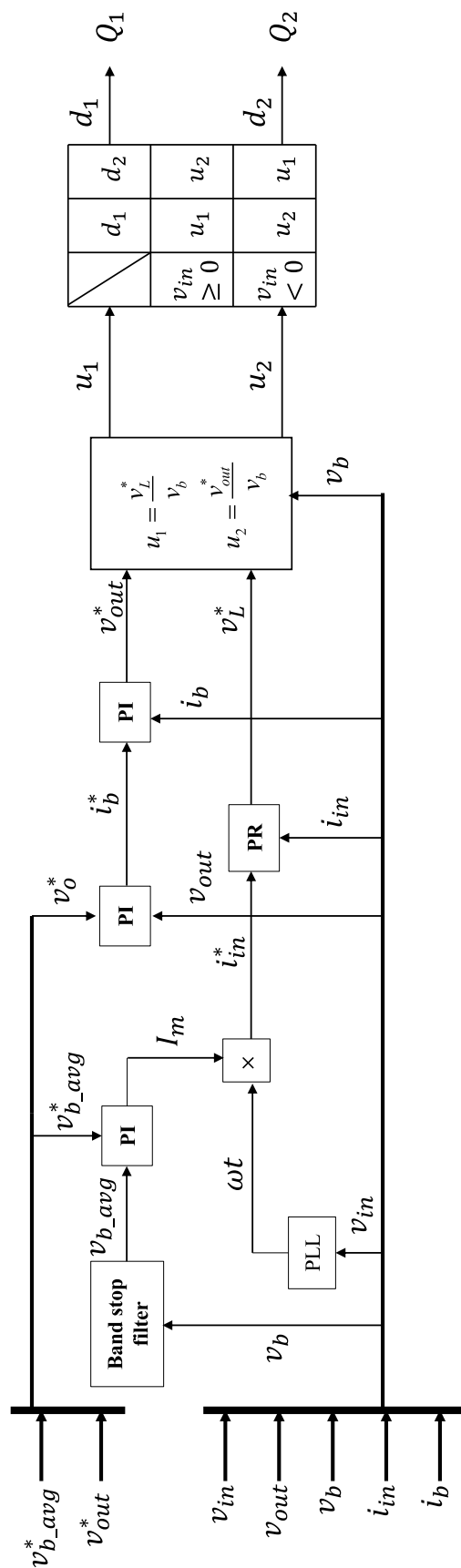


Figure 6.4: Conventional control system in [37]

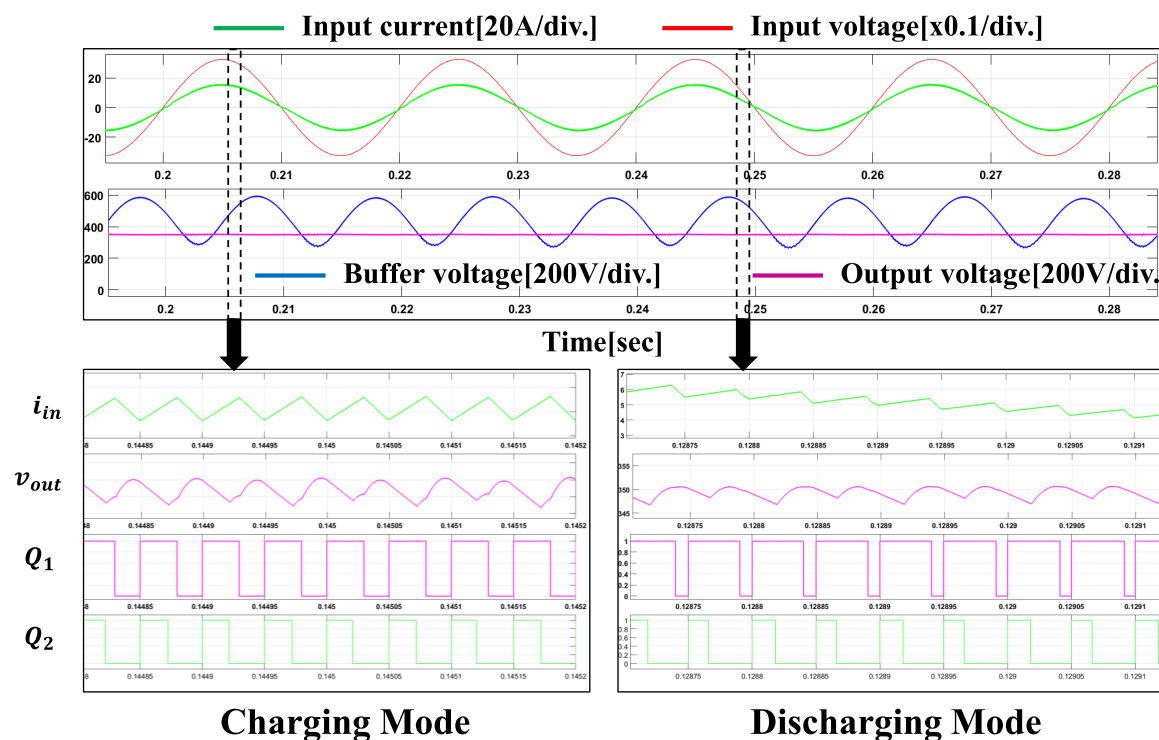


Figure 6.5: Waveform and switch operation of bridge-less SEPIC by APD operation mode.

Fig. 6.5 shows the mode-specific operation of the APD function. When the input voltage increases and surplus energy is generated, the decoupling circuit switches to the charging mode and stores the surplus energy in the buffer capacitor. At this time, the duty ratio of Q_2 is decreased, and the energy to be charged is larger than the energy discharged from the buffer capacitor. Conversely, when the input voltage decreases and the output power becomes insufficient, the buffer capacitor is discharged. That is, by increasing the duty ratio of Q_2 , the energy discharged from the buffer capacitor is made larger than the energy charged.

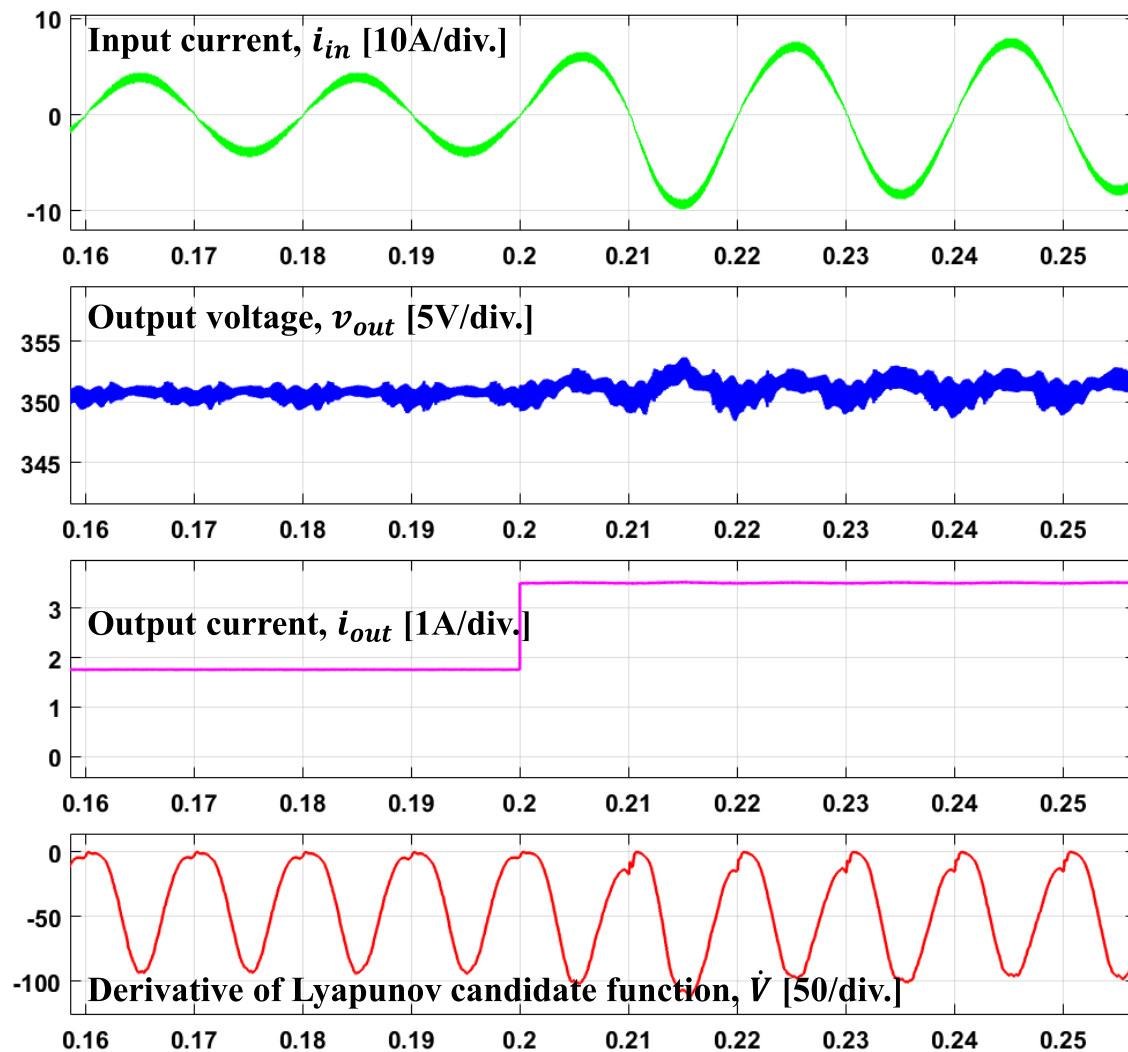


Figure 6.6: Simulation for global stability of the proposed control methods in the load variation condition

Fig.6.6 shows the simulation results of applying the proposed control method to the SEPIC under load-varying conditions. It can be confirmed that the input current has a unity power factor as a sine wave and the output voltage is kept constant even if the load is varied. Also, since \dot{V} is always negative, it can be confirmed that the control system is globally stable.

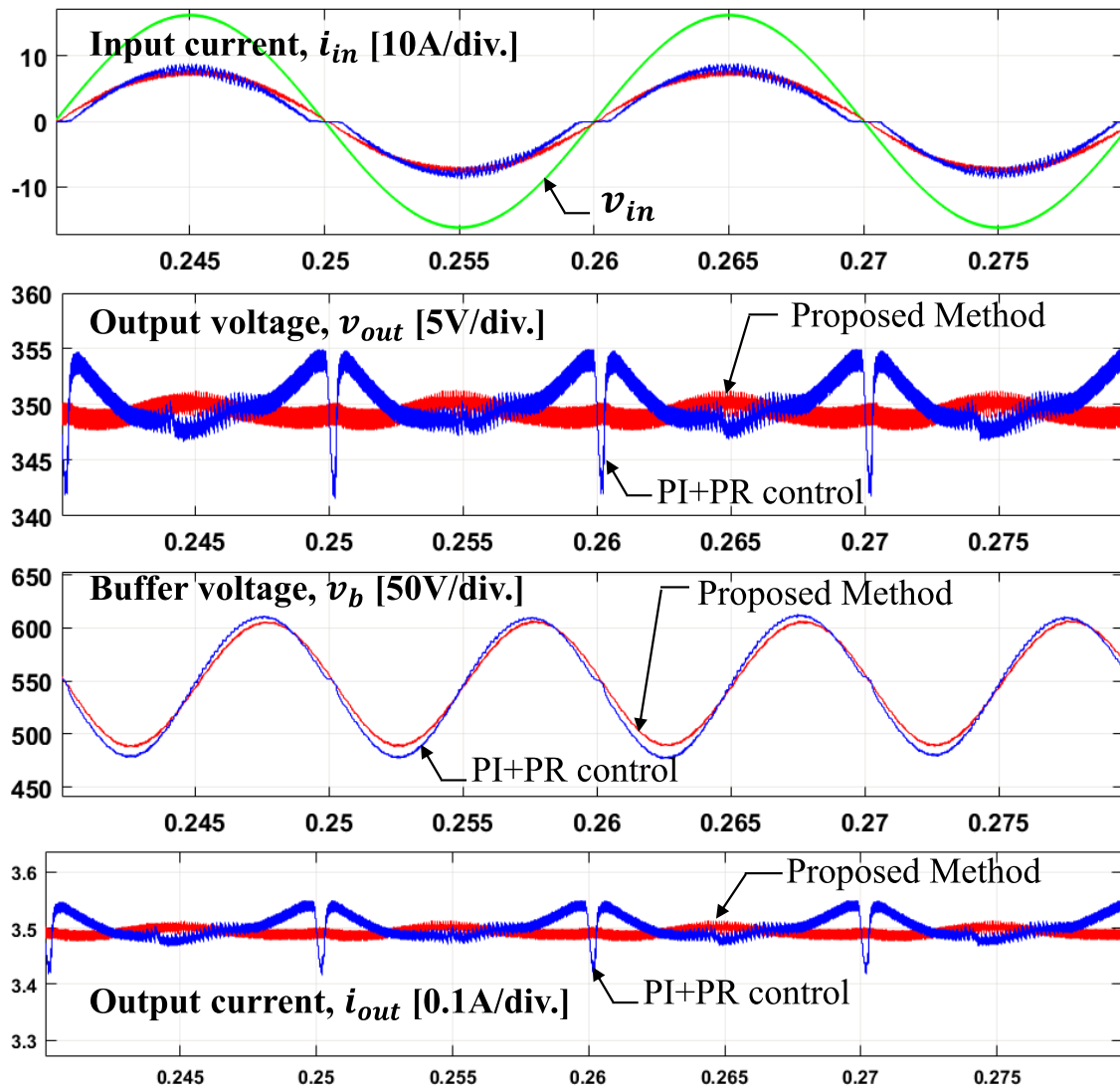


Figure 6.7: Comparison of control performance in the steady state, Red line: Proposed control method, Blue line: Method in [37]

Fig. 6.7 shows the results of a simulation comparing the performance of the control method proposed under steady-state conditions with the conventional control method. The proposed method provides a smaller steady-state error of output voltage and current compared to the conventional method, and the THD of the input current is 3.77 %, significantly lower than the conventional(11.07 %). The proposed method has output voltage ripple of 2V, and the conventional method is 12V. That is, although the proposed method uses a smaller number of sensors and parameters than the conventional method, it has an advantage in performance.

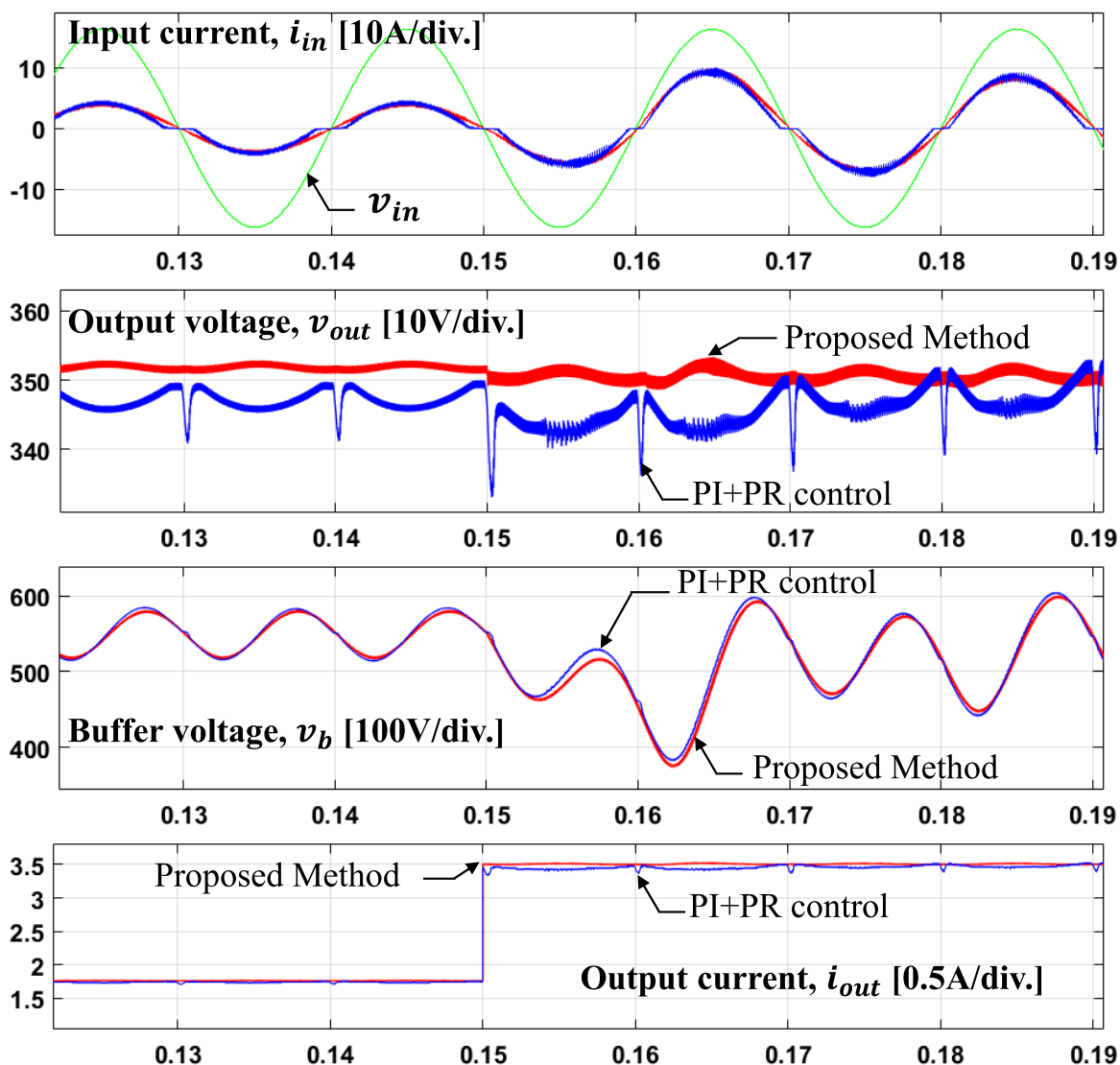


Figure 6.8: Comparison of controller performance under load change conditions, Red line: Proposed control method, Blue line: Method in [37]

Fig. 6.8 shows a comparison of the performance of the controller under conditions of rapid load changes. Conventional methods show that the ripple of output voltage increases as the load increases and take time to converge to normal conditions. On the other hand, the proposed method shows that the output voltage remains at a steady-state even when load changes occur, and the ripple voltage is not as large as it used to be.

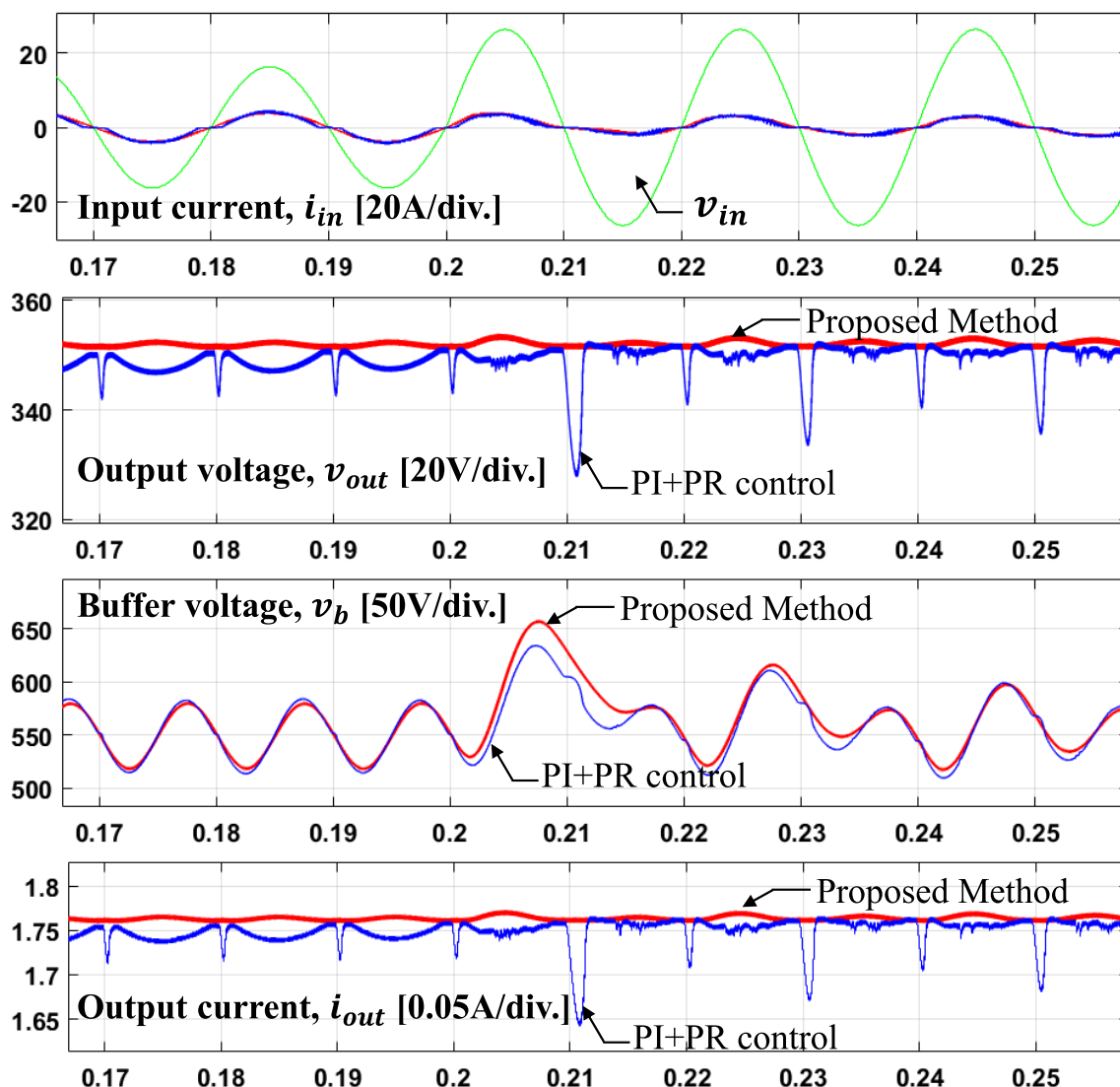


Figure 6.9: Comparison of controller performance under input voltage change conditions, Red line: Proposed control method, Blue line: Method in [?]

Fig. 6.9 shows the simulation results comparing the performance of the controller under the condition that the input voltage changes from $230 V_{rms}$ to $300 V_{rms}$. The proposed method does not change the magnitude of the ripple voltage even if the input voltage changes. On the other hand, in the case of the conventional method, it can be seen that the ripple voltage instantaneously increases ($20 V$). As a result, it can be confirmed that ripples are generated in the output current.

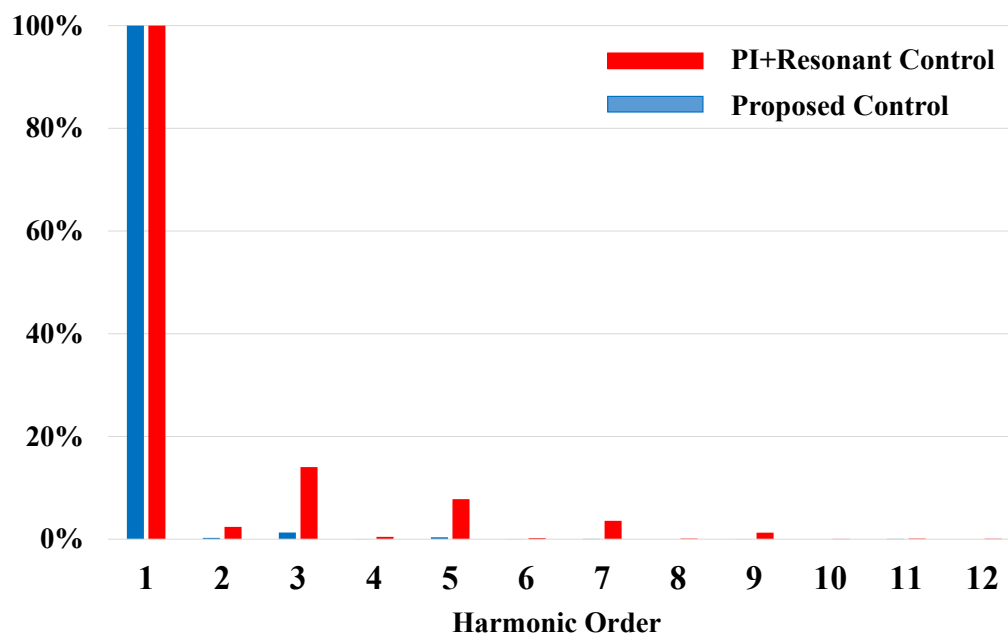


Figure 6.10: Harmonic current spectrum of the input current, conventional control method (red), proposed control method (blue)

Fig. 6.10 shows the harmonic component for the input current. Compared with the conventional control method, the proposed method shows that the harmonic component is low in the entire order.

6.5 Conclusion

In this paper, we applied a Lyapunov function based control strategy for the APD control of Bridge-less SEPIC. Simulation using MATLAB / SIMULINK verifies the effectiveness of the proposed control scheme. Table 6.3 shows the comparison between the conventional control method and the proposed method. As a result of the comparison, we confirmed that the proposed method is superior in stability and accuracy and THD is lower. Also, the proposed method offers DCM control of the buffer current to reduce the number of sensors and a significant reduction in design parameters to facilitate controller design.

Table 6.3: Comparison between the proposed control method and the conventional method

Index	PI+PR control[37]	Proposed method
Global stability	Not guarantee	Guarantee
Number of sensors	5	4
Design parameters	8	4
Maximum v_{out} ripple	20 V	5 V
Maximum THD	11.07 %	3.77 %

CHAPTER 7

Reducing voltage stress of Bridge-less SEPIC based active power decoupling circuit

7.1 Contribution summary

This chapter proposes a method to reduce the voltage stress of the APD circuit based bridge-less SEPIC as referred in chapter 6. The conventional APD circuit based bridge-less SEPIC operates at high buffer voltage. Therefore, the voltage stress of the components constituting the converter is increased, which increases the volume and cost of the parts. Therefore, in order to optimize the manufacturing cost and volume, it is necessary to reduce the voltage stress of the parts. In this chapter, we modified the circuit and control method of the conventional bridge-less SEPIC so that the APD function operates even at low voltage.

7.2 Proposed circuit and control method

As shown in Fig. 6.1, when the buffer capacitor is discharged, the voltage across the inductor is $v_b d_2$. If $v_b d_2$ is lower than the input voltage and the output voltage, the input current will reversely flow to L_{m2} in this interval. Fig. 7.1 shows the simulation results when the target buffer voltage (350 V) is same with the output voltage (350 V). In this case, the energy is not transmitted to the output terminal, and the output voltage is distorted.

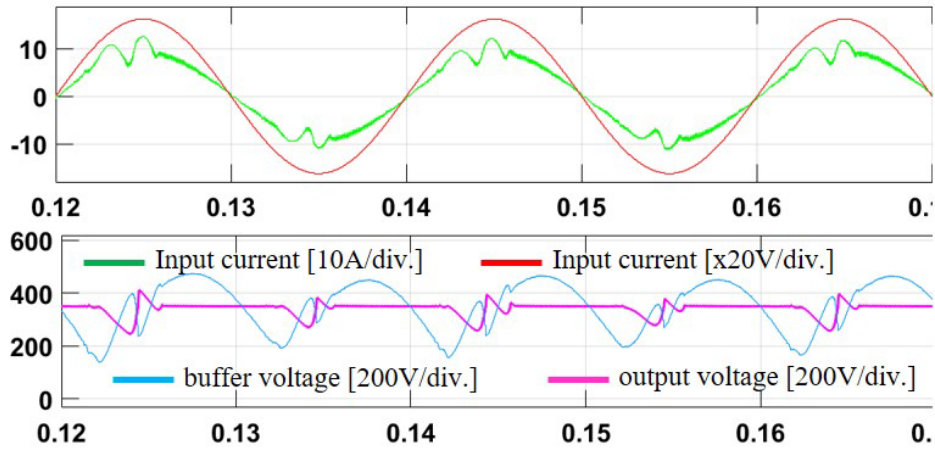


Figure 7.1: Waveforms with target buffer voltage of 350 V

To prevent reverse flow to L_{m2} , the circuit has been modified as follows. Diodes and snubber capacitors were used to prevent reverse currents in conditions where $v_b d_2$ is lower than the input and output voltages.

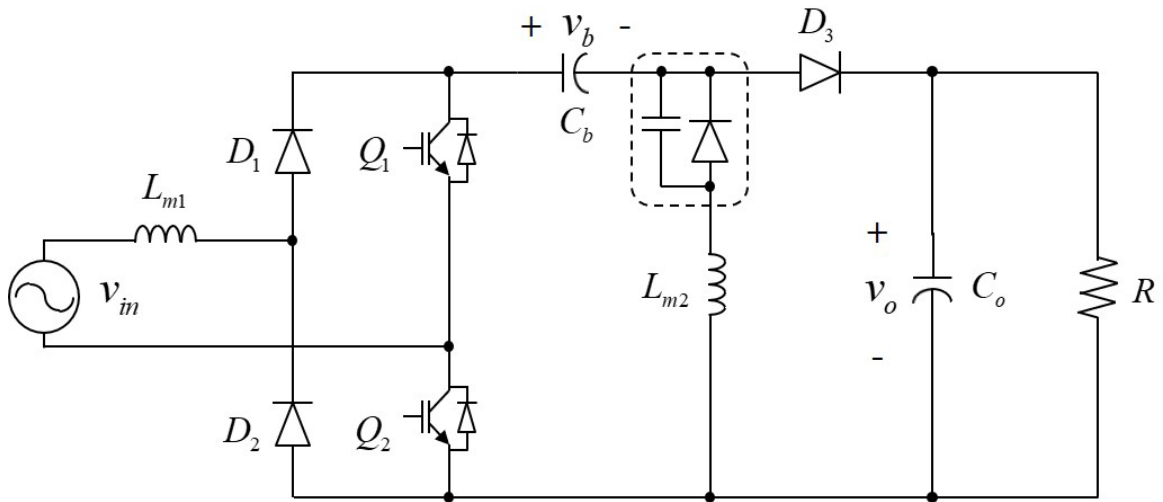


Figure 7.2: Proposed circuit

7.3 Simulation results

Fig. 7.3 shows the simulation results for a modified circuit. As shown in the Figure, no distortion occurs in the waveform. However, zooming in on the output voltage waveform shows that a ripple voltage of approximately 16 V exists. This is because for the APD control of the bridge-less SEPIC, the charging control of the buffer capacitor is dependent

on the input current control. Under conditions where the voltage of the buffer capacitor is low and the input current is high, the output voltage is over-charged regardless of APD control.

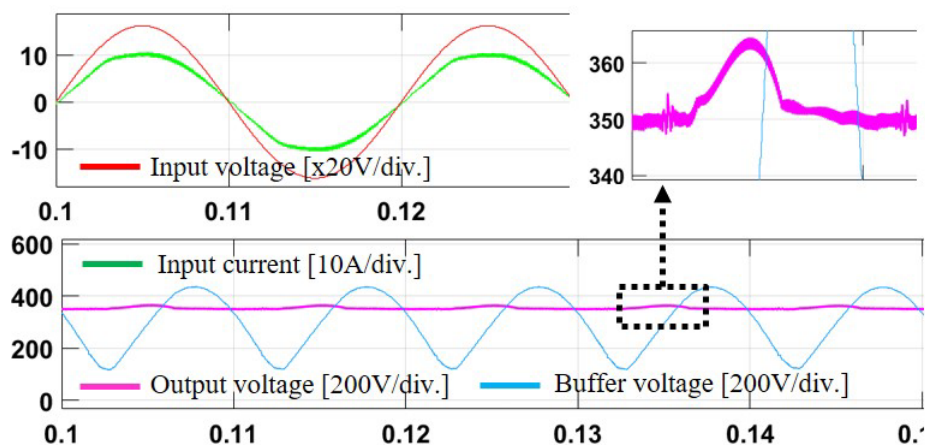


Figure 7.3: Simulation waveforms of the proposed circuit

To reduce the ripple voltage of the output capacitor, it is necessary to lower the peak value of the input current. For this purpose, the method of injecting a 3rd harmonic current into the current reference as follows:

$$i_{in_ref} = I_m(\sin\omega t + k_{3rd}\sin3\omega t) \quad (7.1)$$

As shown in Fig. 7.4, as the ratio of the 3rd harmonic current increases, the peak value of the current decreases. However, since the harmonic injection method increases the harmonic current, it should be decided by considering the margin against the regulatory limit at the maximum current condition.

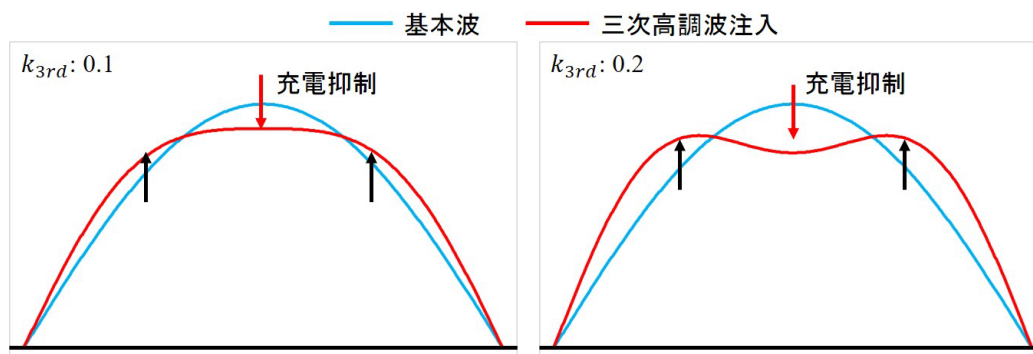


Figure 7.4: Current wave due to ratio of 3rd harmonic current

Fig. 7.5 represents the harmonic spectrum according to the change of k_{3rd} under the maximum current condition. If the third harmonic is 30% of the fundamental wave, it can be

seen that it exceeds the regulatory limit value. In this paper, 10% is applied considering margin.

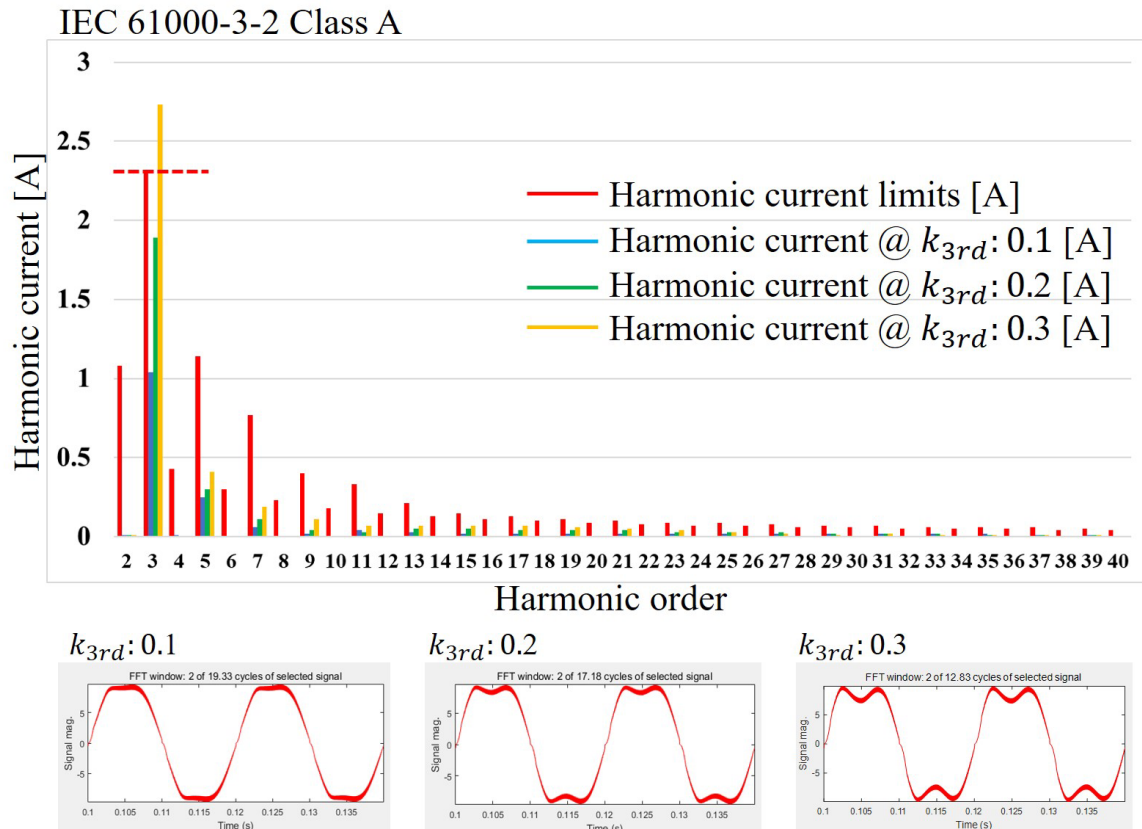


Figure 7.5: Analysis of harmonic spectrum according to k_{3rd} value

Fig. 7.6 shows simulation results for the case where both circuit modification and harmonic current injection are applied. The output voltage ripple decreased from 16 V to 8 V, and the maximum voltage of the buffer capacitor decreased from 550 V to 430 V. This makes it possible to use low rated voltage components and thus reduce manufacturing costs. In addition, the volume of the condenser could be reduced by 20%.

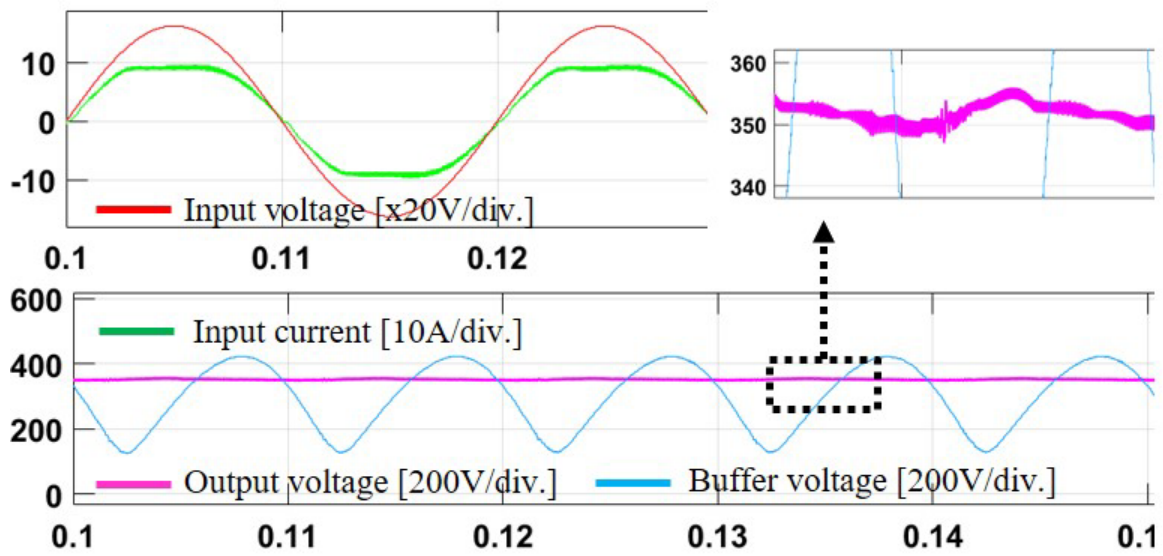


Figure 7.6: Simulation results for applying 3rd harmonic injection method.

Summary and recommendations for future study

8.1 Summary

The APD circuit allows smooth function to be implemented even with a small capacity capacitor, thereby improving longevity and reliability by removing the passive decoupling method of using a large capacity E-Caps. However, the problem was that APD method required additional passive components and switches to actively control the ripple power. This limited the complexity, volume and manufacturing costs of the converter circuits. To deal with these problems, various methods have been studied to reduce the number of inductors that account for a large portion of volume and manufacturing costs. However, there is a limitation of previous studies not taking into account the voltage stress of a circuit. As voltage stress increases, components with higher rated voltages should be used. In particular, film capacitors significantly increase the price of volume as the rated voltage increases. In addition, conventional APD-based control schemes are a type of linear control that fails to ensure stability and reliability under adverse conditions such as various operating points, output disturbances and parameter variations.

In order to solve these problems, voltage stress was reduced by multiplying inductors to reduce the number of magnetic cores and by constructing an APD circuit with a buck type. In addition, the proposed APD circuit could be applied to the interleaved converter to reduce the size of the input and output filters, thereby reducing the size of the converter circuit. In addition, the APD function was implemented by changing the existing bridge-less SEPIC circuit only to control it without additional components. This has made it possible to significantly reduce manufacturing costs. The circuits proposed above were common to SMC and Lyapunov function based controls. By doing so, it was able to robust the influence of process error of passive components, sensor noise and disturbance.

8.2 Recommendations for future study and implications for research

The operating range of the buffer voltage depends on the structure of the APD circuit. Therefore, the appropriate APD circuit should be selected considering the voltage and power required by the product. If the required output voltage is low, the capacity of the capacitor can be further reduced by using a boost type APD circuit. If the required output voltage and power are high, it is recommended to use a buck type APD circuit to lower the voltage stress to make parts with lower rated voltage. This reduces the cost and volume of parts. When the output voltage and power are changed to a large range, various operating conditions can be satisfied by applying a buck-boost type APD circuit.

The controllers proposed in this study commonly use a method of controlling the average value of the buffer voltage. For this purpose, a filter such as a moving RMS is used in the controller. However, when the parameter or load fluctuates suddenly, the transient characteristic of the output voltage and the input current may be deteriorated due to the slow response speed of the buffer voltage controller. In the SMC controller proposed in Section 3, there is a condition that the inductor current must operate as DCM in order to operate in sliding mode. If the buffer voltage drops below a certain value due to a slow response speed, the DCM will not operate, resulting in distortions in the output voltage and input current. If we can improve the slow response speed of the average buffer voltage control, we expect to have stable and high accuracy control over a wider range.

8.3 Conclusions

The longer the time the power converter operates at high temperatures, the greater the failure rate of the E-Caps. In particular, it can be a serious problem for products that are exposed to the outside world, such as an air conditioner or an electric vehicle battery charging station. For example, global warming is driving the trend towards increasing air-conditioner uptime, leading to an increase in the amount of time E-Caps operates at high temperatures. As a result, the life expectancy of the air conditioner is shortened. This will become a serious problem over time, and the APD approach can be the most appropriate solution to solve these problems. In order to apply APD circuit to actual products, problems such as manufacturing cost and reliability of APD circuit should be continuously improved. The multiplexing and voltage stress reduction design proposed in this study can be one of the solutions. Nonlinear control such as SMC and Lyapunov function based control can also be a solution to the reliability and performance improvement of the APD circuit.

References

- [1] T. Tafticht, K. Agbossou, A. Cheriti, "DC Bus Control of Variable Speed Wind Turbine Using a Buck-Boost Converter", IEEE Power Engineering Society General Meeting, pp. 5, 16 October 2006
- [2] Ray-Lee Lin, Yi-Chun Chang, Chia-Chun Lee, "Optimal Design of LED Array for Single-Loop CCM BuckBoost LED Driver", IEEE Transactions on Industry Applications, VOL 49, pp. 761 - 768, 20 March 2013
- [3] Quan Li, Peter Wolfs, "A Review of the Single Phase Photovoltaic Module Integrated Converter Topologies With Three Different DC Link Configurations", IEEE Transactions on Power Electronics, VOL. 23, NO. 3, May 2008
- [4] S. Yang, A. Bryant, P. Mawby, D. Xiang, R. Li, and P. Tavner, "An Industry-Based Survey of Reliability in Power Electronic Converters," IEEE Transactions on Industry Applications, vol. 47, pp. 1441-1451, 2011.
- [5] Huai Wang, and Frede Blaabjerg, "Reliability of capacitors for DC-link applications in power electronic converters-An overview", IEEE Transactions on Industry Applications, VOL. 50, NO. 5, September/October 2014
- [6] Philip T. Krein, Robert S. Balog and Mehran Mirjafari, "Minimum Energy and Capacitance Requirements for Single-Phase Inverters and Rectifiers Using a Ripple Port", IEEE Transactions on Power Electronics, VOL. 27, NO. 11, November 2012
- [7] W. Qi, H. Wang, X. Tan, G. Wang, and K. D. T. Ngo, "A novel active power decoupling single-phase PWM rectifier topology." in Proc. IEEE Appl. Power Electron. Conf., Fort Worth, TX, USA, vol. 3, pp. 8995, 2014
- [8] R. Chen, Y. Liu, and F. Z. Peng, DC capacitor-less inverter for singlephase power conversion with minimum voltage and current stress, IEEE Trans. Power Electron., vol. 30, no. 10, pp. 5499-5507, Oct. 2015.
- [9] S. Liang, X. Lu, R. Chen, Y. Liu, S. Zhang, and F. Z. Peng, A solid state variable capacitor with minimum DC capacitance, in Proc. IEEE Appl. Power Electron. Conf., Fort Worth, TX, USA, pp. 3496-3501, 2014.
- [10] F. Shinjo, K. Wada, T. Shimizu, "A Single-Phase Grid-Connected Inverter with a Power Decoupling Function," IEEE PESC, pp. 1245-1249, 2007.

-
- [11] Y. Ohnuma and J. Itoh, "A Single-phase-to-three-phase Power Converter with an Active Buffer and a Charge Circuit," *IEEE J. Ind. Appl.*, vol. 1, no. 1, pp. 46-54, 2012.
- [12] Yi Tang and Frede Blaabjerg, "A Component-Minimized Single-Phase Active Power Decoupling Circuit With Reduced Current Stress to Semiconductor Switches" *IEEE Transactions on Power Electronics*, VOL. 30, NO. 6, JUNE 2015
- [13] Yao Sun, Yonglu Liu, Mei Su, Wenjing Xiong, and Jian Yang, "Review of Active Power Decoupling Topologies in Single-Phase Systems", *IEEE Transactions on Power Electronics*, VOL. 31, NO. 7, July 2016
- [14] H. Zhao, H. Lin, C. Min, and K. Zhang, A modified single-phase H-bridge PWM rectifier with power decoupling, in *Proc. IEEE Annu. Conf. Ind. Electron. Soc.*, Montreal, QC, Canada, pp. 8085, 2012.
- [15] Peng Fang, Yan Fei Liu, "An Electrolytic Capacitor-Free Single Stage Buck-Boost LED Driver and its Integrated Solution", *IEEE Applied Power Electronics Conference and Exposition*, pp. 1394-1401, 16-20 March 2014
- [16] Udumula Ramanjaneya Reddy, Beeramangalla Lakshminarasaiiah Narasim-haraju, "Single-stage electrolytic capacitor less non-inverting buck-boost PFC based ACDC ripple free LED driver", *IET Power Electronics*, VOL. 10, pp. 38-46, 16 January 2017
- [17] Yoshiya Ohnuma and Jun-Ichi Itoh, "A Novel Single-Phase Buck PFC ACDC Converter With Power Decoupling Capability Using an Active Buffer", *IEEE Transactions on Industry Applications*, VOL. 50, NO. 3, pp. 1905-1914, May/June 2014
- [18] J. Marcos Alonso, Juan Viña, David Gacio Vaquero, Gilberto Martínez, and René Osorio "Analysis and Design of the Integrated Double BuckBoost Converter as a High-Power-Factor Driver for Power-LED Lamps", *IEEE Transactions on Power Electronics*, VOL. 59, NO. 4, April 2012
- [19] Sinan Li, Wenlong Qi, Siew-Chong Tan and S. Y. R. Hui, "A Single-Stage Two-Switch PFC Rectifier with Wide Output Voltage Range and Automatic AC Ripple Power Decoupling", *IEEE Transactions on Power Electronics*, VOL.32, pp. 6971-6982, 28 October 2016
- [20] Wenli Yao, Poh Chiang Loh, Yi Tang, Xiongfei Wang, Xiaobin Zhang and Frede Blaabjerg, "Robust Power Decoupling Control Scheme for DC Side Split Decoupling Capacitor Circuit with Mismatched Capacitance in Single Phase System", *Power Electronics for Distributed Generation Systems (PEDG)*, pp. 1-8, 2016
- [21] Mohammad N. Marwali, Min Dai and Ali Keyhani, "Robust Stability Analysis of Voltage and Current Control for Distributed Generation Systems", *IEEE Transactions on Energy Conversion*, VOL. 21, pp.203-223, June 2006

-
- [22] Akira Tokumasu, Kazuhiro Shirakawa, Hiroshi Taki, Keiji Wada, "AC/DC Converter Based on Instantaneous Power Balance Control for Reducing DC-Link Capacitance", *IEEE Journal of Industry Applications* VOL. 4, No. 6, pp. 745-751, 2015
- [23] A Sliding-Mode Duty-Ratio Controller for DC/DC Buck Converters With Constant Power Loads, *IEEE Transactions on Industry Applications*, VOL 50, pp. 1448-1458, March 2014
- [24] S.-c. Tan, Y.m. Lai , C.k. Tse, L. Martinez-Salamero, "Special family of PWM-based sliding-mode voltage controllers for basic DC-DC converters in discontinuous conduction mode", *IET Electric Power Applications*, VOL. 1, pp. 64-74, February 2007
- [25] Seddik Bacha, Iulian Munteanu, Antoneta Iuliana Bratcu, "Advanced Textbooks in Control and Signal Processing Power Electronic Converters Modeling and Control with Case Studies" 10.1007/978-1-4471-5478-5, Springer page 385-422
- [26] Igor M. Boiko, "Analysis of Chattering in Sliding Mode Control Systems with Continuous Boundary Layer Approximation of Discontinuous Control", *American Control Conference (ACC)*, pp. 757-762, June 29 - July 01, 2011
- [27] Yi Tang, Frede Blaabjerg, Poh Chiang Loh, Chi Jin, Peng Wang, "Decoupling of Fluctuating Power in Single-Phase Systems Through a Symmetrical Half-Bridge Circuit" *IEEE Transactions on Power Electronics*, VOL. 30, NO. 4, April 2015
- [28] W.Qi, H.Wang, X.Tan, G.Wang, and K.D.T.Ngo, "A novel active power decoupling single-phase PWM rectifier topology." in *Proc. IEEE Appl. Power Electron. Conf.*, Fort Worth, TX, USA, vol.3, pp.8995, 2014
- [29] W. Cai, L. Jiang, B. Liu, and C. Zou, "A power decoupling method based on four-switch three-port DC/DC/AC converter in dc microgrid," *IEEE Trans. Ind. Appl.*, vol. 51, no. 1, pp. 336343, Jan./Feb. 2015.
- [30] H. Li, K. Zhang, H. Zhao, S. Fan, and J. Xiong, "Active power decoupling for high-power single-phase PWM rectifiers." *IEEE Trans. Power Electron.*, vol. 28, no. 3, pp. 13081319, Mar. 2013.
- [31] I. Serban, "Power decoupling method for single-phase h-bridge inverters with no additional power electronics." *IEEE Trans. Ind. Electron.*, vol. 62, no. 8, pp. 48054813, Aug. 2015.
- [32] Y. Tang and F. Blaabjerg, "A component-minimized single-phase active power decoupling circuit with reduced current stress to semiconductor switches," *IEEE Trans. Power Electron.*, vol. 30, no. 6, pp. 29052910, Jun. 2015.
- [33] Y. Tang, Z. Qin, F. Blaabjerg, and P. C. Loh, "A dual voltage control strategy for single-phase PWM converters with power decoupling function." *IEEE Trans. Power Electron.*, vol. 30, no. 12, pp. 70607071, Dec. 2015.

-
- [34] Hasan Komurcugil, Necmi Altin, Saban Ozdemir, and Ibrahim Sefa, "An Extended Lyapunov-Function-Based Control Strategy for Single-Phase UPS Inverters" *IEEE Trans. Power Electron.*, vol. 30, no. 7, July 2015
- [35] S. R. Sanders and G. C. Verghese, "Lyapunov-based control for switched power converters" *IEEE Trans. Power Electron.*, vol. 7, no. 1, pp. 1724, Jan. 1992.
- [36] M. Mahdavi and H. Farzanehfard, "Bridgeless SEPIC PFC rectifier with reduced components and conduction losses" *IEEE Trans. Ind. Electron.*, vol. 58, no. 9, pp. 4153-4160, Sep. 2011
- [37] Yonglu Liu, Yao Sun, and Mei Su "A Control Method for Bridgeless Cuk/Sepic PFC Rectifier to Achieve Power Decoupling", *IEEE Trans. Ind. Electron.*, Vol. 64, No. 9, Sep 2017
- [38] Modeling and Simulation of Interleaved Buck- η Boost Converter with PID Controller *IEEE Sponsored 9th International Conference on Intelligent Systems and Control*, 9-10 January. 2015